Part IV

Field Coupling

CREDITS: The chapters in this part are derived partly by the MSc thesis of Ing. Yuri Ardesi, Ing. Giuliana Beretta, and from the notes of current students of the course . These chapters are elaborated on the basis of the lectures of prof. Mariagrazia Graziano and related literature.

IMPORTANT DISCLAIMER NOTE: as mentioned in the main introduction, the reference for the exam preparation are the SLIDES given during the lectures and the registration. The material given her is to be considered an integration, and not necessarily it is complete w.r.t. the SLIDES part.

CHAPTER 9

General Field Coupling concept

9.1 FCN and QCA as solutions for *Beyond CMOS*

Since the scaling of the current CMOS technology will reach the fundamental limit in the near future the era of "Beyond CMOS" will start. In particular, among all of these evolving nanotechnologies, Field-Coupled Nanocomputing (FCN) paradigms show great potential and they are viable candidate for "Beyond CMOS" device technology. In FCN paradigms information encoding, transmission and computation are achieved, not using transistors, but via local field interactions between nanoscale building blocks arranged in array form. Several FCN paradigms are currently under active investigation, including Quantumdot Cellular Automata (QCA), Molecular Quantum-dot Cellular Automata (MQCA), NanoMagnetic Logic (NML), and Atomic Quantum Cellular Automata (AQCA). Each of these paradigms presents features that make it a good candidate for BeyondCMOS technologies, but each of them must face great obstacles to realization and fabrication [3]. The QCA is a FCN based architecture that has been proposed by C.S. Lent and his co-worker at early 1990s derived from the confluence of four concepts (see Prof. Lent's group site for most of the original publications from which some of the basic material is reported iin this inizial part per the chapter https://www3.nd.edu/ lent/Publications.html):

1. The ability to realize configurations of quantum dots able to localize charge.
2. The practical device would need bistable saturation in the information transfer function, argued by Landauer.
3. The charge quantization leads to non-linearity of charge tunneling between such dots.
4. The notion of a locally coupled architecture in analogy to Cellular Automata (CA).

Which means that the binary information is encoded using an elementary unit called QCA Cell, in which the state of each cell is determined by the state of the neighbouring cells. The information propagation occurs through field coupling, either electrostatic or magnetic, of such QCA cells, not requiring charge transport among them. The power dissipation is significantly reduced with respect to standard CMOS technology where current flow is present, and high device density and working frequency up to THz are achievable.

9.1.1 Single QCA Cell or FCN cell

The basic QCA cell is a squared nanostructure of potential wells confining free electrons. Each cell is constructed from six quantum dots (or four quantum dots depending on the implementation technology), which can ideally hold a mobile charge per dot, and binary information is represented by the arrangement of these charges (or magnetic dipoles) inside this cell. Importantly, cells are designed to have a bistable charge configuration, which means to have two low energy states with different dipole or quadrupole orientation that can encode a binary logic states

"1" or "0", and no current flows into or out of the cell. Using indexing convention illustrated in Figure 9.1, cell polarization is defined as:

$$P = \frac{(\rho 1 + \rho 3) - (\rho 2 + \rho 4)}{\rho 1 + \rho 2 + \rho 3 + \rho 4}$$

where ρi is the charge density at dot i and its value represents the average number of electrons occupying dot i.

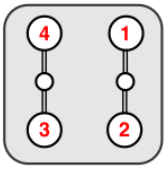

Figure 9.1: Standard Logic dots indexing in QCA cell.

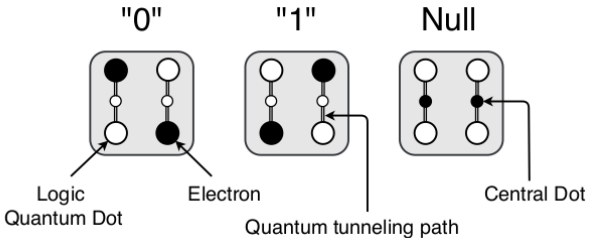

Figure 9.2: QCA cell structure and logic state encoding.

When the two free electrons lie in the main diagonal of the cell the logic state "0" is reached and the cell is negatively polarized $P = -1$, vice versa if they lie in the anti-diagonal the logic state "1" is reached and the cell is positively polarized $P = +1$. The third state represents the condition when the two free electrons are forced to occupy the two central dots, representing the so-called NULL state $P = 0$ because in this configuration the cell is unpolarized and no binary information holds in it. Apparently it may seem useless, nevertheless it is fundamental to fix switching issue and favour the transition between the logic states, moreover, in the future can be used to create a ternary logic system. The working principle of QCA relies on quantum mechanical inter-dot tunneling of the electrons localized in the Logic Quantum Dots (physically they are wells), and on coulombic interaction between these mobile charges. The barrier potential between dots should be high enough so that charge can only tunnel through the barrier, allowing the localization and confinement in the dots and not in the tunneling paths. The electrons arrangement in the QCA cell is ruled by the Coulomb's law according to which the electrons tend to occupy the Logic Quantum Dots with maximum distance, minimizing electrostatic repulsion between them and reaching the minimum energy condition. Therefore, there are the only two possible configurations of the electrons because all other arrangements lead to maximum repulsion as shown in Figure 9.3.

9.1.2 Cell coupling

In order to understand how the information is transferred it is necessary to examine the coupling between two adjacent cells. When two QCA cells are placed close enough to each other, always by means coulombic interaction, the first cell (Driver cell) induce the second cell (Target cell) to assume the same polarity reaching the minimum energy condition. The electrostatic cell-cell coupling can be described by the so-called *kink energy*, Ekink , associated with the energetic cost of two neighbouring cells having opposite polarization. The electrostatic interaction between charges in two four-dot cells, A and B, is:

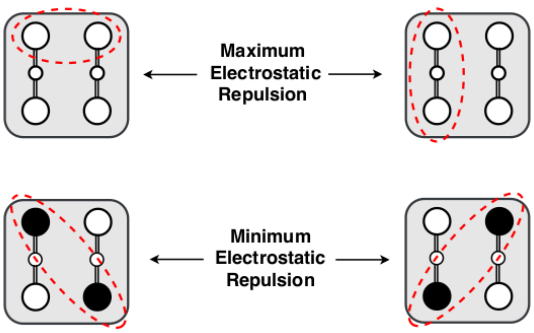

Figure 9.3: Maximum and minimum electrostatic repulsion conditions in QCA cell.

$$E_{A,B} = \frac{1}{4\pi\epsilon}\sum_{i=1}^{4}\sum_{j=1}^{4}\frac{q_i^A q_j^B}{|r_i^A - r_J^B|} \tag{9.1}$$

where q_i^A and q_i^B is the charge in dot i of cell A and B, respectively. While r_i^A and r_i^B is the position of dot i in cell A and B, respectively. The *kink energy* is defined as the difference in energy between two cells that have opposite polarization and those same two cells having the same polarization:

$$E_{A,B}^{kink} = E_{A,B}^{oppositepol} - E_{A,B}^{samepol} \tag{9.2}$$

Actually, there are two positive background charges distributed underneath the cell to represent the counter-ion and ensure charge neutrality of the system. These charges must also be included in the expression of the kink energy, and it can be shown that the kink energy has a decaying behaviour proportional to the fifth power of the distance between cells. This property can be useful to evaluate the possible crosstalk between QCA circuits. Therefore, the state of a particular cell is transferable to another cell as shown in Figure 9.4, and aligning several cells like an array it is able to propagate information since all successive cells must change their polarization to achieve the new minimum energy condition, like Domino effect. Whenever the i-th driver cell switches his polarity a polarization refresh of the target cell occurs, reducing the need to have repeaters in the QCA circuits.

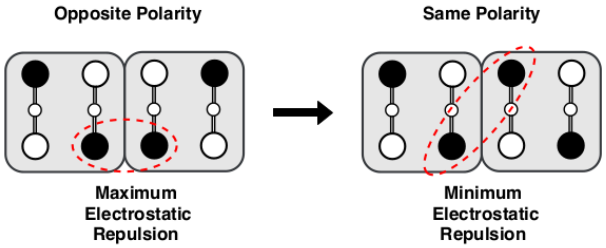

Figure 9.4: State transfer between two adjacent cells.

9.1.3 Basic FCn Building Blocks

The most elementary building block in QCA technology is the QCA Wire that consists in an array of QCA cells aligned in order to form a row (Figure 9.5). Unlike CMOS technology, where the interconnections have their own set of principles and designs, in this technology the wire represents a processing element since the propagation of binary information depends on the correct polarity of each single QCA cell. An example how the information travels in the binary QCA Wire is shown in Figure 9.6, in which is highlighted the chain reaction that starts when the logic state of the first cell (the input) is changed.

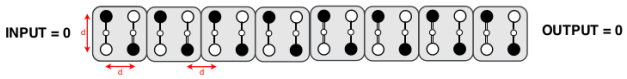

Figure 9.5: FCN binary wire.

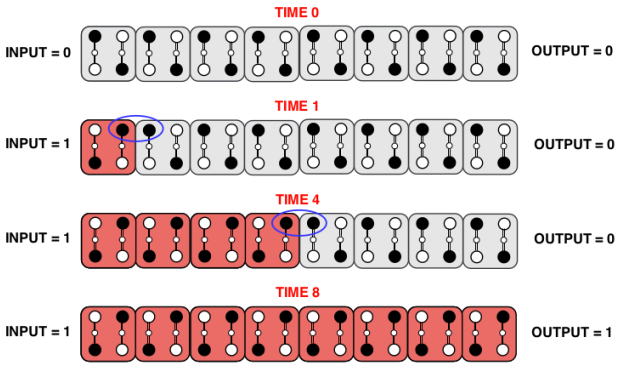

Figure 9.6: Propagation of information in a FCN Wire.

Other important basic elements such as the FCN Inverter (Figure 9.7) and QCA Majority Voter (Figure 9.9) can be implemented. The FCN Inverter exploits the electrostatic corner interaction (or diagonal coupling) to reverse the propagating state as illustrated in Figure 9.8.

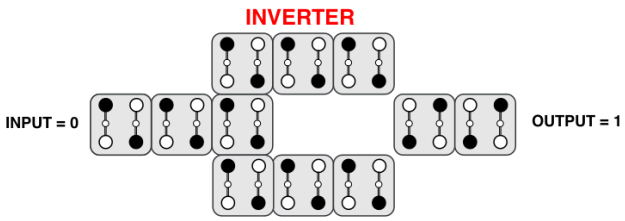

Figure 9.7: FCN Inverter.

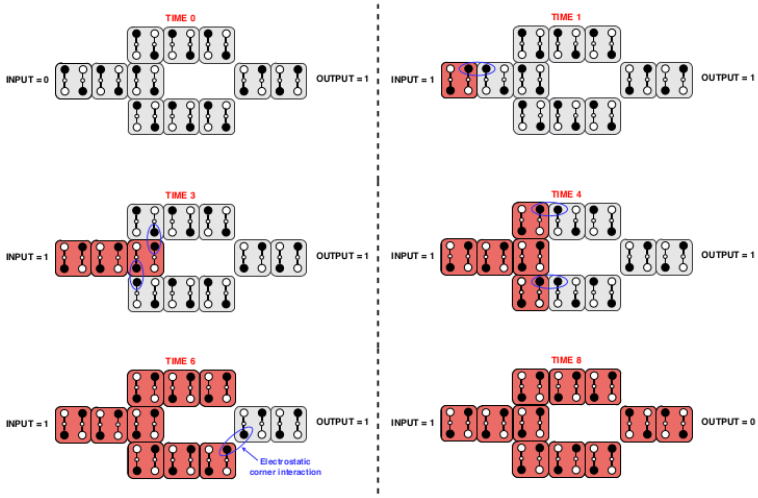

Figure 9.8: FCN Inverter: information propagation.

The Majority Voter (Figure 9.9) is a logic circuit which has three inputs and one output, the output is determined by the simple majority rule, according to which the output state is the polarization that has the majority at the three inputs. This basic device performs the following

C	B	A	OUT
0	0	0	0
0	0	1	0
0	1	0	0
0	1	1	1
1	0	0	0
1	0	1	1
1	1	0	1
1	1	1	1

Table 9.1: Truth table of the majority gate function.

boolean function OU T = AB + AC + BC and it has great importance. Table 9.1 shows the gate thruth table
Forcing one of the inputs to the logic state "0", the block acts as the AND gate since the output is equal to the logic "1" only if the other two inputs are "1" (Figure 9.10). On the other hand, with one input forced to "1", the OR gate is implemented, since the output is equal to the logic "0" only if the other two inputs are "0" (Figure 9.11). Therefore, having the possibility to implement the three fundamental blocks of the combinational logic (Inverter, AND, OR), any Boolean functions could be constructed using majority voters and inverters.

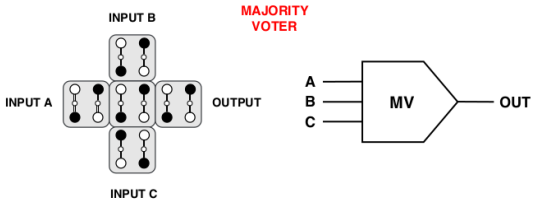

Figure 9.9: FCN Majority Voter (MV).

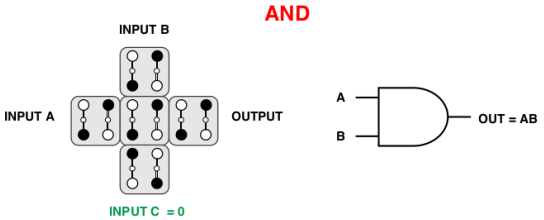

Figure 9.10: FCN AND based on Majority Voter.

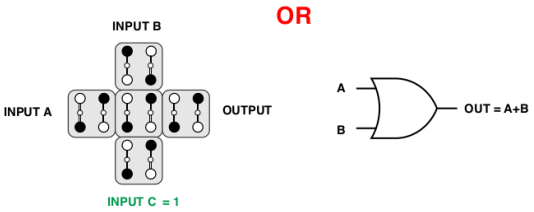

Figure 9.11: FCN OR based on Majority Voter.

9.1.4 The Clocking FCN System

Ideally, using an edge-driven approach, which means changing the boundary condition (the input) of the circuit, the information flow occurs without any problem thanks to Domino effect mentioned in the previous section. However, this approach limits the size of the circuit, since larger circuits tend to stabilize in one of many unwanted metastable states corrupting the information flow. Indeed, as explained in to guarantee correct computation can be used only a maximum number of cells.
Indeed, what has been assumed until now was:

- cell configuration can switch, so there is a *low potential barrier* between the two possible states;
- logic values are stable, so there is a *high potential barrier* between the two configurations;
- there is a direction of propagation, i.e. information goes from the left to the right;
- there is no loss of information during the propagation.

For what concerns the last point, it is true for a limited number of cells: overcame that maximum number of neighbouring cells, information gets lost. The main causes of this phenomenon are temperature and external noise. On the other hand, to solve the first two questions that are in contrast, the cell must be enriched with a sort of *Enable*. This should, from one side, reduce the barrier for the switch and the propagation, and on the other side increase the barrier to have stable logic states.
To do this, cells should have six dots, as shown in Figure 9.12(a).
FIGURA

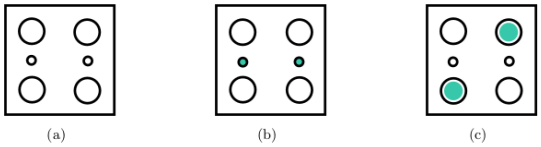

Figure 9.12: Schematic of enriched QCA cells: (a) QCA basic cell with the six quantum dots represented, (b) QCA basic cell in the *Null state* or *Reset State*, (c) QCA basic cell in one of the two *stable states*.

The new dots are regions where electrons can go only depending on the *enable signal*. In this case, charges are trapped in the central dots in an unstable state, called *Null state* or *Reset State*, so there is the need to apply an external electric field, as displayed in Figure 9.12(b). When the external field is released, charges are in a *stable state*, and the cell assumes the same configuration of the input. The external field is usually called *Clock*, and ideally is a square wave, as schematically shown in Figure 9.13.
In real situations, the assumption to work with a perfect square wave clock signal is not possible. The clock signal is an electric field that cannot switch instantaneously, thus actual signals are trapezoidal waves, as shown in Figure 9.14(a).
The last question to solve is related to the assurance of a correct propagation, for example in long wires. The circuit is thus organized in *zones* or bunches of cells [**?**]. The number of cells in each zone depends on the technology: each zone embraces a maximum number of cells, in order to assure no loss of information in a given condition. Each zone is associated with a different clock signal: clock signals are applied in sequence, so information propagates as in a pipeline, as shown in Figure 9.14(b). Moreover, using trapezoidal clock signals, the system works properly even in the presence of jitter. So, the overlaps of the clock signals are useful to avoid errors in the switching of the cells.
The mechanism introduced is named *Adiabatic switching*. According to this mechanism then each circuit, even complicated, is partitioned in smaller sections called Clock Zones is performed, in which in each of them a vertical multi-phase clock field is applied to help the cell state transition,

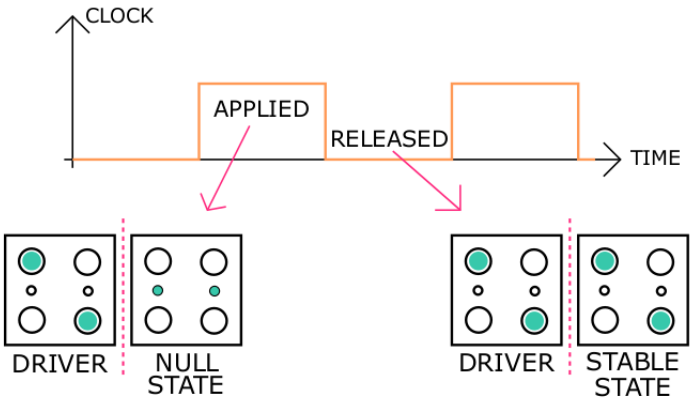

Figure 9.13: Schematic representation of the two possible situations related to the clock signal: when the *Clock* is active, or *Applied*, the cell stay in the *Null state*, whereas the *Clock* is not active, or *Released*, the cell configuration is stable and follow that of the input cell, usually called *Driver*.

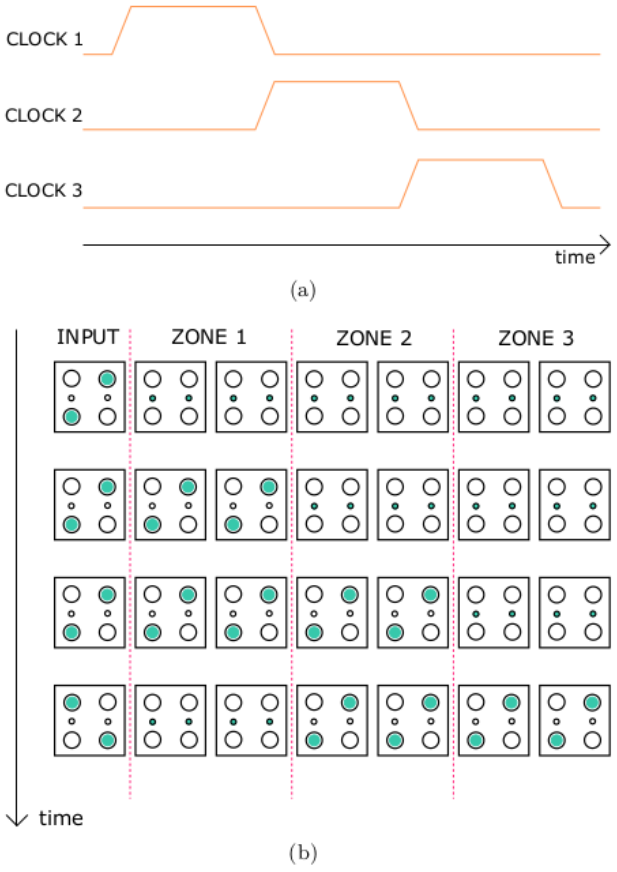

Figure 9.14: Schematic representation of the information propagation as a pipeline: (a) trapezoidal clock signals overlapped to ensure correct propagation, (b) example of the first time steps in a wire.

e.g., switching the cells between a NULL state and Logic states without metastability. As a matter of fact, the Clock, usually applied and controlled using coupled electrodes, is carried out in four "moments" (Switch, Hold, Release and Relax) as shown in Figure 9.15, and it is able to vary the potential barriers between the quantum dots of the cell, which in turn controls the transfer of charges:

1. Switch Phase: The clock field starts to rise slowly increasing the inter-dot potential bar-

riers and, at the same time, forcing the mobile charges to tunnel from the quantum dots representing the NULL state towards the Logic Dots (Figure 1.15.A), according to the polarization of neighbouring cells. During this phase, the information is encoded and propagated.

2. Hold Phase: The potential barriers reach the maximum value, full polarizing the QCA cells. In this phase the cells are locked in their previous logic states, any kind of tunneling is suppressed and, ideally, no logical switching is possible. The locked cell act as a driver to the next stage.
3. Release Phase: The clock field starts to decrease slowly and the mobile charges are free to tunnel from Logic Dots to central dots (Figure 1.15.B). At the end of this phase, the QCA cells lose their polarization assuming the NULL state configuration.
4. Relax Phase: The potential barriers reach the minimum value locking the QCA cells in the NULL state. Due to the loss of polarization, the cells inside this clock zone do not influence the cells of the other clock zones. Clock Voltage

   Four phase Clock signal waveform.

   Considering a wire, which is clocked from left to right with increasing Clocking Zones, the application of a trapezoidal clock signal with delay of 90 degrees in phase between adjacent zones, as depicted in Figure 1.16, enables adiabatic propagation as well as correct computation. This clock mechanism is called Four-Phase Clock, recalling the number of phases induced by the trapezoidal signal in each clock zone. As a result, the QCA wire is pipelined at the clocking zone level and behaves like a shift register. Finally, it is important to remark that the main advantage of this computing paradigm is that the interaction between cells is electrostatic, which means through a field, not involving conduction of charges in the information flow. As a consequence, this property translates into a strong limitation of power consumption, especially with respect to CMOS technology.

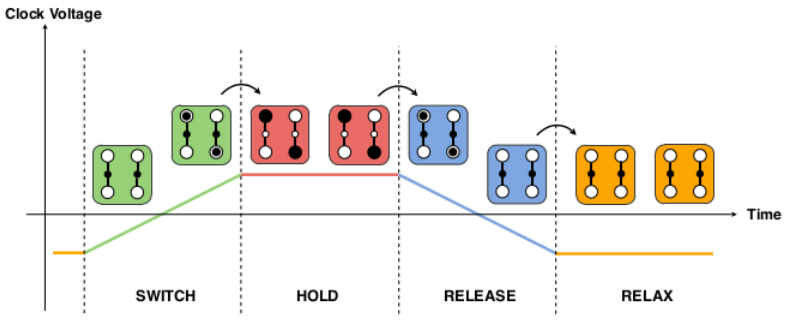

Figure 9.15: Different phases of trapezoidal signal applied to the clock zones of FCN Wire.

9.2 Possible Physical Implementations of FCN devices

As mentioned in the previous chapter the binary information is encoded with charge configuration of the cell and in particular by the confinement and localization of the two charges in the Quantum Dots. The Quantum Dot is a region of space with potential barriers surrounding it sufficiently tight and high to induce charge quantization to a multiple of the elementary charge within itself. Of course, at a certain point, it is necessary to lower the barrier so that a charge can quantum mechanically tunnel from one dot to another [33]. During the years several approaches have been published to create QCA cell and in the following, some of these are discussed according to the schematic classification which follows:

– Metal-Dot QCA (FCN)

– Magnetic FCN or Nanomagnet Logic
– Semiconductor-Dot QCA
– Molecular FCN

9.2.1 Metal-Dot FCN

In metal-dot FCN or Metal QCA implementation the dot is created by small metal islands (Al) on an insulating substrate (SiO2) and tunnel junction are used to create connection between two dots, as shown in Figure **??**. The Metal-Dot QCA is the first fabrication done to implement the QCA cell. Unfortunately, up to now, the current techniques do not allow to scale the metal islands to nanoscale, needing cryogenic temperature (70 mK) to work properly and the maximum operating frequency is in the range of MHz. The reason why this approach is under study, despite the strong limitations described above, is that the electron population inside them is quantized allowing analogous behaviour of quantum dot.

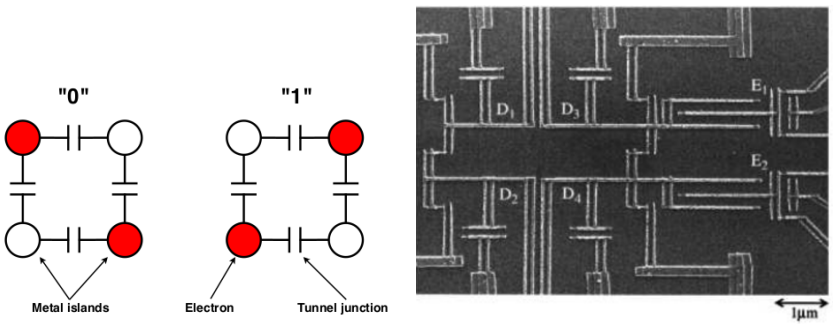

Figure 9.16: Metal Dot FCN and its die photograph (SEM)

9.2.2 Semiconductor-Dot QCA

Another solution consists of exploiting Semiconductor QCA structures, fabricated with advanced CMOS fabrication processes, to create the dots in order to contain mobile charge. The advantage of using semiconductor QCA is that it is based on materials that are very well understood and several fabrication techniques have been created to work with them. Different approaches are used in order to demonstrate semiconductor based QCA operation: SOI Technology and GaAs Technology.

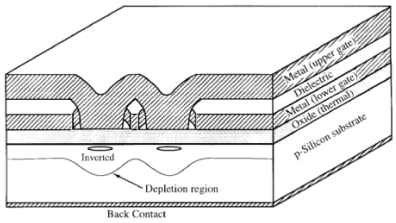

Figure 9.17: Semiconductor DOTs ofr QCA based on a heterostructure

The dots structures can be formed using 3-Dimensional Quantum wells [42], created through patterning of the semiconductor surface [33], permitting energy quantization effect of the charge population inside the dot itself. Unlike the MetalDots, in this case, the dimensions and distance are both of the order of nanometer scale and no longer micrometer one. This structure, like the metal-dot solution has been tested but the results were not particularly successful because it should work at cryogenic temperature, it's highly defective and especially if nano-dimensions should be reached it has been proven that the defects prevent the feasibility of this technology.

9.2.3 Magnetic QCA or Nanomagnet Logic (NML)

In general magnetic phenomena are used for data storage and hard disk implementation because ferromagnetism phenomenon is non-volatile, meaning that magnetization state can be preserved even without power. A lot of research efforts have been performed during the years in order to implement magnetic logic due to the attractive feature that consists in eliminating standby power consumption. Another advantage of the magnetic device is that its intrinsic switching energy can be orders of magnitude lower than a current-based CMOS device due to its nonvolatile constitution [3].

Presented and developed for the first time by Cowburn and Welland [35] and highly explored by Porod group [10], Magnetic QCA cell is composed of nanomagnet or magnetic nano-particle in which the coupling between them is ferromagnetic (the individual nanomagnets tend to be magnetized in the same direction) or antiferromagnetic (the individual nanomagnets tend to be magnetized in the opposite direction), unlike other types of QCA where the coupling is electrostatic one. To encode the binary information the magnetization orientation of QCA cell is utilized, when it is magnetized along "up" or "down" direction the logic state "1" or "0" is achieved, respectively. While the NULL state is encoded forcing the magnetic orientation along the short axis of the cell.

Computing devices are performed by arranging a chain of these elongated nanomagnets with small separation, in which each of them is able to contain single magnetic dipole; in particular the version fabricated by the Cowburn et al. group is a single circular nanodot made up of magnetic Supermalloy N i, created through high-resolution Electron Beam Lithography (EBL). This nanodot presents a diameter of 110 nm, thickness of 10 nm and size of 100 nm, with interspacing between other nanodots equal to 20 nm. Additionally, Ferromagnetically and Anti-ferromagnetically coupling are possible to generate FCN wires.

The main advantages of Magnetic QCA are that they can be operated in room temperature, require fewer fabrication requirements compared to QCA, very low power consumption, high thermal robustness and 3D architectures are possible. Nevertheless, when the nanomagnets are made under 20 nm stability issues are present and the working frequency is lower with respect to existing technologies [42]. Indeed, it is experimentally demonstrated the operation of majority-logic gates at ambient temperature where the predicted frequency reach a speed of about 100 M Hz .

This implementation is largely analyzed in another part of this document.

9.2.4 Molecular implementation

One of the most attractive QCA approaches, apart from the magnetic one, consists of using molecules as structured charge containers, because molecules represent the smallest artificial structures that can be engineered by humans. In MQCA implementation the Quantum Dots are formed by redox-active sites, that are regions inside the molecule itself able to release or to accept an electron without breaking the chemical bonds that hold the molecule together. In the former case, the site is oxidized namely positively charged, while in the latter it is reduced namely negatively charged.

This implementation is analyzed in the following two chapters.

CHAPTER 10

Molecular Field Coupling

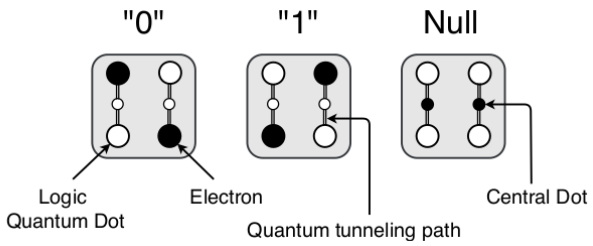

Figure 10.1: QCA cell structure and logic state encoding.

CHAPTER 11

Molecular Field Coupling fabrication

11.1 The guiding wire

Regarding the analysis of the implementation of molecular FCN, fewer studies are found in the literature. The idea is to have a substrate on which molecules attach by mean of a tile, a "guiding wire" as shown in Figure 11.1.

Figure 11.1: Molecular wire implementation: (a) a substrate, for example a gold nanowire, onto which molecules are placed, (b) top view.

The main problem is that molecules have generally dimensions of 1-2 nm, so wires need to have the same dimensions and lithography based technology does not permit it. Moreover, independently on dimensions, it is difficult to have the precision needed to build angles, which would be necessary for a cross structure like that of the majority gate. Since the idea is to deposit molecules employing self-assembled monolayers (SAM), to have regular SAM, a precise wire is needed.

11.1.1 The trench implementation

Another important thing that has to be managed is the generation of the electric fields needed to the computation, which is the clock field and the switching field of the input molecules. To do this, other wires are needed. Among all the possible solutions, the most reliable is the one represented in Figures 11.2 and 11.3. The molecules are placed in a trench, over a wire as seen before. On top of the two edges of the trench, there are other two electrodes. Applying a voltage between these two electrodes, an electric field is generated between them as in a capacitor, and thanks to the border effects even molecules are subjected to this field, as represented in Figure 11.3(a). It is impossible to influence only one molecule, depending on the dimension of the electrodes a certain number of molecules are subjected to the generated field.

The same structure can be used also for the clock field, as shown in Figure 11.3(b). Applying a voltage between the electrodes on the top and at the bottom of the trench, a vertical electric field is generated over the molecule. The expected vertical field depends on the aspect ratio of the trench.

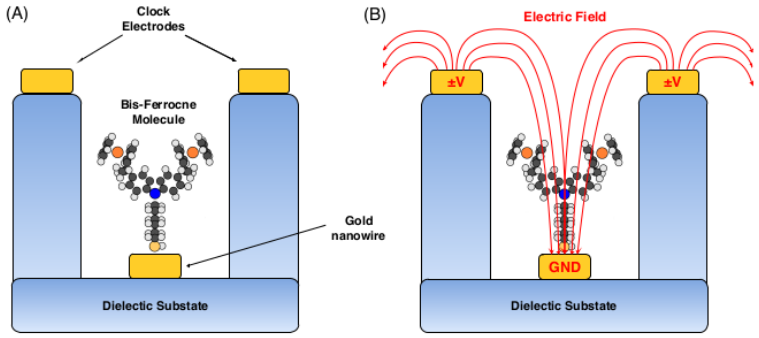

Figure 11.2: (A) Scheme of physical implementation of MQCA clock system (B) Almost vertical Clock field generated by the designed clock system.

Figure 11.3: Implementation of the electric fields involved in the computation (section view): (a) input voltage is generated by two electrodes placed on top of the trench, (b) the clock field is obtained by a potential difference between the top electrodes and the gold nanowire at the bottom of the trench..

The top view of the implementation of a clocked wire is shown in Figure 11.4 and 11.5. In real systems, neighbouring electrodes interfere with each other, the two fields overlap: the goal is to have constructive interference to not lose the information. Overlapping in time the clock signal waves solve also the issue concerning the overlap in space.

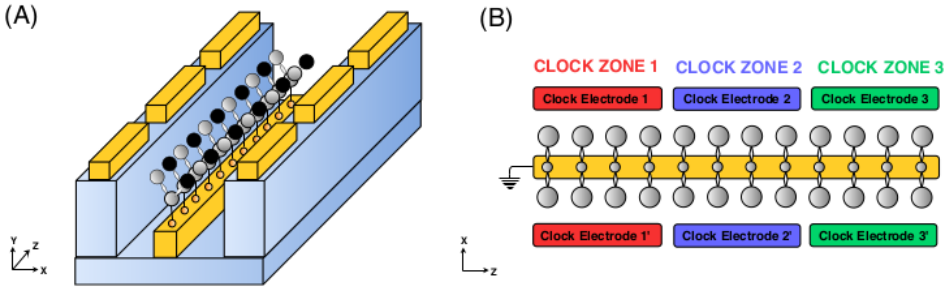

Figure 11.4: Scheme representation of MQCA physical implementation: (A) 3D view (B) Top view with Clock Zone partition.

Another problem emerges looking at the space between the electrodes, as shown in Figure11.6. A separation of about 1 nm is desired, which is the order of magnitude of the distance between two molecules, but this is impossible to obtain with current technology. With a realistic separation, it is possible to see that some molecules are not associated to any electrode. Anyway, the presence of overlapped fields in space solves this resolution problem.

According to this implementation to generate adiabatic propagation of information the MQCA device, for example, a MQCA Wire is divided into three clock zones. The reason why three electrodes are used, instead of four, is that a movement towards a zone-less configuration is accomplished. Reflecting the clock zones three gold clock electrodes for each

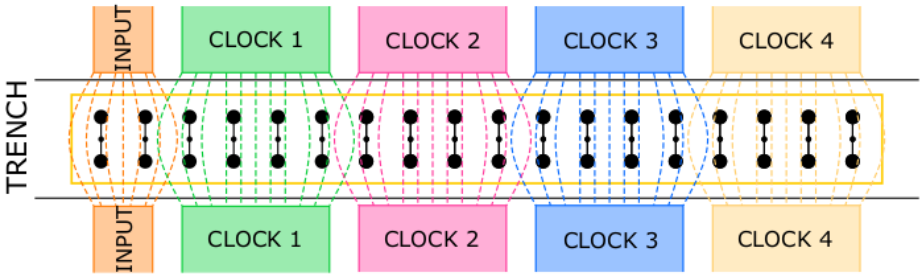

Figure 11.5: Clocked molecular FCN nanowire implementation.

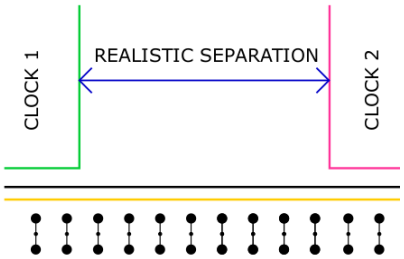

Figure 11.6: Clocked molecular FCN nanowire implementation: zoom in the separation of two electrodes.

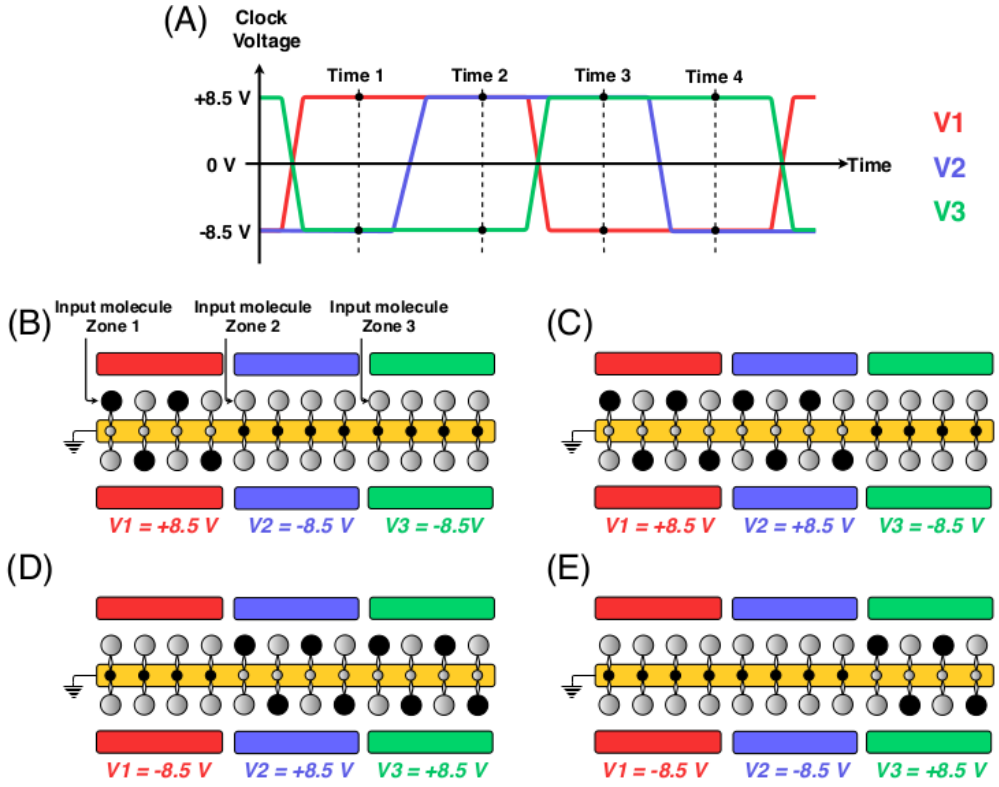

Figure 11.7: Schematic example of information propagation in MQCA Wire

side are patterned and in each of these electrodes the same time varying trapezoidal clock signal, but with different phase, is applied. According to the Finite Element Method (FEM) simulations with COMSOL Multiphysics program, the maximum and minimum values that the clock signal reaches are +8.5 V and -8.5 V, respectively, because they ensure to have

a clock field equal to ± 2 V /nm necessary to optimally enhance/inhibit the molecular interaction between oxidized Bis-ferrocene molecules. Higher voltage values generate clock signals greater than ±2 V /nm, giving the possibility to increase the amount of charge in the active dots, however, this leads a higher power consumption and at an extra amount of charge that is unnecessary for logic switching. To explain how propagation occurs, four time instants involved on MQCA Wire propagation are described and sketched in Figure 11.7(A).

- Time 1: The set of three values (+8.5 V , -8.5 V , -8.5 V) is applied to the Clock Zone 1, Clock Zone 2 and Clock Zone 3, respectively. In the meantime, at the input molecule is assigned externally the desired logic state by means write-in system. Since the clock signal applied in Zone 1 allows the molecules to electrostatically change their polarization according to the logic state of the input molecule, the binary information propagates, while the molecules in Zone 2 and Zone 3 are forcibly induced in the NULL state prohibiting any form of molecular communication with the molecules in Zone 1 (Figure 11.7(B)).
- Time 2: When all molecules in Zone 1 complete their logic states switching, the set of three values (+8.5 V , +8.5 V , -8.5 V) is applied to the three Clock Zones. In this way the polarization of the molecules in Zone 1 maintain their previous configuration, while those belonging to Zone 2 are able to assume the proper polarity according to the new Zone 2 input (which in turn depends on the molecules' polarization of Zone 1), continuing the transmission of information. Concerning the Zone 3 the molecules are frozen in the NULL state (Figure 11.7.(C)).
- Time 3: Keeping going with the same mechanism, the applied set of three voltage values is (-8.5 V , +8.5 V , +8.5 V). The molecules in Zone 2 maintain their previous polarization and molecular communication among Clock Zone 2 and Clock Zone 3 is possible allowing information flow in Zone 3. Regarding the Zone 1 molecules, they undergo a Reset operation setting them in the
- Time 4: With the set (-8.5 V , -8.5 V , +8.5 V) fully propagation occurs in Zone 3 and Zone 2 is reset together with the Zone 1, in order to be ready for the transmission of a new binary data (Figure 11.7(E)). Whereupon, the process starts again with another imposed logic state to the input molecule in the Clock Zone 1.

In particular, using this implementation, in each clock zone three working conditions are involved. Taking as reference the Time 2 depicted in Figure 11.7.(C), it is possible to identify that in the first Clock Zone all molecule are in Hold State, in the Clock Zone 2, the information propagates until all molecules assume proper polarization (Switch State), while in Clock Zone 3 all molecules are in Reset State. For this reason, this clock mechanism is called Three-Phase Clocking. Therefore, alternating the phases of the clock signal applied to the electrodes along the Molecular QCA Wire, the correct information flow is ensured.

11.1.2 Wave clocking

A possible zone-less clocking configuration is the so-called Sinusoidal Clocking.

This configuration is based on the idea to have a single electrode in which a high- frequency signal is applied. Therefore, instead of dividing the QCA Wire into clock regions, the electrode is made continuous and it is treated as a transmission line where the signal is supposed to propagate as electromagnetic wave, generating an electric field which changes with respect to the position and to the time. Making a comparison among the Sinusoidal Clocking and Three-Phase Clocking, illustrated in Figure 11.8, in the former one electrode is present and only one signal propagates in the space, in the latter three electrodes and as many signals, with annexed interconnects to provide them, are needed.

In particular, in Three-phase clocking the propagation performances are influ- enced by the inter-electrode space in which there is a sudden change of applied electric field into the

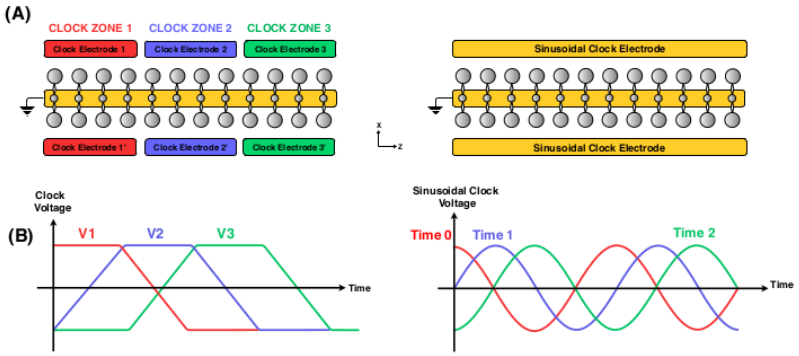

Figure 11.8: (A) Clock systems comparison: Three-Phase Clock schematic (left) Sinusoidal Clock schematic (right), (B) corresponding Clock voltages.

Wire. This criticality is removed with Sinusoidal Clocking configuration, and in addition, it may be very interesting from a technological point of view because a single electrode fabrication could be easier to obtain.

11.1.3 Defects and process variations

From the information propagation point of view, there are many parameters involved. First of all, the parameters relative to the trench, so mainly height and width, which influence the application of the electric fields. Linked to this has to be mentioned also the separation of the electrodes, which depends on the precision of the production process. Even the limit of the width of the guiding wire is imposed by the lithography process. For what concern the guiding wire there other two characteristics that influence information propagation: the lattice structure, which defines the regularity of the SAM anchoring, and the roughness, because the wire is not perfectly flat. In the case of a metal wire, both *inter-grain* and *intra-grain* irregularities have to be mentioned: grains are not all the same heigh and they are not perfectly smooth, as shown in Figure 11.9(a).

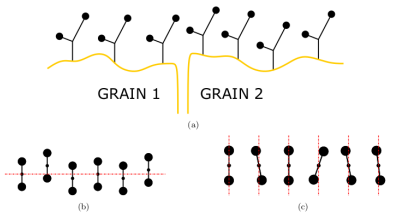

Figure 11.9: Schematic representation of some possible implementation defects: (a) vertical misalignment, (b) horizontal shift, (c) tilting.

Due to this, it is possible to have:

- vertical misalignment among molecules, Figure 11.9(a);
- horizontal shifts due to different anchoring points, Figure 11.9(b);
- tilting, due to defects and different grains orientation, Figure 11.9(c).

Finally, two more possible defects related to the SAM regularity are the presence of extra molecules not included in the design or the lack of some molecules, that can affect the propagation of the information.

Part V

Magnetic Logic (in memory)

CREDITS: The chapters in this part are derived partly by the MSc thesis of Ing. Marco Vacca, Fabrizio Riente, Chiara Cannavó, Elisa Plotzner, Davide Blua, Fabrizio Cairo, Giulia Santoro, Alessandro Morè, Antonino Ferrara, Teulant Marpepa and others (see references), and from the notes of current students of the course . These chapters are elaborated on the basis of the lectures of prof. Mariagrazia Graziano and related literature.

IMPORTANT DISCLAIMER NOTE: as mentioned in the main introduction, the reference for the exam preparation are the SLIDES given during the lectures and the registration. The material given her is to be considered an integration, and not necessarily it is complete w.r.t. the SLIDES part.

CHAPTER 12

Logic in memory concepts and review on magnetism

12.1 Logic in Memory

Currently what we are relying on is the concept of Von-Neumann architecture in which we have a CPU (made by different cores), a memory (typically we have several memories) and a bus; what happens is that we fetch the instructions from the memory, we decode the instructions and then we execute them (actually the execution requires several sub-steps). During the execution we get the data from the memory, we execute the operation in the CPU on the base of the instruction that arrived and on the data and then we typically store the result in the memory. This involves going to and from the memory, so we have to use the bus system and the memory in reading and writing; however both these two elements are slow with respect to the CPU since buses typically are very long whereas the memories are big, this means that they are adding a lot of input capacitances, there is a lot of power consumption and also reading or writing the memory can be a long operation depending on the technology we are using. In this context we talk about "memory bottleneck" or "dark memory" which means that maybe we have the capability to produce big memories but we cannot use them as we would.

A possible solution could be use the memory hierarchy organization with multiple caching systems with all the problems that this brings, especially in multi-processor systems; this is a method that has been adopted from long time. The other technique that is now being studied and also introduced firstly at research level and then at industrial level is the concept of logic in memory (or "memory computing" or "processing in memory"), in this case the idea is that for several operations this going forward and backward from the memory and the CPU is useless and so we could think of processing part of the instructions using a "smart memory", embedding some logic in the memory.

Of course this would change the concept of memory and also its performance, this is the reason why just some parts of the memory could be enriched with these smart parts. Nowadays what's happening at the research toward the industrial level is that we talk more about "logic near memory" in the sense that touching the memory technology is considered a dangerous operation because the memory is very highly optimized even with some analogic parts, then as soon as we touch something everything will break. So, one of the more easy ways to do this is to put some logic around the memory, in this way at least we don't have to move data if not just nearby. this has been adopted and actually in some cases this is done in a 3D fashion, we have integrated structures in which we have the memory on the bottom in several layers and then the logic on the top connected together.

So, as introduced before, in-memory computation has been extensively targeted in literature

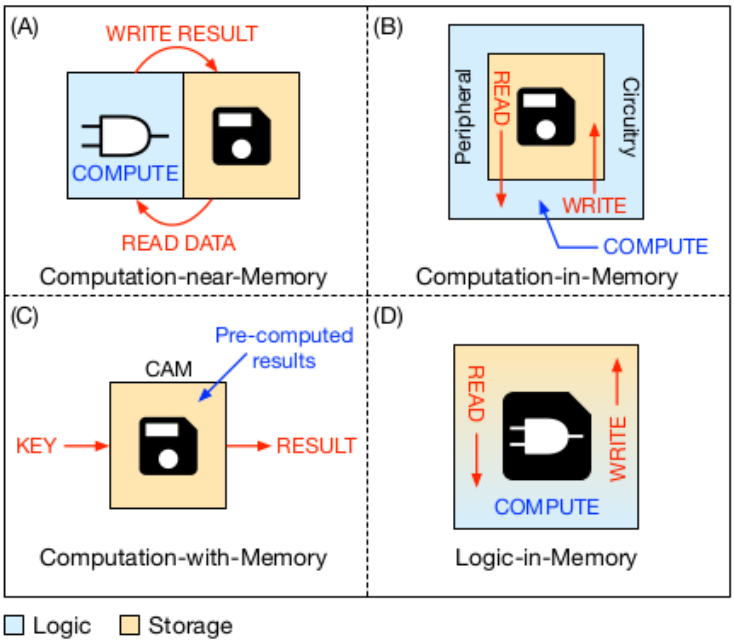

Figure 12.1: Depending on the role that the memory plays in computing data, four main approaches can be defined. (A) Computation-near-Memory: logic and storage are still two separate entities but they are brought closer together thanks to 3D- integration technologies. (B) Computation-in-Memory: memory is used as is to perform computation. The actual data manipulation takes place in the peripheral circuitry (e.g. sense amplifiers) of a memory. (C) Computation-with-Memory: memory is used (as a CAM) for storing pre-computed results for LUT-based computation. (D) Logic-in-Memory: simple logic is added inside the memory cell to manipulate data locally.

and different solutions have been explored. Given the extent of the State of the Art and the differences between the proposed approaches in terms of design and implementation choices, it is very difficult to make comparisons. In the following a taxonomy is presented that categorizes the main works present in literature, based on the role that the memory plays in computing data. Four main approaches have been defined and in figure 12.1 the differences between them are highlighted.

12.1.1 Computing-near-Memory Approach

This approach can be considered as an evolution of conventional architectures where logic and memory are two separated units. In fact, works that belong to this category try to bring closer computation and storage by exploiting 3D Stacked Integrated Circuit (3D-SIC) technology. This 3D integration technology allows to stack silicon wafers or dies one on top of the other by interconnecting them vertically, exploiting through-silicon vias (TSVs). As the name suggests, a TSV is an electrical connection that crosses a silicon wafer, connecting the two sides of it. By exploiting a 3D-stacking technology, not only memories can be implemented as 3D structures with several memory layers stacked one on top of the other (such as the Hybrid Memory Cube, HMC or the High Bandwidth Memory, HBM), but they can also be stacked on top of a computing unit. Computation and memory are very close but still separate entities. For this reason, this approach has been named Computation-near-Memory (CnM). Moreover, as shown in figure 12.1(A), there is data movement from the memory, when data are read and sent to the computing unit, and to the memory, for writing back results. The advantages of TSV technology are manifold: shorter interconnections, wider memory bandwidth, reduced power consumption, more functionality (and/or storage capacity) in a smaller area. All these benefits help

mitigate the memory-bottleneck problem. In particular some authors propose a multi-core architecture where each processor is composed of two tiers, a computing one and a memory one stacked on top of it. In a couple of proposals host processor (a GPU in the former paper and a CPU in the latter, non 3D- stacked in both cases) delegates data-intensive tasks to 3D-stacked computation- near-memory units that act as co-processors. In other cases in bibliography authors exploit the logic layer at the base of the HMC to perform near-memory computing. IN other works researchers do not make use of a 3D-stacking technology, but they propose to integrate the processor and memory banks on the same silicon die to exploit a direct connection between them and avoid off-chip communication. The benefits of such architectures are demonstrated by means of memory-intensive and parallel benchmarks. Moreover, all the works cited here are implemented in CMOS technology.

12.1.2 Computing-in-Memory Approach

Works belonging to these category use non-volatile memory technologies, such as MRAM (Magnetoresistive Random-Access Memory) or RRAM (Resistive Random-Access Memory) , or volatile memory technologies, like DRAM (Dy- namic Random-Access Memory) or SRAM (Static Random-Access Memory), to perform both computation and storage tasks, by using technology as is. This means that the memory array is not modified in terms of structure and functional- ity, but its analog functionality is exploited to perform operations inside the array. To be more specific, peripheral circuitry (i.e. sense amplifiers, SAs) is modified and used to perform row-wise or column-wise logic operations. Hence, in-memory computation is performed by reading data which is sensed and processed by SAs and the result is written back in the array, as depicted in figure 12.1(B). In this case, data is not moved out of the memory for the computing task, hence the name Computing-in-Memory (CiM). Several works use a RRAM array to perform logical or arithmetic operations depending on the target application; in partcular some researchers propose to modify a commodity DRAM to perform bulk bitwise logic operations inside the memory. In other proposals RRAM arrays are connected by means of configurable interconnects to realize fast in-memory adder trees. The configurable interconnects can also be used to shift data. Other authors propose a hybrid architecture in which CMOS logic is used to perform instruction fetch and decode or other functions needed to manage the data computation done inside the RRAM array. In another works a chip for energy- harvesting applications is presented. The system is composed of a host CPU and RRAM arrays used as co-processor to accelerate ANN-like computing.

12.1.3 Computing-with-Memory Approach

As the previous one, this approach is also based on performing computation and storage tasks by using non-volatile memory technologies. However, in this case, RRAM arrays are used as Content Addressable Memories (CAM) to perform computations in form of look-up tables (LUT). In fact, any n-input boolean function can be encoded in an n-bit LUT by storing the truth table of the function in the LUT. For example, the addition between two n-bit values can be implemented by storing in the LUT all 2 2n input combinations. Pre-computed results are instead stored in a further memory. Then, the LUT is accessed, like a CAM, by using an input key (the combination of the two inputs) and an address is retrieved. This address is used to access the memory that stores the correspondent result of the operation. As shown in figure 12.1(C), computation is carried out with the memory to retrieve a pre-processed result, from which the name Computing-with-Memory (CwM).

12.1.4 Logic-in-Memory Approach

Finally, in this approach simple logic is directly integrated inside the memory cell, hence the name Logic-in-Memory (LiM). Differently from all other approaches, this one enables

data computation to be performed locally without the need to move data to the peripheral circuitry or outside the memory. As highlighted in figure 12.1(D), data movement is exclusively internal to the memory array. Readings are done to move data from one cell to another for computation purposes and writings are done to update a cell content after a processing task. The are few works in literature that are part of this class. Some authors propose a hybrid memory cell in which an MTJ (Magnetic Tunnel Junction) device, used as non-volatile storage, is integrated with simple CMOS logic to realize a non-volatile logic-in-memory cell. MTJs are at the base of MRAMs and they are composed of two ferromagnets separated by a thin insulator layer. The resistance of the MTJ changes depending on the relative orientation of the magnetization of the two ferromagnetic layers. In particular, in a parallel magnetization configuration the resulting resistance of the MTJ is low, while in an antiparallel magnetization configuration the resulting resis- tance of the device is high. The switching between these two configurations can be In another case authors present an architecture based on an hybrid MTJ/CMOS CAM engine for search operations. In this case, the single non-volatile logic-in-memory cell is a 3D structure in which a MTJ cell is stacked on top of simple CMOS logic. Other authors propose a modified SRAM array in which rows of logic cells (LUT- based and XOR-based) and rows of memory cells are alternated according to a memory-logic-memory-latch scheme. The latch rows are used as redundant storage cells to hold partial or final results. Another system is a hybrid approach between Computing-near-Memory and Logic-in-Memory. The proposed architecture exploits 3D integration by stack- ing DRAM on top of a logic layer using TSVs and it also adds logic inside the DRAM to perform XOR operations. More specifically, while in the other works belonging to this class logic is added directly inside each memory cell, in this work XOR engines are added outside each memory bank.

In the following chapters some of the technologies that can be used for implementing memories, logic blocks and logic-in-memory elements are being explored, without the aim of being exhaustive.

12.2 A brief introduction to magnetism

Magnetism is a physical phenomenon related to the magnetic field; from the combination of electric current and magnetic moment derives the magnetic field. All materials are influenced in some way by the magnetic field and according to their behavior can be divided in ferromagnetic, paramagnetic and diamagnetic.
Ferromagnetic have a persistent magnetic moment; paramagnetics are attracted to the magnetic field, other are repulsed, and are called diamagnetics. There are also materials which have no interactions with the magnetic field and are known as non-magnetic. The magnetic state of a material is related to the temperature, so there are more form of magnetism for the same material depending on the temperature.

12.2.1 Historical traces

Magnets at the beginning of the early civilization were called 'live rocks' because they were capable of moving without direct contact with other magnets. The ancients were also fascinated by the particular property of the amber. This material when rubbed with a cloth, is capable to attract light bodies. For long time this phenomena remain in the sphere of mysticism and in the ancient China (2500 BC) for example they were related to the symbolism of YIN/YANG so the property of attraction and repulsion were related to the natural evolution of animated and not animated materials.
The first pseudo-scientific discussion about magnetism was attributed by Aristotle to Thales of Miletus (625BC to 545 BC) who said that loadstones attracts iron because they have

a soul; so he thought that the phenomena was related to a particular form of energy that belong to the loadstone.

In ancient China the earlier reference to magnetism in the literature is in a book of the 4th century BC 'The Master of Demon Valley'in which is written 'The loadstone makes iron come or it attracts it.'
In the first's decades of year 1000, Shen Kuo, a Chinese scientist was the first that wrote about the magnetic needle compass, he introduced the concept of the true north.

In Europe we have to wait the year 1187 when Alexander Neckman describes the compass and how much is useful for navigation; in 1269 Peter Pregrinus de Maricourt wrote the first exhaustive treatise describing the properties of magnets, Epistola de magnete.
In 1600 is the turn of William Gilbert that published 'De Magnete, Magneticisque Corporibus et de Magno Magnete Tellure', this book is very important because is the first time that the Earth is modeled as a magnet, in fact Gilbert described in this book a lot of experiment with the 'terella'(figure 1.1) that is of course a small magnetized ball, representing the Earth.
Gilbert concluded that the Earth is a magnet itself, and this is the reason why compasses point north.
The next step was the understanding of the important relationship between the magnetism and the electricity and this happens with contributions from different scientist in the 18th century. The first was Hans Cristian Orsted who discovered accidentally that electric current could influence the needle of the compass; then Andre Marie Ampere found that the magnetic field circulating in a closed path depends on the current flowing in that path.
In 1820 the Biot-Savart law gives an equation for the magnetic field generated from a wire in which flow current:

$$B(r) = \frac{\mu_0 I}{2\pi r} \tag{12.1}$$

Michael Faraday, who in 1831 found that a time-varying magnetic flux through a loop of wire induced a voltage, and others finding further links between magnetism and electricity. James Clerk Maxwell synthesized and expanded these insights into Maxwell's equations, unifying electricity, magnetism, and optics into the field of electromagnetism.
In 1905, Einstein used these laws in motivating his theory of special relativity requiring that the laws held true in all inertial reference frames.
Electromagnetism has continued to develop into the 21st century, being incorporated into the more fundamental theories of gauge theory, quantum electrodynamics, electroweak theory, and finally the standard model.

12.2.2 Magnetic materials

Atoms contain many electrons, each of which spins about its own axis and moves in its own orbit around the nucleus. A magnetic moment is associated with these motions and it is: i) parallel to the axis of spin, in the first case ii) normal to the plane of the orbit, in the second case. The magnetic moment of an atom is the vector sum of all its electronic moments. There are thus two possibilities:

- No net magnetic moment: this happens when the magnetic moments of the electrons cancel each other out. This leads to diamagnetism.
- Net magnetic moment: some magnetic moments cancel each other out, but not all and so the atom is left with a net magnetic moment. Substances composed of such atoms can be para-, ferro-, antiferro-, or ferrimagnetic (see later a classification).

Depending on their magnetic moments all the materials can be divided into two classes: the ones that contains atoms having a permanent magnetic moments and the ones that do not. In the first group magnets can be classified according to the response of the magnetic material to magnetic field at different values of temperature:

- paramagnetic;
- ferromagnetic;
- ferrimagnetic.

Materials that have not permanent magnetic moment instead are called *diamagnetic*.
The constitutive relation that links together the magnetization and the applied field is

$$M = \chi_m H \tag{12.2}$$

in which χ_m is named magnetic susceptivity and has a value that depends on the family to which the material belongs.

Paramagnetism

Independently from the temperature around, the magnetic domains of paramagnetic materials have no long-range order. From the atomic point of view, this is due to the fact that their atoms have only one electron in their orbital, so the Pauli 's exclusion principle is not applied and the electron is free to align to the applied external field reinforcing it. This property allows the electron orientation in the direction of the external applied field. These materials lost the magnetization as soon as the magnetic field is removed.

Ferromagnetism

Ferromagnetism is a property of some materials to strongly magnetize under the imposition of an external magnetic field. The nearest neighbour magnetic moments have the same parallel orientation. Contrary to the paramagnetic materials, they can keep magnetization for a while until the nullification of the residual field. This class of material exhibit the important property of long range magnetic order that remains only for temperatures below a particular threshold named Curie temperature that varies depending on the material. If the temperature rises above the Curie point, the material losts its ferromagnetic properties ad behaves as it were paramagnetic.

Ferrimagnetism

In presence of external magnetic field nearest neighbour magnetic domains in ferrimagnetic materials have antiparallel orientation of magnetic moments. As for ferromagnetic material, ferrimagnetic ones also present spontaneous magnetization below Curie temperature and nothing above.

12.2.3 Ferromagnetic material properties

Ferromagnetic hysteresis loop

Ferromagnetic materials are characterized by a particular trend of the internal magnetic field as a function of the magnetic inductance. Let's suppose that we have an isotropic material, that means a material whose properties do not depend on the direction in which the sample is observed. If the material has isotropy properties, the proportionality factor between the magnetic inductance and the magnetization is a scalar, otherwise it is a tensor. The graphical representation (12.2) of this function is the hysteresis loop.

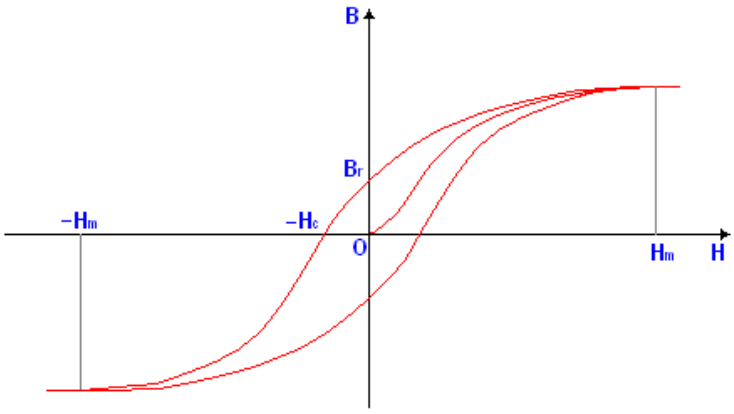

Figure 12.2: Graphic representation of the hysteresis loop

In order to understand the meaning of this curve, let's assume an initial condition in which the magnetic field is $H = 0$. Applying an external field the material is magnetized by following the *first magnetization curve* (damped line) until it reaches the saturation. When the magnetization is complete, the external field is removed, but, due the fact that the magnetic moments in these materials become ordered and parallel to each other, a low state energy is reached and the material stay magnetized until an opposite field is applied and then the demagnetization starts.

Weiss theory of ferromagnetism

Ferromagnetic materials present very strong magnetization also in absence of an external magnetic field. This means that the whole volume could be subdivided into elementary volumes, each of which is considered as isolated, so that the interactions between single spins can be considered. Materials that exhibit spontaneous magnetic moments in a defined direction have a total magnetic field that is the sum of the applied field and the *molecular* one $\mathbf{H}_m$. This field is assumed to be proportional to the thermally averaged magnetization $\mathbf{M}$ through factor λ:

$$\mathbf{H}_m = \lambda \mathbf{M}. \tag{12.3}$$

Substituting this total field into the constitutive relation that links together the magnetization and the applied field gives

$$M = \frac{C}{T}(H + \lambda M) \tag{12.4}$$

in which C is a characteristic constant of the material (*Curie constant*), H is the applied external field and T is the working temperature. The susceptibility is obtained by solving the previous equation for M/H and so it' easy to get the *Curie-Weiss law*:

$$\chi_m = \frac{M}{H} = \frac{C}{T - T_c} \tag{12.5}$$

where T_c is the Curie temperature. When the temperature rises above this threshold, the material losts its ferromagnetic properties and behaves as it was paramagnetic.

Magnetic anisotropy

Magnetic anisotropy is the directional dependence of a material's magnetic properties. It is determinant for the energy required to the domains making. Taking into account

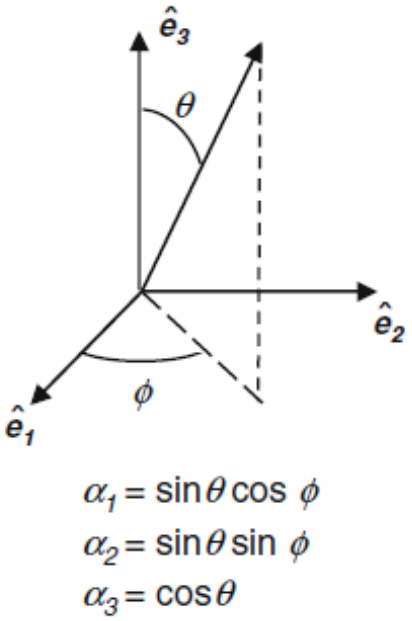

Figure 12.3: Definitions of direction cosines

these definitions, the anisotropy energy can be defined as the energy required for magnetic domains making in a specific direction. This means that there is an axis corresponding to a minimum of energy that is the most favorable direction of spontaneous magnetization. On the contrary a magnetic isotropic material has no preferential directions for the magnetic moment. In general it is useful to express the *anisotropy energy density* (the anisotropy energy normalized in order to be expressed for an elementary volume) in terms of direction cosines, defined as the normalization of the magnetization components with respect to M_s (magnetization value when the applied field is so strong that all the magnetic domains are completely oriented).
Let's assume for example that we have a three-dimensional Cartesian reference system with axis $\hat{\mathbf{e}}_1$, $\hat{\mathbf{e}}_2$ and $\hat{\mathbf{e}}_3$.
The anisotropy direction lies on the direction of the versor $\hat{\mathbf{r}}$. It's possible to identify the magnetization components along the three axis:

$$\alpha_1 = \frac{M_1}{M_S}, \qquad \alpha_2 = \frac{M_2}{M_S}, \qquad \alpha_3 = \frac{M_3}{M_S} \tag{12.6}$$

where M_s is the symble used to indicate the saturation magnetization.
In the simplest case that we can consider, the anisotropy has the major contribution on a single axis (uniaxial anisotropy), so the anisotropy energy density can be expressed as follows:

$$W_{au}(\mathbf{m}) = -Km_{\hat{e}_i}^2 \tag{12.7}$$

in which K is the *anisotropy constant* and it is derived empirically and i is an index that can assume values from 1 to 3 depending on the direction we are referring to.
The anisotropy energy density along a particular axis (let's assume for example that we need the anisotropy magnetization contribution parallel to $\hat{\mathbf{e}}_3$) can be expressed in the form:

$$W_{au} = K_{u1}(1 - M_3^2/M_S^2) + K_{u2}(1 - M_3^2/M_S^2)^2 + ... \tag{12.8}$$

The effects of anisotropy can be translated as an addictional contribution to the total field, so the *effective anisotropy field* $\mathbf{H}_k$ is defined as the variation of the anisotropy energy density with respect to the magnetization:

$$\mathbf{H}_k = -\frac{1}{\mu_0}\frac{\mathrm{d}W_{au}}{\mathrm{d}\mathbf{M}}. \tag{12.9}$$

If the sample is a cubic crystal, then the anisotropy too respects the symmetry of the whole structure. For this reason the anisotropy energy density has to satisfy the following requirements:

- W_a musts be a function of even powers of the direction cosines (the function used to express the anisotropy energy density is the cosine in order to comply with the symmetry condition), since it's not affected by the reversal of magnetization;
- by interchanging the two axes, W_a must don't vary (it's possible to build a matrix that is symmetric with respect to the diagonal).

It turns out that the anisotropy energy density for a cubic crystal is of the following form:

$$\begin{aligned} W_{ac} &= K_{c1}(\alpha_1^2\alpha_2^2 + \alpha_2^2\alpha_3^2 + \alpha_3^2\alpha_1^2) + K_{c2}\alpha_1^2\alpha_2^2\alpha_3^2 + ... = \\ &= \frac{K_{c1}}{M_S^4}[M_1^2M_2^2 + M_2^2M_3^2 + M_3^2M_1^2] + \frac{K_{c2}}{M_S^6}M_1^2M_2^2M_3^2 + ... \end{aligned} \tag{12.10}$$

The magnetization $\mathbf{M}$ can be threated as if it is composed by a static and a time-dependent term:

$$\mathbf{M} = \mathbf{M}_0 + \mathbf{m}(t). \tag{12.11}$$

Solving the equation 12.9 and substituting 12.11 the effective anisotropy field results to be:

$$H_{kc} = -\frac{2K_{c1}}{\mu_0 M_S^4}\begin{bmatrix} M_{01}(M_{02}^2 + (M_{03}^2) \\ M_{02}(M_{03}^2 + (M_{01}^2) \\ M_{03}(M_{01}^2 + (M_{02}^2) \end{bmatrix} + \bar{\mathbf{N}}^a \cdot \mathbf{m} \tag{12.12}$$

in which we indicate as $\bar{\mathbf{N}}^a$ the anisotropy tensor.

12.3 Toward a single magnet

12.3.1 Magnetic Domains and sizes

A ferromagnet is divided into a number of regions, called domains. In each domain the magnetization is in a uniform direction, which means that the magnetic moments of the atoms in the same domain are aligned with one another and point approximately in the same direction. The reason a magnetic material spontaneously divides into separate domains, rather than exist in a single domain state, is to minimize the magnetostatic energy. More in detail, the demagnetizing field affects magnetostatic energy; in order for magnetostatic energy to be reduced, the demag- netizing field has to be reduced too. The division in domains achieves exactly this, since it lowers the external demagnetizing field. Adding extra domains, however, increases exchange energy but still results in an overall lower total energy. Eventually domains will stop increasing in order to reach a balance between these contributions. The magnetization within each domain is saturated (M s) and will always lie along an easy crystallographic direction of magnetization, when there is no ex- ternally applied field, in order to reduce the magnetic potential energy. In the demagnetized state, it's possible that the ferromagnet has no net magnetization since the magnetization of different domains may cancel each other out.

Domains are alos known as Weiss domains from the scientist who developed the Magnetic domain theory, where the total sum of domains magnetization is '0'. When an external Magnetic field is applied to the magnet, the Magnetic domains are forced in the same direction, as shown in fig.12.4, and the number of rotating domains and their speed in performing it is directly proportional to the intensity of the external magnetic field.

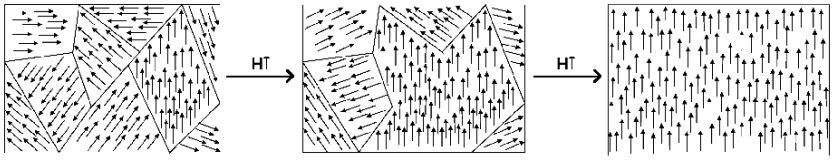

Figure 12.4: Rotation of orientation and increase in size of magnetic domains in response to an externally applied field. *Source: 4lex at Spanish Wikipedia.*

12.3.2 Domain walls

At the interface between two domains, the magnetization needs to change direc- tion from one easy crystallographic direction to the other. Such boundary regions separating magnetic domains are called domain walls. The exchange energy in a ferromagnetic is minimum when adjacent spins are parallel. A zero length domain wall would thus have a very large exchange energy associated with it. It is therefore energetically much more favorable for the direction of the magnetic moments to change gradually over several atoms, since the exchange energy between adjacent atoms would decrease. However the spins within the wall are now pointing away from easy directions and so the crystal anisotropy energy within the wall is higher than it is in the adjoining domains. In short, exchange energy tends to make walls as wide as possible in order to reduce exchange energy between adjacent atoms, while on the contrary crystal anisotropy tends to make the wall as thin as possible in order to reduce the number of spins pointing in non-easy directions. As a result of this competition, the wall in general has a nonzero width and a definite structure. The wall energy is given by the sum of the exchange and anisotropy energies, in- tegrated over the wall.

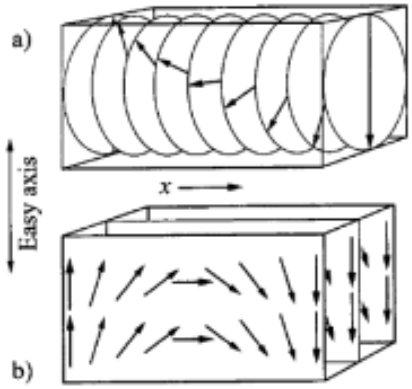

Figure 12.5: Variation of the magnetization in (a) a Bloch wall or (b) a Néel wall in a planar film where the magnetization in the domain is parallel to the film plane. Adopted from L Dennis et al..

Two one-dimensional wall types have been found both numerically and experi- mentally:

- Bloch walls: the wall spins rotate within the plane of the wall;
- Néel walls: the wall spins rotate in the plane perpendicular to the plane of the

wall; or, in other words, the component of the magnetization perpendicular to the wall changes during the rotation. These two wall types are limit cases of more complex, higher dimensional, walls. The higher dimensional walls can, in other words, be seen as a combination of these two basic types. Bloch walls are generally favored, because of the already introduced topic of minimizing magnetostatic and exchange energy. In practice, Bloch walls are favored in infinite or bulk samples, while Néel walls can be favored in thin films and

in applied fields. Other possible reasons for which a Bloch wall might not be favored are presence of inclusions, voids, dependence of wall energy on orientation, internal stress. Some pictures of the two types are in figures 12.6 and **??**.

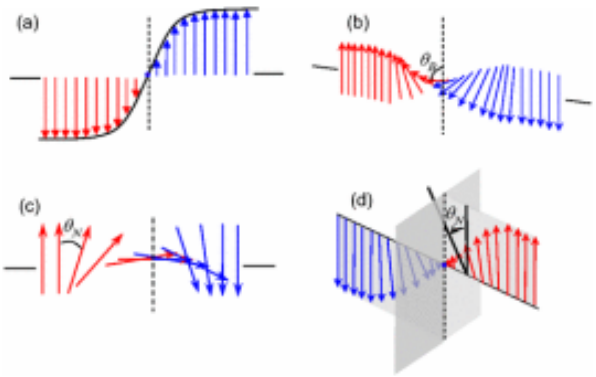

Figure 12.6: Different types of domain walls: (a) Ising type, (b) Bloch type, (c) Néel type, and (d) Mixed Ising-Néel type walls. A mixed Ising-Bloch type would look similar to (d) except that the rotation would be out of the plane of the polarization vector. Adopted from Lee et al..

12.3.3 Shrinking the magnet size

Shrinking the magnet sizes, make it possess less magnetic domains, and 100 nanometer smaller magnets have only one domain, as shown in fig.12.7. Magnets which are too small (less than 15 nm) will show a super-paramagnetic behavior, meaning that they will polarize themselves even when the external magnetic field is very small, hence also the magnetic noise will be enough, making these structure unable to retain their state in computational environment, since they will polarize easily in a random state. This means that for our purposes, magnets with dimensions in the range $[100 - 15]$nm must be used.

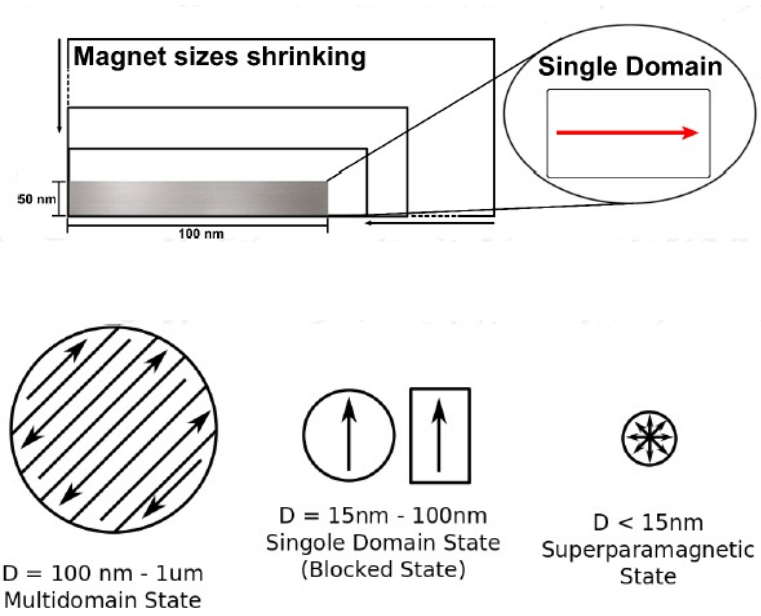

Figure 12.7: Magnetic sizes shrinking and Magnetic related behavior.

To sum up, it is possible to have different Domain states (shown in fig.12.8):

- **Multi-domain State** Magnet behavior depends on hysteresis cycle. Several possible magnetization states.
- **Single-domain State** Hysteresis cycle changes due to anisotropy influence. Only two stable states become available.
- **Super-paramagnetic State** State reached when magnet sizes are reduced beyond a certain limit. Super-paramagnetic limit depends on material type. The magnetic anisotropy (see Chapter 12.3.4 for more details) is overcome by thermal noise. The coercivity (see Chapter 12.3.4 for more details) is '0', magnetic moment continuously change.

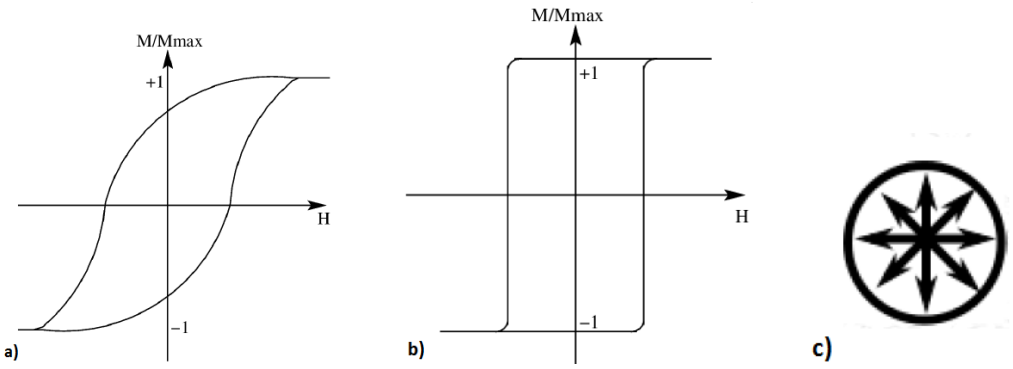

Figure 12.8: Magnetic States: In **"a"** the hysteresis curve of a Multi-Domain magnet. In **"b"** the hysteresis curve of a Single-Domain magnet. In **"c"** a Super-paramagnetic state.

12.3.4 Magnetic Anisotropy, Remanence and Coercivity

Magnetic Anisotropy

The *Magnetic Anisotropy* is a basic trait of magnetic structures. It is the ability of the magnetic moments to align themselves with an "easy axis", which is an energetically favorable direction of spontaneous magnetization. The anisotropy can be of different natures:

- **Shape anisotropy** It is given by magnet sizes. Magnetization lies along the longer magnet side. Shape anisotropy is caused by the shape of a mineral grain. If the specimen were spherical, the same applied field would magnetize it to the same extent in any direction. If however the specimen were not spherical, then it would be easier to magnetize it along a long axis than along a short axis. This happens because of the demagnetizing field. The demagnetizing field is produced by the distribution of surface charge on a magnetized body. This means that the applied field along a short axis would need to be stronger than the one applied along a long axis, in order to result in the same actual field inside the specimen. The shape anisotropy energy is related to the difference in energy ΔE when the sample is magnetized along its hard and easy directions.
- **Magneto-crystalline anisotropy** It is given by the atomic structure of a crystal that introduces preferential directions for the magnetization. A ferromagnetic material is said to have magnetocrystalline anisotropy if it takes more energy to magnetize it in certain directions than in others. These directions are usually related to the principal axes of its crystal lattice. It will be shown later that applying a field can cause a domain wall in the crystal to move. This happens because applying a field H in a certain direction increases or reduces the potential energy of atoms in domains, therefore causing some domains to expand and others to reduce. In other words, continued application of such a field will eventually result in the elimination of all domains but the favored one (the one with lowest magnetic potential energy) and the

crystal will be saturated (i.e an increase in the applied field H would be unable to increase the magnetization further). If the material has magnetocrystalline anisotropy, it will be found out that, depending on the orientation of the applied field with respect to the crystal lattice, a higher or lower magnetic field is needed to reach the saturation magnetization. In particular: i) the easy axis is the direction along which a small applied magnetic field is sufficient to reach the saturation magnetization; ii) the hard axis is the direction along which a larger applied magnetic field is needed to reach the saturation magnetization. Crystal anisotropy can so be considered as a force which tends to hold the magnetization in certain equivalent crystallographic directions in a crystal. It results from the interaction of the spin magnetic moment with the crystal lattice (spin- orbit coupling). The applied field must do work against the anisotropy force to turn the magnetization vector away from an easy direction. Crystal anisotropy energy E_a is therefore defined as the energy necessary to deflect the magnetic moment in a single crystal from the easy to the hard direction.

- **Exchange anisotropy** It is given by the interaction of anti-ferromagnetic and ferromagnetic materials. Exchange anisotropy happens due to exchange forces. In general, since the ex- change energy for neighbouring atoms depends only on the angle between their spin magnetic moments, it does not give rise to anisotropy. However, in mag- netic multilayers, exchange anisotropy can occur at the interface of two magnetic materials, due to exchange coupling between the spins of the two materials.
- **Stress anisotropy** It is given by a mechanical stress applied to the magnet. Magnetization lies along the applied stress axis.
- **Induced anisotropy** Anisotropy can be induced in certain materials by:
  * Magnetic annealing: a disordered alloy is put in a magnetic field at high temperature. This process rearranges the atomic-scale texture of the alloys, and can induce anisotropy. It can also improve the alloy's ferromagnetic properties.
  * Stress annealing: combines heat treatment and an applied stress.
  * Plastic deformation: can induce uniaxial anisotropy in certain alloys.
  * Magnetic irradiation: properties of the material are changed via bombardment with neurons, ions (FIB), electron on gamma rays. The effect depends on which of those is used. In general what is changed is mechanical strength, hardness and even the hysteresis loop itself. It can also make some materials magnetically softer. These effects happen because bombardment causes atomic rearrangements (this is called radiation damage): some atoms are displaced into interstitial positions and leave behind vacancies.

Magnetic Remanence

The *Magnetic Remanence* is the magnetization left behind in a ferromagnetic material after an external magnetic field is removed. It also provides the magnetic memory in magnetic storage devices.

Magnetic Coercivity

The *Magnetic Coercivity* is a measure of the ability of a ferromagnetic material to withstand an external magnetic field without becoming demagnetized. Ferromagnetic materials with high coercivity are called magnetically hard materials, and are used to make permanent magnets. Materials with low coercivity are called to be magnetically soft and are used in transformer and inductor cores, recording heads, microwave devices, and magnetic shielding. In fig.12.9 it is shown the Magnetic Coercivity in relation to the radius of nanoparticles while in fig.12.10 a curve showing a family of hysteresis loops highlighting the coercivity and remanence is depicted.

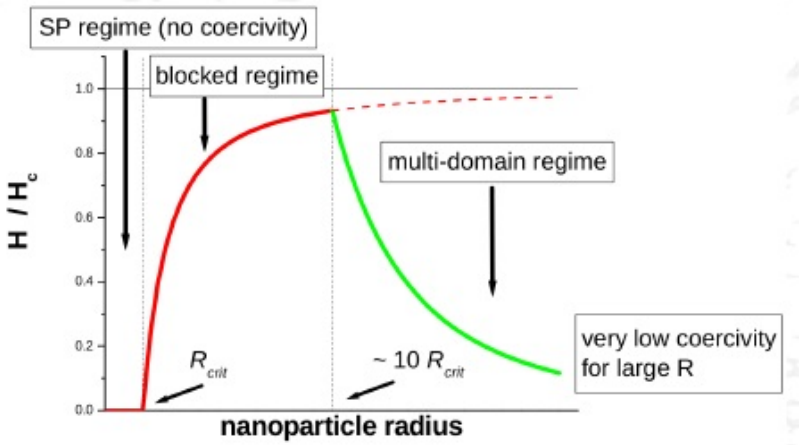

Figure 12.9: Magnetic Coercivity vs Nano-particles radius.

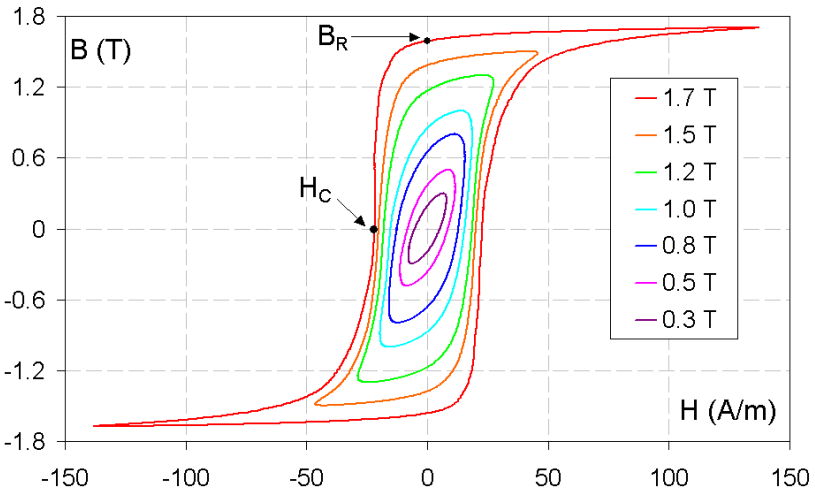

Figure 12.10: A family of hysteresis loops for grain-oriented electrical steel. B_R denotes retentivity and H_C is the coercivity. The wider the outside loop is, the higher the coercivity. Movement on the loops is counterclockwise. *Source: Zureks - Own work.*

CHAPTER 13

Magnetization dynamics: LLG equations and DW dynamics

13.1 Magnetic dynamics

Depending on the length scale of the structures one is dealing with, different approaches and theoretical physics models are used in order to predict and describe the behaviour of ferromagnetic materials. The following list shows in detail which are these estabilished models:

- **Atomic level theory** : this is the approach used for structures having a length scale $< 1\mu m$;
- **Micromagnetic theory** : this is the approach used for structures having length scale varying from $1nm$ to $1000nm$;
- **Domain theory** : this is the approach used for structures having length scale varying from $1\mu m$ to $1000\mu m$;
- **Phase theory** : this is the approach used for structures having length scale $> 0.1mm$

13.1.1 Static micromagnetism

Micromagnetics is the field of physics that deals with the magnetic behaviour of the magnets in sub-micron length scale. Currently it seems that the only realistic approach is to ignore the atomic nature and to use classical physics in a continuum description of a magnetic material, based on the formulation of the energy of the system in terms of continuous magnetization vector field $\mathbf{M}$. This model has the aim to understand which is $\mathbf{M}$ spatial distribution. A first simplification is the assumption of working below the Curie temperature, so that the module of the magnetization $|\mathbf{M}|$ can be considered equal to the saturation value $\mathbf{M_S}$ in the whole structure. The problem now is reduced to find the orientation $\mathbf{m}$, by minimizing the magnetic energy. The total energy of a ferromagnet with respect to the magnetization is influenced by a multitude of physical effects:

- exchange energy E_{exch};
- anisotropy energy E_{anis};
- Zeeman energy E_Z;
- demagnetization energy E_{demag};
- magneto-elastic energy E_{m_e}.

For this reason the total energy is defined as the sum of all these contributions:

$$E = E_{exch} + E_{anis} + E_Z + E_{demag} + E_{m\_e}. \tag{13.1}$$

Exchange energy

The elementary magnets in ferromagnetic materials are subject to the so-called *exchange interaction*, that is a quantum mechanical effect having origin in electrostatic interactions and Pauli principle. It occurs between identical particles and has a particular energy (energy exchange). This effect leads to a most energetically favorable alignment of the neighbouring spins, so in ferromagnetic materials it gives its contribution to domains alignment in ferromagnetic and antiferromagnetic material. The origin of the energy exchange $\mathbf{H_{ex}}$ between two electrons can be described by using the *Heisenberg Hamiltonian* interaction:

$$\mathbf{H_{ex}} = -2\frac{\mathbf{J}}{h^2}\mathbf{S_1} \cdot \mathbf{S_2}. \tag{13.2}$$

where $\mathbf{J}$ is the exchange constant, $\mathbf{S_1}$ and $\mathbf{S_2}$ are the spin momentum opertors and h is the Planck constant.

Anisotropy energy

As explained in the previous chapter, the anisotropy depends on the crystal structure of the material and energetically favors the parallel magnetization alignment to certain axes (easy axes). The anisotropy energy can be expressed as follows:

$$E_{anis} = \int_V W_a(\mathbf{m})\, dV \tag{13.3}$$

in which $W_a(\mathbf{m})$ is the anisotropy energy density as a function of the orientation of the magnetization and V is the whole volume of the considered ferromagnet.

Zeeman energy

Zeeman energy refers to the external field energy. It is the interaction between the magnetization and the externally applied field. The Zeeman energy allows the magnetization to align parallel to the applied field H_a and can be expressed in the following form:

$$E_Z = -\mu_0 \int_V \mathbf{M} \cdot \mathbf{H_a}\, dV. \tag{13.4}$$

Demagnetizing Energy

The demagnetizing field is an internal field created by the magnetic sample upon itself. It is due to the fact that the media is not infinite. The external applied field leads to the formation of "poles" at the surfaces of the magnetized material. An internal magnetization field $\mathbf{H_d}$ is formed with an opposite direction with respect to the external magnetization. H_d is proportional to the magnetization $\mathbf{M}$ through the demagnetization factor D:

$$\mathbf{H_d} = D \times \mathbf{M}. \tag{13.5}$$

As can be understood by looking at the figure 13.1, the effect of the applied filed $\mathbf{H_{ext}}$ is reduced by this quantity, so the total field turns out to be:

$$\mathbf{H} = \mathbf{H_{ext}} - \mathbf{H_d}. \tag{13.6}$$

Magnetoelastic Energy

The last contribution is given by the magneto-elastic energy that represents the energy stored by the ferromagnetic sample because of the lattice distortion.
All these contributions are added together in order to define the effective field H_{eff} acting on the whole structure.

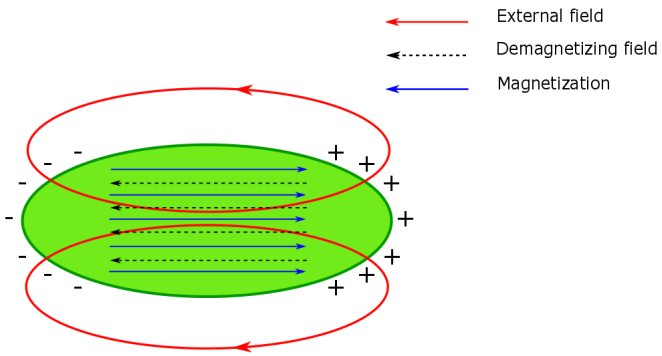

Figure 13.1: Demagnetizing field

13.1.2 Landau-Lifshiftz-Gilbert equation

When a ferromagnetic material is put in a magnetic field, each electron spin tends to orientate along the direction of the external field in order to minimize the total system's energy. Nevertheless, because of the kinetic energy that acts against the equilibrium tendency, the result is that spins line up with the applied field following a precession motion that can be described by Landau-Lifshitz-Gilbert equation. Because of the two conflicting forces acting on the single electron, the resultant torque is given by:

$$\vec{\Gamma_e} = \vec{\mu_e} \times \mu_0 \vec{H} \tag{13.7}$$

where $\vec{\mu_e}$ is the magnetic momentum of the electron, μ_0 is the vacuum magnetic permeability and $\vec{H}$ is the magnetic field. From the Euler's second cardinal equation, we know that the mechanical momentum of the external forces is equal to the first derivative of the angular momentum with respect to time. If $\vec{J}$ is the angular momentum, it's possible to write:

$$\vec{\Gamma_e} = \frac{d\vec{J}}{dt} \tag{13.8}$$

where $\vec{J}$ is defined as

$$\vec{J} = \frac{h}{g\mu_B}\vec{\mu_e} = \frac{1}{\gamma_0}\vec{\mu_e} \tag{13.9}$$

where h is the reduced Planck constant, μ_B is the Bohr magneton and γ_0 is the gyromagnetic ratio. γ is equal to $\gamma_0\mu_0$, so it is possible to rewrite the torque equation in the following form:

$$\frac{d\vec{\mu_e}}{dt} = -\gamma\mu_e \times \vec{H}. \tag{13.10}$$

This result can be extended to all the electrons of the ferromagnetic films, that means that it is allowed to write the total magnetization as:

$$\frac{d\vec{M}}{dt} = -\gamma M \times \vec{H}_{eff}. \tag{13.11}$$

$\vec{H}_{eff}$ represents the sum of all the magnetic field contributions (demagnetizing field, exchange interactions, external field...).

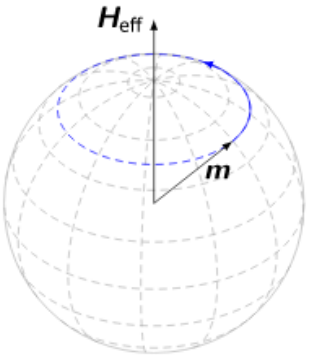

Figure 13.2: Precession motion around the applied external field

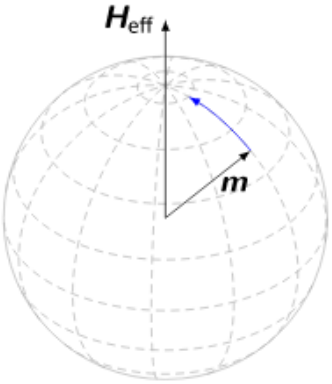

Figure 13.3: Damping effect

This equation is only ideal, because it doesn't take into account the damping of this precession motion that derives from interaction of the electrons with the crystalline lattice and other factors that contribute to the relaxation of the system, that otherwise will precess forever. Because of these non-idealities, the previous equation is rectified by inserting a second term that take into account the damping. In according with Gilbert considerations, the damping effect can be seen as a field component related to the time variation of the magnetization. This allows to rewrite the previous formula in the following form, by keeping a viscous damping approach:

$$\frac{d\vec{M}}{dt} = -\gamma\vec{M} \times (\vec{H}_{eff} - \eta\frac{d\vec{M}}{dt}). \tag{13.12}$$

The coefficient η is the damping constant that is set in order to have the parameter $\alpha = \eta\gamma M_s$ dimensionless. As this equality is valid

$$\vec{M} \times \vec{H}_{eff} = \frac{1}{\gamma}\left[\frac{d\vec{M}}{dt} + \frac{\lambda}{{M_s}^2}\vec{M} \times (\vec{M} \times \vec{H}_{eff})\right] \tag{13.13}$$

it's easy to get the final Landau-Lifshitz-Gilbert equation:

$$\frac{d\vec{M}}{dt} = -\gamma(\vec{M} \times \vec{H}_{eff}) + \frac{\gamma\alpha}{M_s}\left[\vec{M} \times (\vec{M} \times \vec{H}_{eff})\right]. \tag{13.14}$$

This means that the system will relax until the magnetization $\vec{M}$ becomes parallel to $\vec{H}_{eff}$. Thanks to this formula, it's possible to predict the evolution over time of the magnetic configuration of a material subject to an external field.

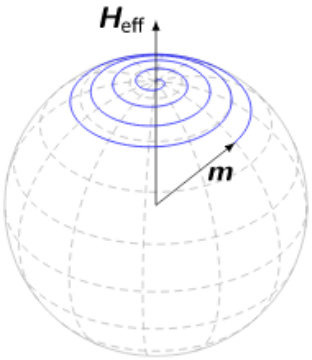

Figure 13.4: Graphic representation of the magnetization vector dynamics according to Landau-Lifshiftz-Gilbert equation

13.2 Spin polarized currents and STT

In normal materials, electron spins are present in equal way and randomly dis- tributed in an equilibrium state. However, in ferromagnetic materials electron spins are aligned spontaneously and this can re- sult in a net magnetic moment for the whole sample: there is asymmetry in the density of states (DOS) at Fermi energy for spin up and spin down, which is also what causes the spin transport:

- If an unpolarized current passes through a normal metal, since the density of the two states is the same, the electrons have the same scattering rate and the current stays unpolarized.
- If an unpolarized current passes through a ferromagnetic material, the density of the states being different, one of the two states may encounter less scat- tering, or suffer other effects, compared to the other state. In this case the conductivity due to the majority spin channel would be higher and the current leaving the ferromagnetic material would be spin polarized

The electron spin polarization P is defined as:

$$P = \frac{DOS(\uparrow) - DOS(\downarrow)}{DOS(\uparrow) + DOS(\downarrow} \tag{13.15}$$

where $DOS(\uparrow)$ s the density of the spin-up state and and $DOS(\downarrow)$ is the density of the spin-down state. When spin-polarized electrons pass through a magnetic domain wall the spins of the charge carriers rotate to follow the local magnetization. In short, the magnetization of the ferromagnet changes the flow of spin-angular momentum by exerting a torque on the flowing spins to reorient them, and so the flowing electrons must too exert an equal and opposite torque on the ferromagnet. This torque is called spin transfer torque STT.

13.3 Magnetization dynamics in presence of STT

STT is found to be made of two main contributions

$$T = T_{AD} + T_{FL}$$

where T_{AD} called antidamping torque an T_{FL} field-like torque. Other names for them are adiabatic and nonadiabatic contributions. The initial response of the DW in presence of a STT depends on which of the two contributions dominates. It was also found that the adiabatic STT dominates for large cur- rent densities, while the non-adiabatic STT dominates at low current densities: it is thus the required one to make DW motion practical.

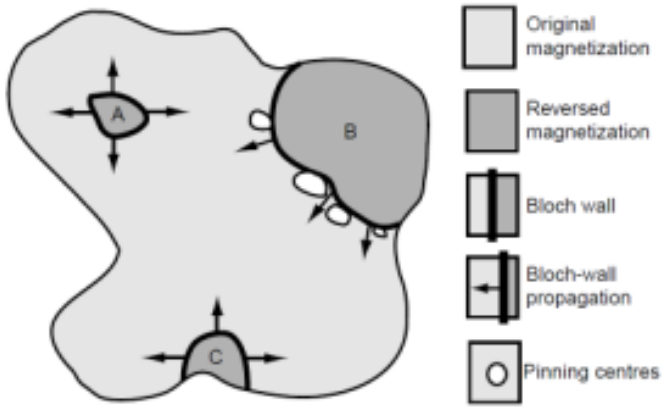

Figure 13.5: Processes involved in magnetization reversal in the second quadrant of the hysteresis loop. A is a reverse domain which nucleates in the bulk at a defect, or from a spontaneous thermal fluctuation. B is a reverse domain which has grown to the point where it is trapped by pinning centres and C is a reverse domain which nucleates at a surface asperity. Adopted from [X].

There is a threshold current under which steady DW motion doesn't happen, and above which the DW start moving. In general, velocity varies linearly (this also depends if there is a Magnetif field applied, see next chapter for a model in this case).

There is however a upper limit to the maximum velocity that can be reached. Sufficiently high current densities make it so the torques are strong enough to deform and transform the spin structures of the domain walls; these effects influence the domain wall velocity. This effect is called Walker breakdown. It was found that the DW can be moved by current pulses and that the distance they move varies linearly with the length of the pulse.

STT presence influence the dynamics modeled by LLG equations. Acutally if the current is big enough the damping effect is counterbalanced and this can result in stable precession of a switching. This is used in Racetrack memories (see next chapter).

13.4 Domain wall nucleation and reversal by means of an external field

As seen in the following chapters, a magnetic field can be used in order to nucleate a domain wall. Magnetization reversal is initiated in a small nucleation volume around a de- fect or surface asperities, as they are sources of strong local demagnetizing fields. Once a small domain has formed, the wall propagates outwards, growing from the nucleation volume or otherwise becomes pinned at some other defect.

The simplest model of magnetization reversal is the Stoner-Wohlfarth model, which assumes a coherent mode 3 of magnetization reversal. A Stoner-Wohlfarth particle is a uniformly magnetized ellipsoid (fiugre 13.6) with uniaxial anisotropy in a field ap- plied at an angle α to the anisotropy axis.

The total energy density is then:

$$E_{tot} = E_{ani} - \mu_0 M H cos(\alpha - \theta) \tag{13.16}$$

where E_{ani} is the anisotropy energy, and the second contribution is due to the applied field, with θ being the angle of the magnetization M with respect to the anisotropy axis. By minimizing with respect to θ two minima are found; hysteresis arises between the two minima.

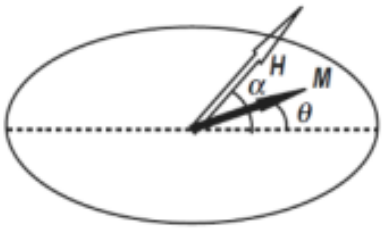

Figure 13.6: A Stoner-Wohlfarth particle. Adopted from [X].

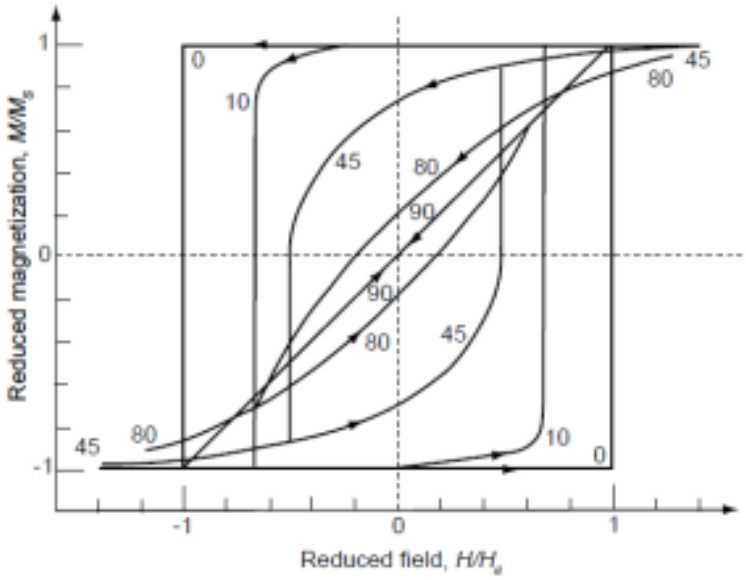

Figure 13.7: Magnetization curves for the Stoner-Wohlfarth model for various angles α between the field direction and the easy axis. H is given in units of the anisotropy field Ha. Adopted from [X].

The hysteresis varies as a function of α. In particular: (i) when $alpha = 0$ the hysteresis loop is perfectly square and the coercivity is equal to the anisotropy field; (ii) when $\alpha = \pi/2$ there is no hysteresis loop (figure 13.7).

The nucleation field H_n is defined, considering a uniformly magnetized ellipsoidal particle, as the field which causes the first nucleation to happen and thus the first difference from the uniformly magnetized state to appear (see in the next chapter on PNML a simple model).

CHAPTER 14

In plane Nano Magnetic Logic

Nano-Magnets implements the FCN principle being able to stay in one of the two possible minimum energy states at time, encoding the logic '0' and '1' as shown in fig.14.1, where single-domain nanomagnets are used to represent logic values. They are also the only *FCN* implementing Technology that can be fabricated today with the modern photo-lithography used to realize CMOS based dies.

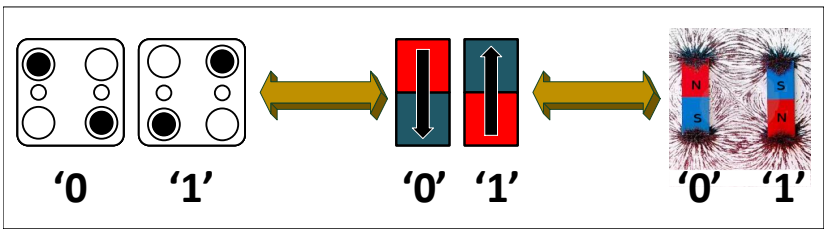

Figure 14.1: NML Logic-Magnetic States as FCN cells.

NML technology is then based on magnets that contains only a single magnetic domain. Nanomagnets are tiny bar magnets, that generate stray field, this can be used to couple with other nearby magnets; if are used for data storage of course, the strong coupling, it is undesirable, but to perform logic operations is indispensable.

The single domain behaviour is a condition that depends on size and shape of the sample, the structure are in single domain if their dimensions go approximately from few hundred to tens of nanometers; above this bounds, the magnet splits in multi domain loosing its strong fringing fields needed for coupling; this phenomenon happens because, over a certain size, the total energy necessary to remain in a single domain state is a lot large than the energy needed to be in multi domain state, so the matter as always will search the minimum energy equilibrium and will split up in multi domains; under tens of nanometres the magnet is too sensible to thermal fluctuations and have no more a stable state, will be a supermagnet.

In iNML the easy axis of magnetization depends mainly on the shape of the magnets. This magnet have an elongated shape from witch depends the magnetic shape anisotropy so they preferred direction of magnetization coincide with it. figure 14.2 shows an example of antiferromagnetic wire consisting of 16 dots. The dots are made from a 30 nm permalloy film using an electron beam lithography(EBL) and lift-off, so the same techniques used in the CMOS production.

In the figure there is the visualization with three type of different microscope; scanning electron microscope(SEM) and atomic force microscope(AFM) are used to see the structure of the dots while, magnetic force microscope(MFM) is useful to see the magnetic contrast. The dot on top right impose the order of the other ones in a domino like effect resulting, at the end of the process, in a antiferromagnetic ordered chain.

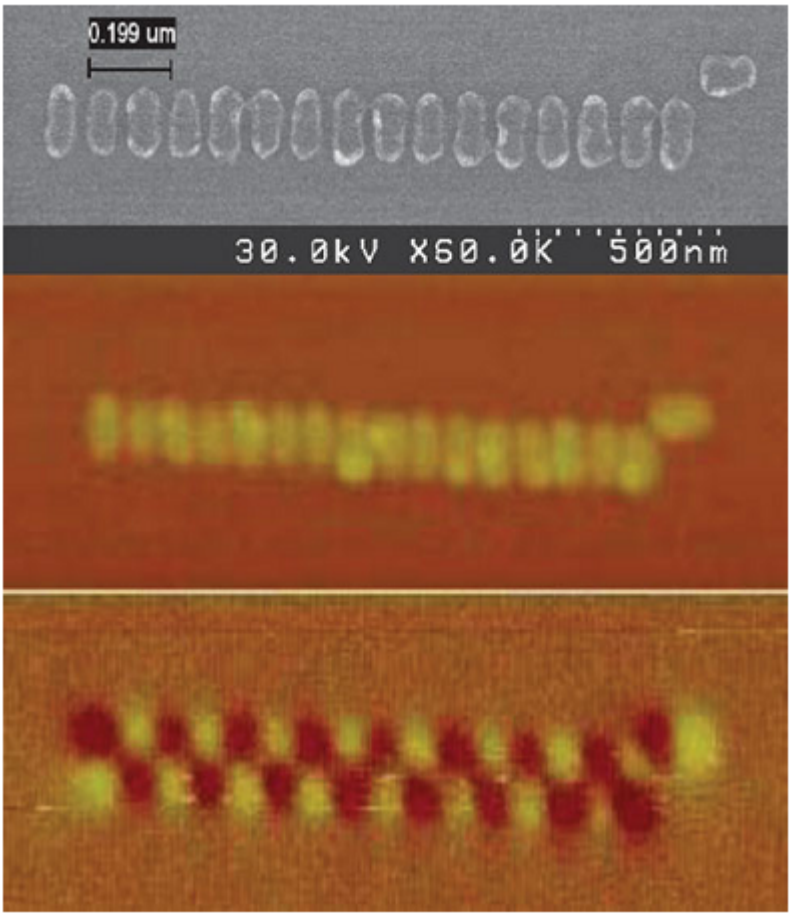

Figure 14.2: iNML wire scanned with scanning electron microscope(SEM), atomic force microscope(AFM), magnetic force microscope(MFM). Figure taken from[146]

Building circuits in Nano-Magnet Logic involves both pros and cons. The advantages and disadvantages of this technology are summarized in the following.

Advantages:

- **Logic-In-Memory** The same device can be used as a computational element but it also retains its state if not forced to change it. Hence it can act both as a logic circuit and a memory.
- **Low Power Consumption** No static power consumption. Dynamic power consumption up to 20 times lower than ultra-scaled CMOS.
- **Radiations and Heat Robustness** Total immunity to any kind of radiations. High heat resistance. Ideal for space and military applications.
- **Compatible with up to date fabrication processes** Using the same photo-lithography process already used to fabricate CMOS based dies.
- **Possibility to build multilayer circuits** Up to now, experimental results are available for three layers circuits.
- **High speed reachability** Advanced magnetic structures (SpinWaves) can work at hundreds of GHz.

Disadvantages:

- **Limited speed** If using pure NML implementation.
- **Dynamic power consumption** It is related to the clock technology. Hence, it can be very high (Resistive Clock wires) or very low (Magneto-Elastic Clock)

– **Clock technology constraints circuits layout** This will increase the circuit area raising the Power Consumption of the Clocking Mechanism [1].
– **Wasted circuit area** Due to Interconnection overhead.

14.1 In-Plane Nano-Magnet Logic *iNML* and the clock mechanism

iNML is the abbreviation used to indicate Nano-Magnets whose magnetization vector lyes aligned in the long axis due to its magnetic shape anisotropy. In fig.14.3 there are shown the representations of the binary states plus the reset one.

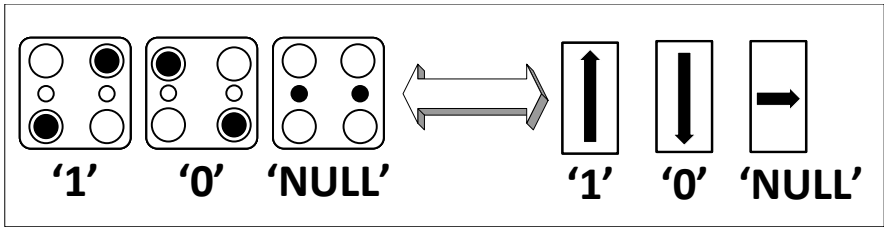

Figure 14.3: iNML logic states representation.

The design of circuits based on iNML requires that magnets are placed on a plane (or onto different planes one over the other, in *Multi-Layers* designs), then input signals, magnetic fields, are introduced to interact with input magnets of the circuit to start the data computation. Since the magnetic field generated by the input magnets is not strong enough to force the other magnets to assume their next logic state, an external magnetic field, the clock, is needed to lower the magnetic coercivity of the cells in order to make them more sensible to the input magnetic field. This clock, hence, has the same function explained in previous chapterd for generic FCN. Therefore, the clock signal will force the magnets in an unstable state, then the input magnetic field will be high enough to force the magnet to assume the corresponding minimum energy stable state, then, the clock is removed to make the magnet retain that state and be insensible to input signal variations (thermal noise included). Using the clock, the magnets in the circuit will start to switch in a domino-like effect, being the clock applied to different zones with a certain phase shift in order to favor the signal propagation toward a specific direction. In fig.14.4 it is shown the changes of the magnetic states into a magnetic wire during the application and removal of the clock signal. The clock gives to the circuit an intrinsic pipelined behavior.

There are limitations in the number of consecutive magnets that can switch simultaneously. This happens because the thermal noise will interfere with the input signal, and since the latter intensity is inversely proportional to the distance, after a certain number of magnets, the thermal noise intensity, which is almost uniform, will overcome the former one, inducing the magnets to assume random state, therefore errors in computation, as shown in fig.14.5. This problem is coherent with the one of *FCN* cell previously explained. The solution is to use multiphase clock signal as the *4-phases clock mechanism*. It must be noticed that using this kind of clock mechanism, the different phased clock signal must be overlapped to avoid back signal propagation.

For iNML a three-phase clock is studied[**?**]; in this system the clocking mechanism is based on three state:

– **Reset** state, magnetic field applied
– **Hold** state, no magnetic field applied

[1] Increasing the Area, the length and the number of clocking wires increase too.

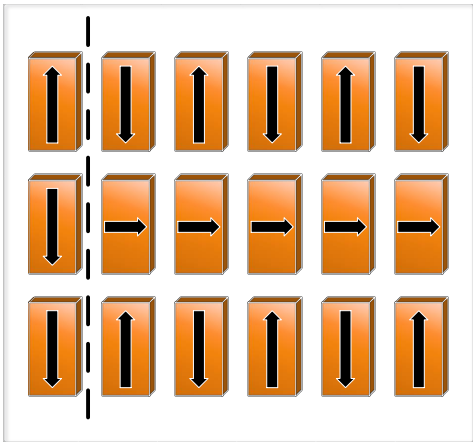

Figure 14.4: iNML wire switching under clock appliance and removal principle. The magnet at the extreme left side is the input one. In the upper image, the wire is in memory state. In the middle one, input changes and the wire is under clock appliance (unstable state). In the bottom one, the clock signal is removed and the magnets have switched in a domino-like effect assuming the correct states.

Figure 14.5: iNML wire switching: limitations in consecutive correct switching magnets under thermal noise effect. Green margined magnets are the one which are correctly switching, while the red ones are introducing errors.

– **Switch** state, magnetic field slowly removed

Consider the wire in figure 14.6 a) if the first dot switch, the second dot will remain in the same direction because the magnetic stray field of the first dot is not strong enough. A solution can be to apply a magnetic field that force the other dots to be in a RESET state; this state is unstable so, when the external magnetic field is removed, the other dots will switch reaching an antiferromagnetic order and propagating so the input value; the bad news is that only a limited number of dot, in cascade, can switch correctly during the phase of antiferromagnetic realignment[147].
This problem can be solved dividing the circuit in small areas where only a limited number of dot is present, for each zone a clock is applied.

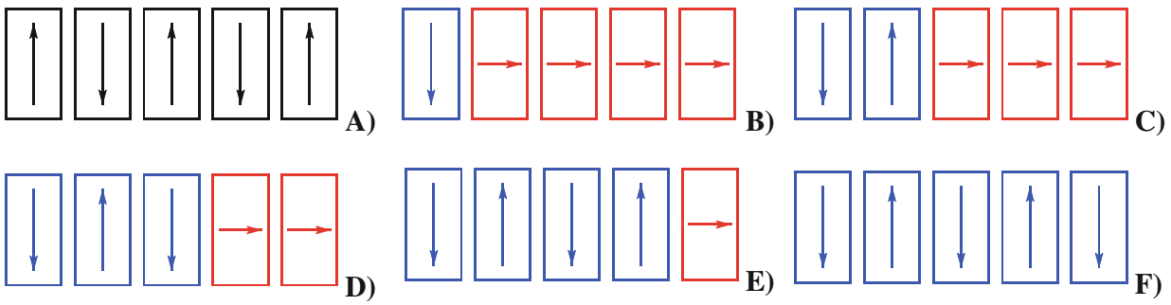

Figure 14.6: Clocking for iNML. a) antiferromagnetic ordered line. b) new input applied and the other dots(red ones) are in the reset state. c) d) e) f) realignment of dot when the magnetic field is removed. Figure taken from[148]

Figure 14.7 illustrates a mechanism that uses three-phase clock each applied to a different region of the circuit and the signals have a phase difference of 120°.
When a clock region is in the RESET state, the magnetic field is applied so, the magnets feel the inputs of the HOLD region that behaves like input for the magnets in the RESET zone; when the magnetic field is slowly removed(SWITCH) the magnets will align following the input imposed bye the HOLD phase.

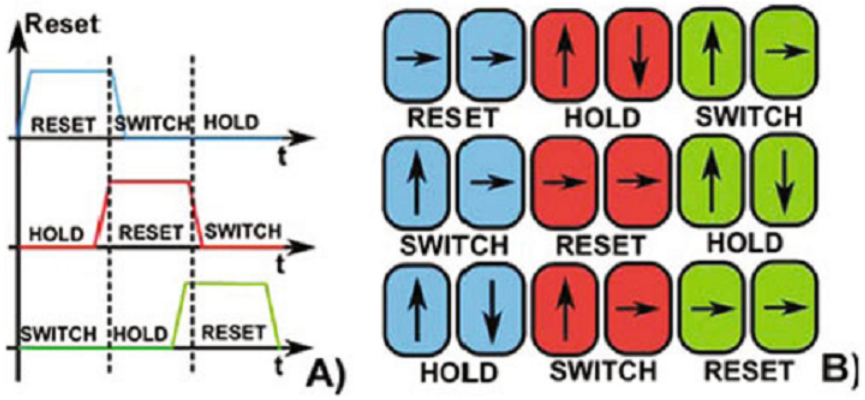

Figure 14.7: Three-phase clock. a) Waveform of the three different clock with a difference in phase of 120°. b) signal propagation trough the different clock zones. Figure taken from[148]

The SWITCH zone have on the left HOLD, on the right the RESET zone; with this mechanism not only the correctness of information propagation is ensured, but also the unidirectionality since the RESET state on the right of the SWITCH zone, have no influence on it.

14.1.1 Different Physical Clock Implementations

Several Physical implementations of the Clock have been studied in order to lower its Power Consumption and reduce the physical layout constraints of the design. The most important to briefly review are the following ones:

- **Magnetic Field Clock** Where the Clock Layout can be:
  Snake Clock
  Parallel Clock Wires
  Virtual Clock The most used since it simplify the feedback realization without wasting so much area of the circuit as the *Snake Clock* does.
- **Spin Hall Effect Clock** Based on materials, like *Tantalum*, which possess the physical property of showing high *Spin Angles*.
- **Magneto-Elastic Clock** Based on Piezo-electric materials.

On-chip Magnetic Field Clock generation

The magnetic field, clock,is generated by a current flowing through a wire placed under the magnets and a ferrite joke is used to confine it. A picture is shown in fig.14.8.

This Clock Mechanism produces circuit layout constraints, since each clock wire is associated to a clock zone and their placements is related to technological constraints. In addiction to this, the clock zone layout must allow *NML* signal propagation both forward, to guarantee transfer in-Out of data, and backward, to allow the realization of feedback signals.

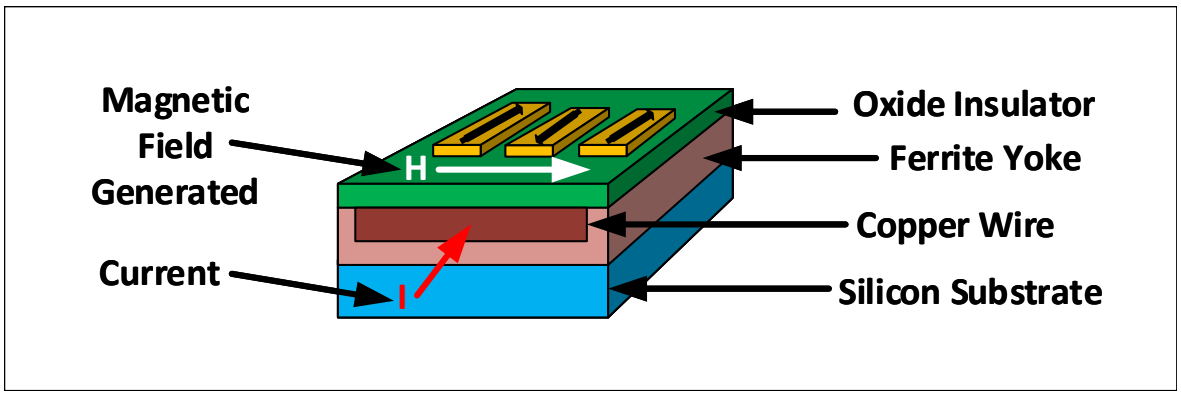

Figure 14.8: iNML Clock Mechanism: On-chip Magnetic Field Clock generation.

Snake Clock

The idea is that the clock wires in the circuit are, in some nodes, twisted to create a different *zones* order. This allow the signal to go back passing through backward oriented *zones*. This implies a lot of circuit wasted area, since there are limited areas in which signal can change its direction and magnets must reach that particular node to go back. A picture is shown in fig.14.9.

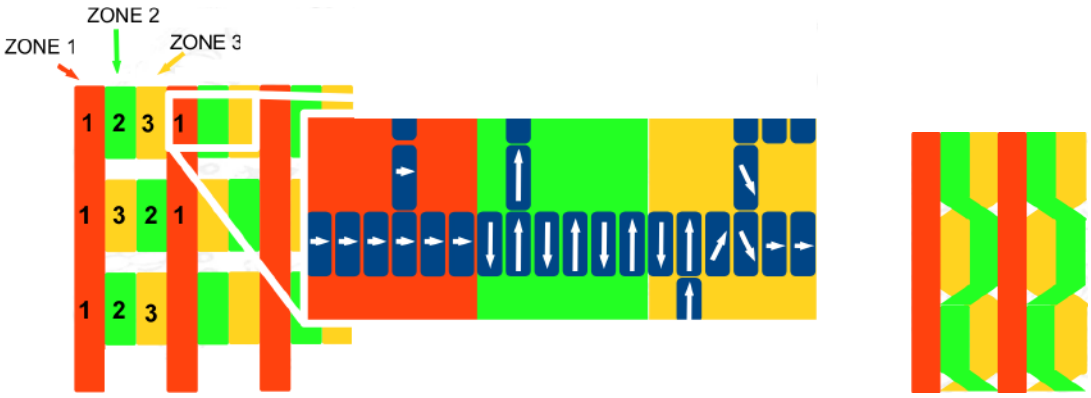

Figure 14.9: iNML Snake Clock: At left the Circuit zone Layout and at right the twisting of the clock wires.

Parallel Clock Wires

This implementation avoids the wasting of area introduced by the *Snake Clock* creating more compact circuits. The problem is given by the fact that feedback becomes impossible to realize, since information can propagate only in one direction. A slight modification is to twist the clock wires only when strictly necessary. A picture is shown in fig.14.10.

Virtual Clock with 4 phases

The idea is to use magnets with different aspect ratio. This because bigger magnets need stronger magnetic field to lower their barriers with respect lower aspect ratio ones. Therefore, applying a gradually decreasing magnetic field makes the bigger magnets switch before the smaller ones. In this way, placing both sized magnets in the same clock wire, two virtual phases have been created: The bigger magnets will switch when the clock has lowered enough to restore their barriers, and the smaller ones will switch when the clock field intensity has reached a very low value, after the bigger ones have already gone in a *Hold* state

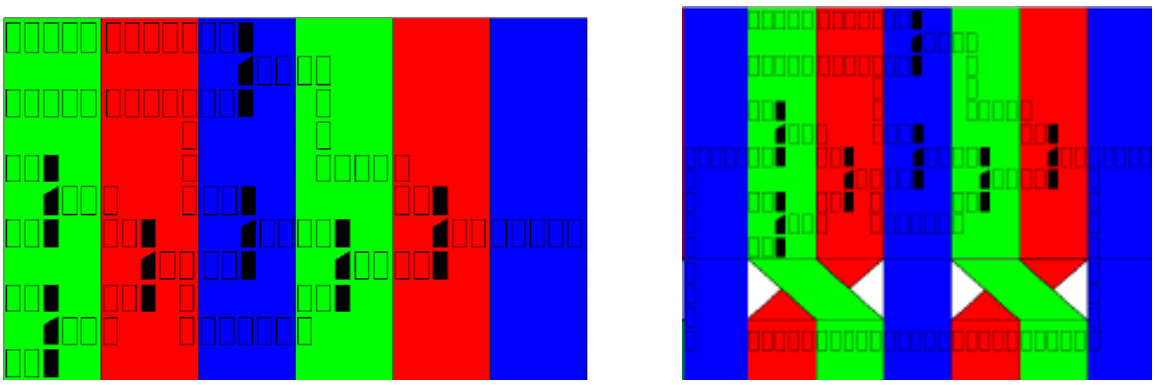

Figure 14.10: iNML Parallel Clock Wires: At left, the compact version where no feedback are possible. At right, the one using twisting of the clock wires to realize the feedbacks.

to serve them as input ones. Two clock wires in which the signal is sent phased shifted can additionally realize the 4-Phases Clock Signal. Using the Virtual Clock, building a Majority Voter is more efficient because placing this magnet on a different phase with respect the inputs will make it switch only after the latter have already arrived. Therefore, the Virtual Clock shows different advantages with respect the other clocking mechanisms:

- **Simple fabrication process** Since only two wires are necessary to realize four clock phases
- **Area Optimization** There is not wasting of area due to the twisting of the clock wires to realize the feedback, just switch the position of the bigger magnets with respect the smaller ones.
- **Feedbacks are Possible**
- **Majority Voter Efficiency**

Spin Hall Effect Clock

The magnetic field based clock in all its variants (*Snake Clock*, *Parallel Clock Wires* and *Virtual Clock*) has a big disadvantage: Power Consumption. This is due to the fact that high current is needed to flow through the wire to generate the magnetic field, and since the wires have not zero resistance, the Jule Effect is not negligible. Therefore, it would not be efficient to use a technology which is promising a low power one (since nanomagnets switching energy is very low), but implying the usage of a clock mechanism which will "erases"almost these advantages in term of power. This is the reason why alternative clock solutions have been explored to reduce the power needed to put the magnets in the *Reset* state.
One is the *Spin Hall Effect Clock*. Its layout is similar to the one of the *On-chip Magnetic Field Clock generation* (see Chapter 14.1.1), the main used material is *Tantalum*, and it also uses current flowing through it to generate the clock signal. The main advantage relies in *Tantalum* physical property of showing high *Spin Angles*, which is electrons split according to their spin. What happens is that, electrons with the same spin accumulate near the same surface of the wire, reducing the amount of current needed to generate the clock signal. An image is shown in fig.14.11.

Magneto-Elastic Clock

To further reduce the clock power consumption, the idea is to use something which is based on *Voltage* instead of *Current*, to avoid the Jule Effect loss. One possible solution is the *Magneto-Elastic Clock*. It is based on the *Magneto-Elastic Effect*, typical of Piezo-electric materials, according to which an electric-induced strain makes the magnetization change.

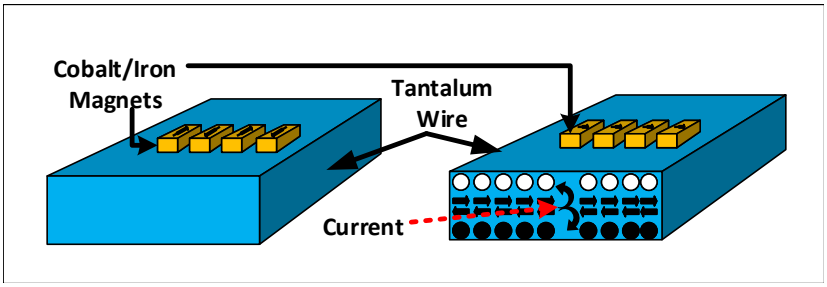

Figure 14.11: iNML Spin Hall Effect Clock.

In fig.14.12 it is depicted the layout of this clock scheme placed under nanomagnets. It is possible to notice that parallel electrodes are buried inside the *PZT* substrate. Applying a voltage across the two electrodes, an in-plane electric field is generated which will induce a physical strain to the magnets that will be forced in the *Reset* state. In fig.14.13 it is shown a typical cell placement using this clocking mechanism.

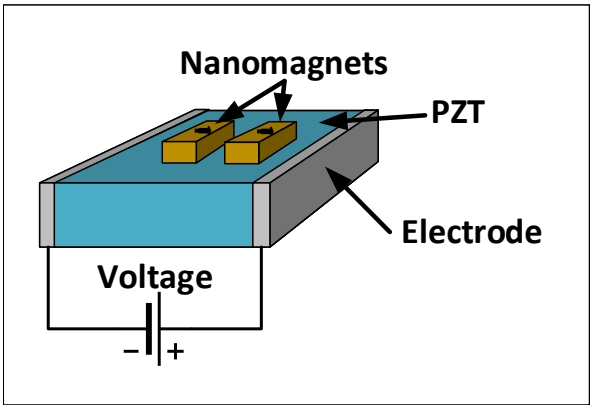

Figure 14.12: iNML Magneto-Elastic Clock.

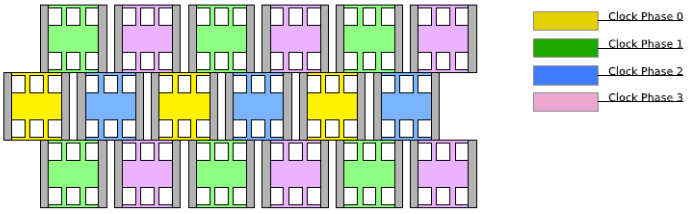

Figure 14.13: iNML Magneto-Elastic Clock: Cells Placement.

14.1.2 iNML: Some Logic Gates

Horizontal and Vertical Wires

In *Horizontal*, wires, the magnetic axis of aligned magnets is an *Anti-ferromagnetic alignment* while in *Vertical* one it is a *Ferromagnetic* one. Both wires are shown in fig.14.14.

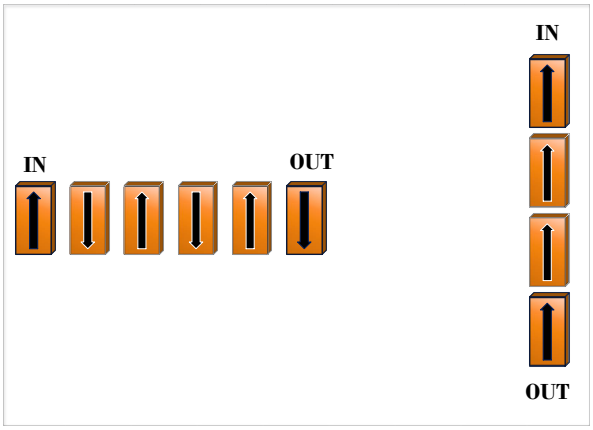

Figure 14.14: iNML wires: At left the Horizontal wire and at right the Vertical one.

Inverter

The *inverter* is just an *Horizontal wire* made up of an odd number of magnets. Since the coupling is *Anti-ferromagnetic*, the output data is the opposite of the input one. It is shown in fig.14.15.

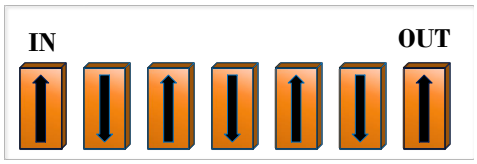

Figure 14.15: iNML inverter horizontal wire.

Cross-Wire

The *Cross-Wire* has the ability to cross 2 wires on the same plane without interferences. It is shown in fig.14.16.

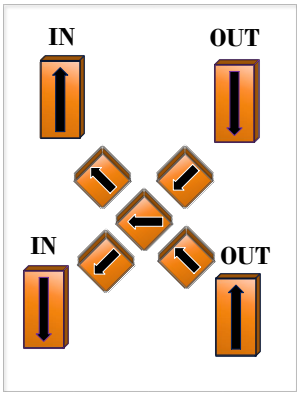

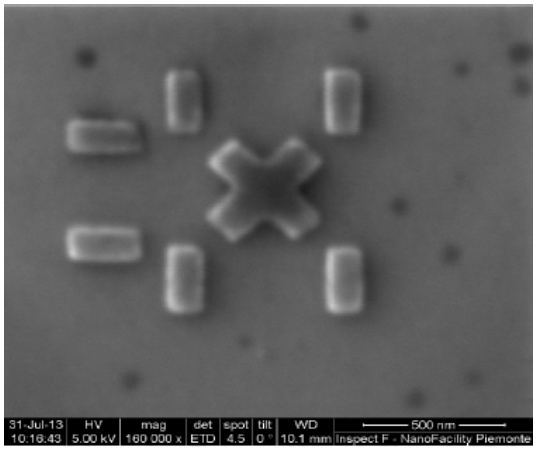

Figure 14.16: iNML Cross-Wire: At left, the model and at right, the physical implementation. The latter Image was obtained at Nano-facility Piedmont, using a SEM (Scanning Electron Microscope)

The Majority Voter

Its behavior is the same explained in **??**. Its realization in *iNML* must take into account from where inputs are coming to design correctly the output function. Indeed, Inputs coming from the top an the bottom are *Ferromagnetic* aligned and will force the majority Voter Magnet to assume their same value respectively. The other input, coming from the side, usually the left one since information propagation is left to right driven as choice, will force the majority Voter Magnet to its *Anti-ferromagnetic* state. It is shown in fig.14.17.

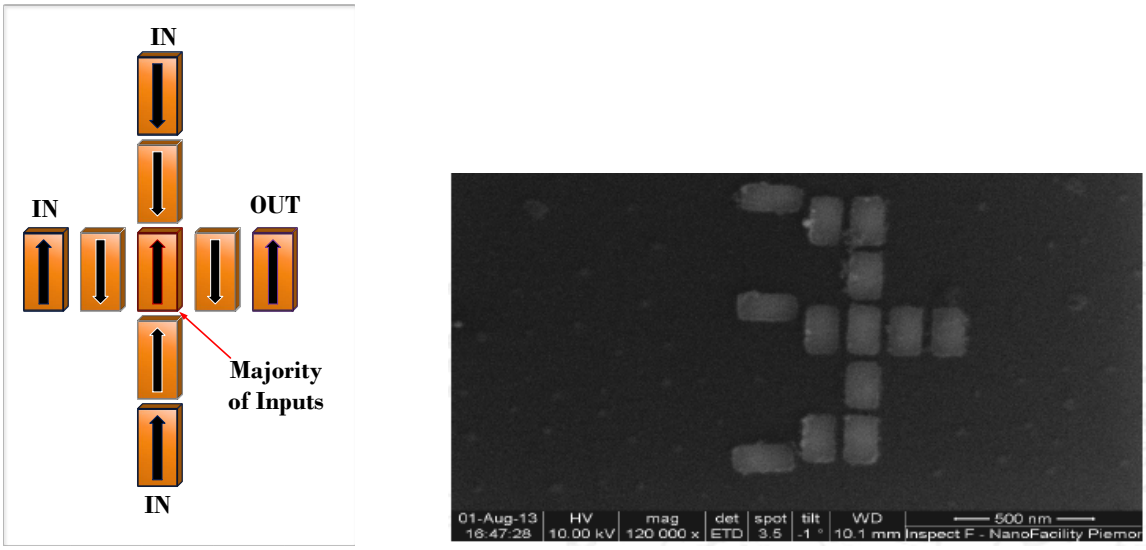

Figure 14.17: iNML Majority Voter: At left, the model and at right, the physical implementation. The latter Image was obtained at Nano-facility Piedmont, using a SEM (Scanning Electron Microscope)

Figure **??** shows the experimental results for the eight input combination of a majority voter analysed with a magnetic force microscope(MFM) at University of Notre Dame (group of Prof. Porod).

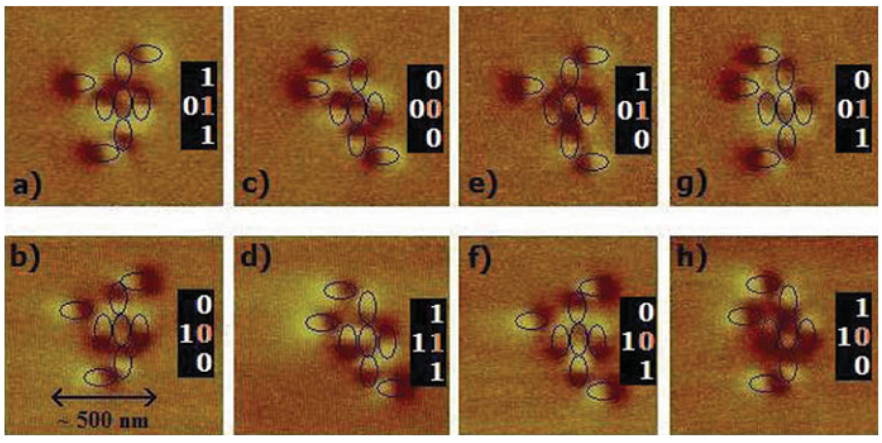

Figure 14.18: Test for the eight input combination of a majority voter analysed with a magnetic force microscope(MFM). Figure taken from [XX] developed at Notre Dame University (Prorod et al.)

The *AND* & *OR* Magnets

These two Magnetic cells are based on a *Cut* Magnet. In particular, the cut magnet will produce asymmetry in the energy barrier, making it more suitable to polarize itself as logic

'1' (**OR**), or as a logic '0' (**AND**), depending on how the cut magnet is placed with respect the input ones. Both functions are shown in fig.14.19.

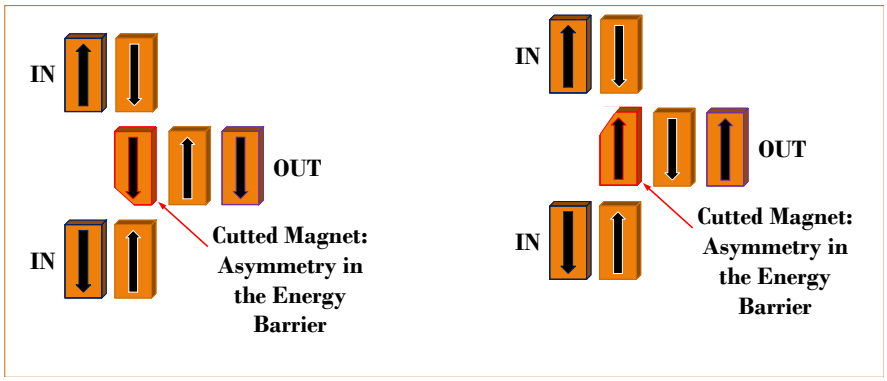

Figure 14.19: iNML *AND* & *OR* Magnets: At left the one implementing the *AND* function and at right one implementing the *OR* one.

14.1.3 iNML: Multi-Layer Design

iNML Technology can benefit from the possibility to realize designs on overlapped layers, but only using Magnetic Field based Clocking Mechanism (not Magneto Elastic). This happens because magnets placed one on top of each other, on different layers, align themselves in an anti-ferromagnetic configuration. It is important to notice that an intermediate layer is needed, the so-called *VIA* layer. Its name origins from the fact that it behaves like a *VIA* in *CMOS* Technology, a pass-through. Without it, magnets belonging to neighboring planes will be affected by this interacting magnetic field, making them behave wrongly, since not all of them need to receive inputs from other layers, but simply from neighboring magnets belonging to the same layer. The *VIA* magnets will copy the magnetization status from the source layer magnets and will interact with the destination layer ones, polarizing them correctly. Magnets in this intermediate layer are placed only where a *VIA* is needed. In this way, the remaining ones will be unaffected by the magnetic field generated by the ones placed on other active layers, since they are far enough to nullify the magnetic field interaction. Therefore, the magnets which must not interact with other layers, will continue to work as usual, receiving their inputs from their neighboring magnets, not the ones placed on top of or under them.
The Multi-layer approach can reduce the circuit area and latency. Indeed it is possible to have computation and interconnects on different layers, to reduce the routing congestion, or also having parallel computation on different layers, if the circuit exploits this advantage. For example, it is possible to evaluate two distinct data, in parallel, on two different layers, and finally compute a third one combining them on the final layer. In this Thesis, design have been realized on one, three and seven layers, counting also the *VIA* ones, to separate the active layers.
in fig.14.20 it is possible to see a model of the physical implementation of a multilayer approach, while in fig.14.21 it is shown a Full-Adder realized on three overlapped layers (2 active layers, 1 and 3, and the *VIA* one, the layer 2).

14.2 iNML and Domain Wall interconnects (Doman Magneti Logic)

NML logic leads to compact circuits with a very low power consumption. However, if this is true when considering very simple circuits, in case of complex and realistic architectures

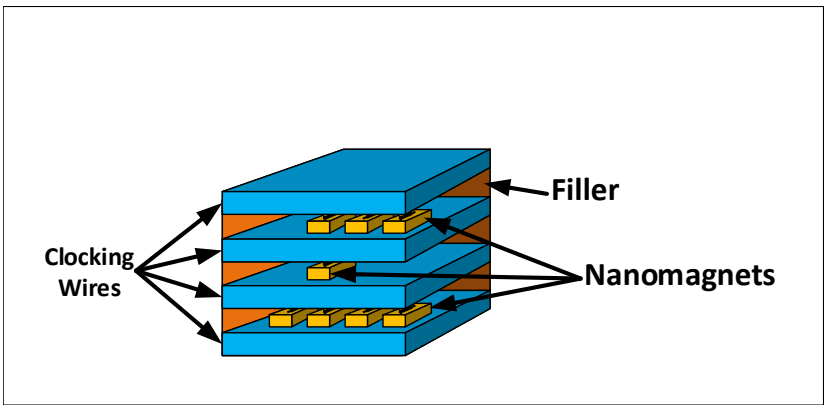

Figure 14.20: iNML Multi-Layer design: physical structure.

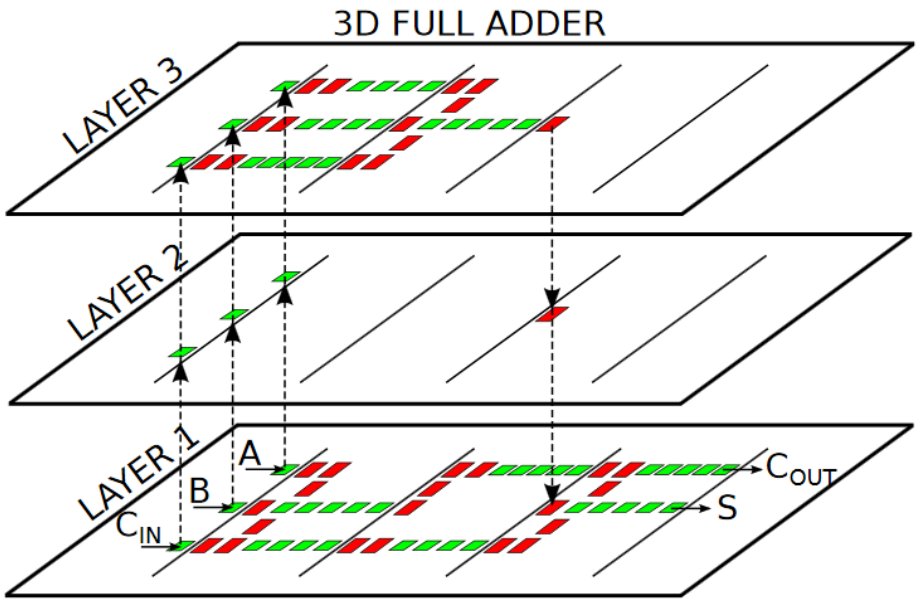

Figure 14.21: iNML Multi-Layer design of a Full-Adder: Layers *1* and *3* are used as computational ones, while layer *2* is the *VIA* plane to correctly send data through the other two ones.[149]

the situation is the opposite. In fact circuit efficiency is seriously reduced by a large amount of area wasted for interconnection wires. Magnetic interconnections can take up more than 99% of the entire circuit area. There are two main reasons to explain this behavior. First, up to now only one single layer can be used to implement NML circuits. A particular logic block, the crosswire allows to cross two wires on the same plane without interferences. But, while the crosswire allows to effectively build circuits using only one layer, interconnections efficiency is extremely low. Second, constraints related to the clock generation network fabrication limits the placement of magnets and clock zones layout. One important thing to note is that, in NML technology, more area means more latency and power dissipation. One efficient solutions for interconnection wires is to exploit Domain Walls technology. Domain walls (see previous chapter) are region of space inside a magnetic material, where two opposite magnetization come in contact. Considering a magnetic wire uniformly magnetized, a domain wall is created if an opposite magnetization is forced at one of the wire tips. The domain wall travels along the line propagating therefore the information. It appears evident that domain walls are an ideal vector for information propagation inside a magnetic circuit, while the strongest point of NML logic is the efficiency in building logic

gates. These two technologies can be mixed creating a new type of magnetic circuits, the Domain Magnet Logic (DML).

A multiphase clock system is required to correctly propagate information. Considering a three phases clock, it is necessary to generate and apply to the circuit three different clock signals. Consequently multiple clock wires are needed. In Figure 14.22.A is depicted the circuit layout considering a three clock phases. Clock zones are fabricated by parallel stripes, corresponding with the clock wires buried under the magnets. The maximum number of magnets that can be cascaded in a clock zone is around 5. This clock zones layout was chosen because it has several advantages. It allows automatic signals synchronization and it is compatible with up to date fabrication processes. The drawback is that it constraints circuit layout. In particular wires acquire a characteristic stair-like shape (Figure 14.22.A) when it is necessary to propagate signals in vertical direction. Inefficient vertical signals propagation, coupled with only one circuit layer, leads to a huge increment in circuits area for interconnections overhead.

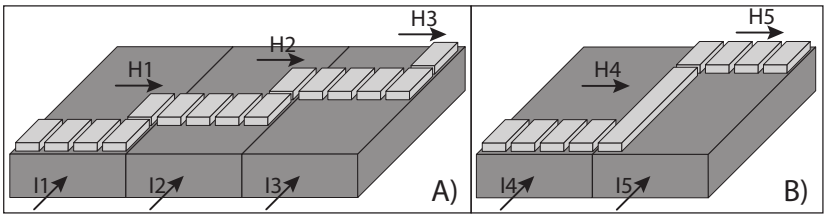

Figure 14.22: A) NML vertical interconnection. Due to the technological constraints on clock fabrication, vertical NML wires have a typical stair-like shape. B) DML vertical interconnection. Domain wall is promising for interconnections thanks to its simplicity. It is basically a magnetic wire.

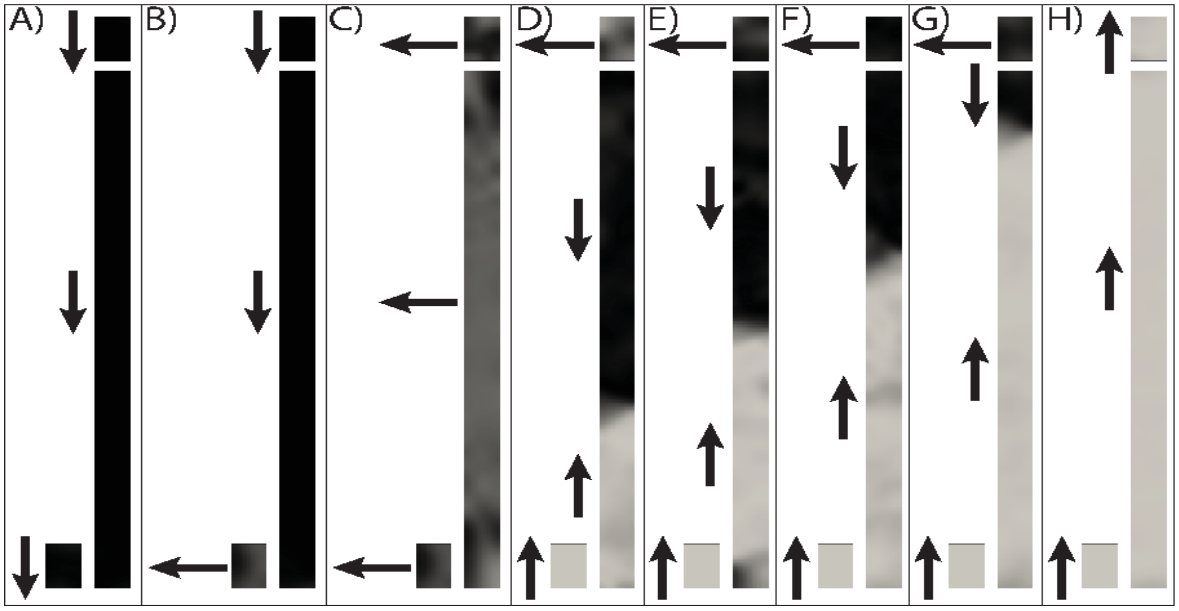

Figure 14.23: Main simulation steps of a DML structure. A) Initial state. B) The input magnet is forced in the RESET state, while the line and the output magnets are still in the initial state since they belong to a different clock zone. C) Also the line and the output magnet are forced in the RESET state. D) The input magnet is forced in a stable state and the magnetic field start to be removed from the line. The domain wall is created. From E) to G) the domain wall propagation can be observed. H) When the magnetic field is completely removed also the output magnet switches.

Domain walls share many common features with NML technology. They represent therefore a promising structures to be integrated in NML circuits. Considering a generic magnetic

material, distinctive regions with a uniform magnetization, called magnetic domains, are divided by an interface, namely a Domain Wall (Figure **??**.D). In a domain the magnetic moments of atoms assume the same versus and direction. In the region of transition between different domains a gradual orientation of the magnetic moments occurs. Domain walls technology was first proposed by Russell P. Cowburn and co-workers. They are generally constituted by a long stripe of magnetic material uniformly magnetized in one direction. A domain wall is generated forcing one of the stripe tips in the opposite state. The domain wall then starts to propagate until it reaches the far end of the line, carrying the correct information. Domain wall is a well consolidated technology with many experimental validation to sustain its theoretical validity.

While employing domain walls it is also possible to implement complex circuits based on logic gates, like NOT, AND, OR, it appears evident that they are best suited to carry information from one point to another. NML technology instead allows to efficiently build logic gates, while interconnections lead to a huge wasted area. Mixing these two technologies it is therefore the most natural way to exploit the advantages of both of them, greatly enhancing magnetic circuits development.

One basic structure is reported in Figure 14.22.B. It uses 2 nanomagnets, one as input and the other as output, and a line. The first magnet correspond to the last magnet of the previous clock zone (see Figure 14.22.B), while the line and the output magnet belong to the same clock phase. The low level simulation of the structure is depicted in Figure 14.23. Both magnets and the line are made of Permalloy, with a maximum mesh size of 5nm. Magnets are 60x90x20 nm^3, while the line is 60x1200x20 nm^3.

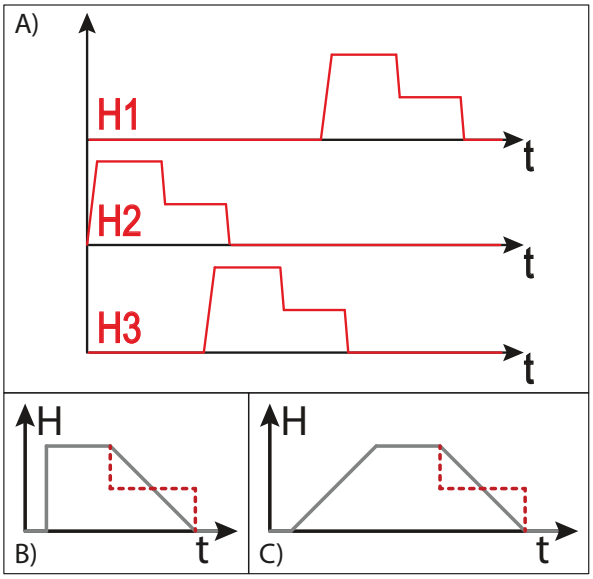

Figure 14.24: A) Clock signal waveforms in DML logic. Waveforms are similar to classic NML logic, but a two-steps magnetic field is necessary. The value required to reset the line is slightly higher then the value required to reset the magnets. B) STEP-clock. The magnetic field has a very short rise time, in the simulations an ideal step is used. C) RAMP-clock. The magnetic field is slowly applied to the circuit. The rise time can vary from 1ns to few ns.

Both magnets and the line are initialized in a stable state, with magnetization vector pointing downward (Figure 14.23.A). An external magnetic field is applied first to the input magnet, which belong to the previous clock zone (Figure 14.23.B), and then to both the line and the output magnet (Figure 14.23.C). The magnetic field is removed from the input magnet, that is then forced in a different stable state (Figure 14.23.D), with magnetization pointing upward. This behavior mimic what happens in a complex circuit. The input magnet, being part of the previous clock zone, is forced in a stable state by other magnets

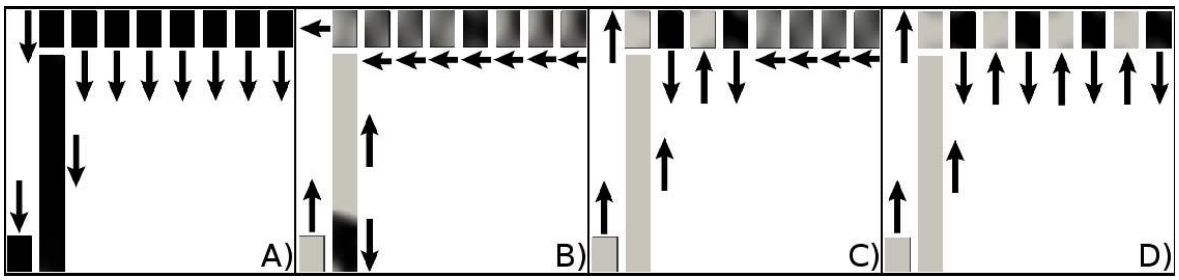

Figure 14.25: Simulation of a domain wall interconnection coupled with an horizontal NML wire. A) Initial state. B) Signal propagation through the domain wall. C) Signal propagation through the first 4 output magnets. D) Signal propagation through the last four magnets.

belonging to its clock zone. When the input element is stable, the magnetic field applied to the line and the output magnet is slowly removed (Figure 14.23.D). As can be observed from Figure 14.23.D a domain wall is created inside the line, however the output magnet is still forced in the RESET state. This is possible because the magnetic field required to force the line in the RESET state is slightly higher then the one required to reset a magnet. More details on the required magnetic field strength are presented in Section **??**. Removing the magnetic field slowly will cause immediately the creation of the domain wall inside the line, but the output magnet will stay in the RESET state since the magnetic field is still applied. The domain wall propagate successfully through the line (from Figure 14.23.D to Figure 14.23.G). When the magnetic field is completely removed also the output magnet switches to a stable state, according to the line state. The information is therefore correctly transfered through the magnetic interconnection.

The clock signal waveforms used are depicted in Figure 14.24.A. The three clock phases are similarly to the one of Figure **??**.C, but a two-steps signal is required. As stated before the value of magnetic field required to reset the line is higher than the value necessary to reset the magnets. The exact value of magnetic field depends on the line length and width. At first glance this is a disadvantage, however the benefit provided by this solution more than compensate the increment in magnetic field strength. This solution greatly reduces circuit area, consequently reducing power consumption. More details can be found in Section **??**. It must be noted that the two-steps waveform is just a simulation gimmick, used to simplify and shorten the simulation. The two-steps waveform is equivalent to a slow descending ramp, a signal with a long fall time as depicted in Figure 14.24.B and Figure 14.24.C. Regarding the rise time of the clock signal we have adopted two solutions. In the first one, STEP-clock (Figure 14.24.B), the rise time is very short (100ps) and approximated as an ideal step in the simulation. In the second one, RAMP-clock (Figure 14.24.C), the rise time is much longer, from 1ns to several ns. The RAMP-clock is a safer solution. A signal with a longer rise and fall time is easier to generate at experimental level. The STEP-clock instead, requires a very short rise time. While signals with such a short rise time can be generated, they are more sensitive to noise and variations from the ideal condition, which can negatively affect the behavior of the domain wall. We have studied and analyzed in details also the STEP-clock solution, because it allows to use a lower magnetic field. Applying a clock signal with a very short rise time induces an oscillation of the magnetization vector that lead to the creation of the domain wall also with a lower magnetic field than the RAMP-clock solution.

Figure 14.25 shows the simulation of a more complex circuit, a domain wall interconnections and 8 magnets chained at its output. The structure span through 3 clock zones. The first magnet is in the first clock zone. The line and the first 4 magnets are in the second clock zone. The 4 last output magnets are in the third clock zone. For space reasons only the more important simulation steps are reported. In Figure 14.25.A the initial state is depicted, the magnetization of all magnets points downward. In Figure 14.25.B the magnetic field

was applied to all elements and removed only from the input magnet and the line. The input element is forced upward and the domain wall is created inside the line. After the complete removal of the magnetic field from the first clock zone also the first 4 output magnets switch correctly (Figure 14.25.C). After the removal of the magnetic field also from the second clock zone, the last four magnets switch properly (Figure 14.25.D). Figure 14.25 clearly highlights how the solution here proposed is perfectly embedded in the NML logic structure.

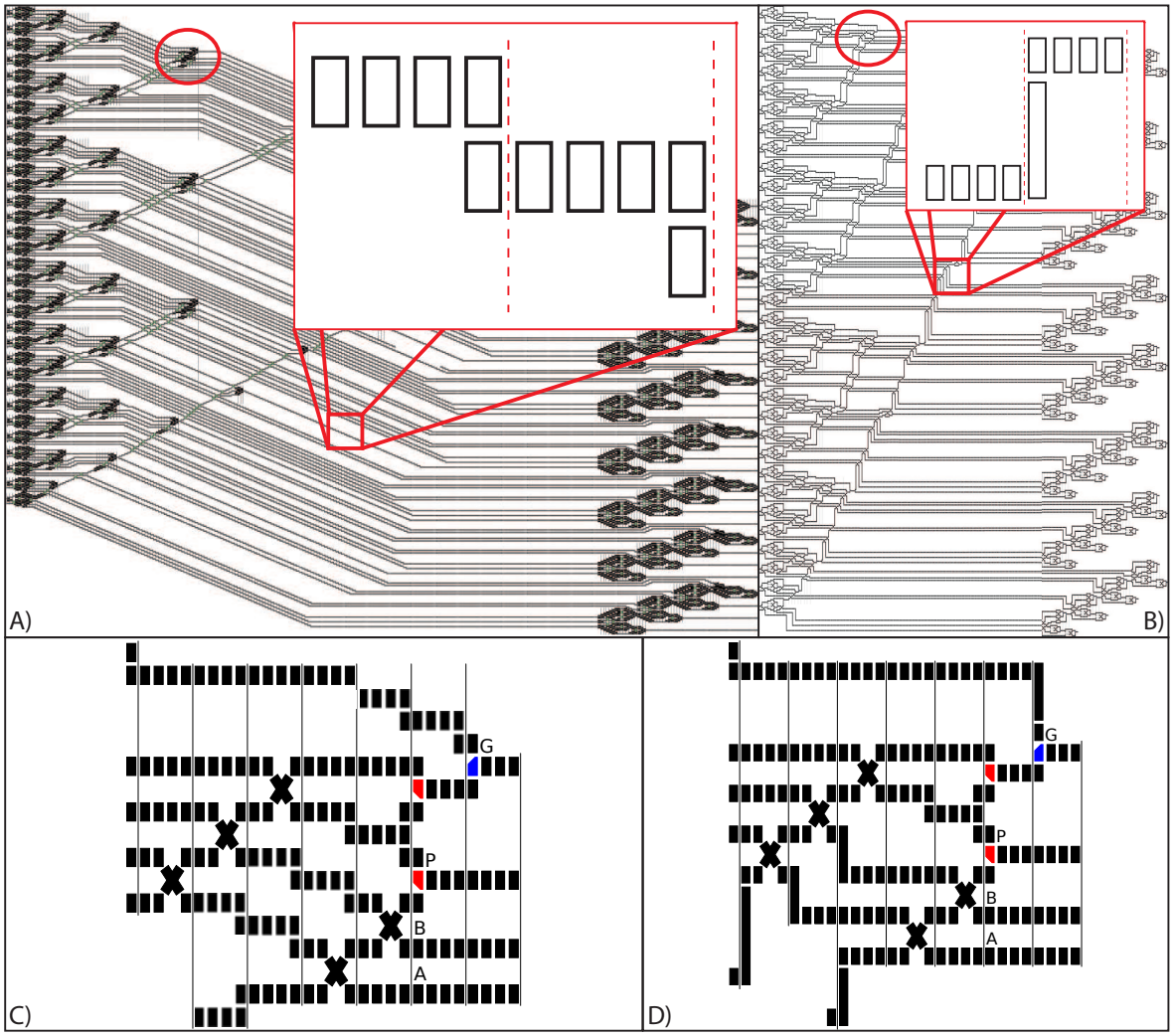

Figure 14.26: Pentium 4 like 32 bits adder. The structure is based on a Sparse Tree as carry generation network and 8 four bits ripple carry adders. A) Pure NML implementation, vertical signals propagation follow a stair-like structure. B) DML implementation, domain walls are used for vertical signals propagation. The area gain is around 58%. The circuit area in the circle, in which the generate and propagate signals are produced in the carry generation network, is zoomed out in C) for NML and D) for DML logic respectively.

An example of a complex circuit based on this technology is now commented. The circuit is an adder similar to the one implemented in the Pentium 4. A complete architectural analysis in total occupied area and timing varying the number of bits from 4 to 32 with a step equal to 4 bits is the case studied. The implementation of such an highly parallel architecture is very inefficient in pure NML circuits. In Figure (Figure 14.26.A) is depicted the pure NML 32 bit implementation. The adder uses a Sparse Tree Network for carry calculation (depicted on the left of Figure 14.26.A). In the Figure 14.26.C is reported a section of the generate and propagate network in more detail, with the propagation of

vertical signals similar to a stair-like structure. Eight 4 bits ripple carry adders are used to evaluate the sum (depicted on the right of Figure 14.26.A). Long interconnection wires are used to connect the two parts of the adder. Interconnections follow the stair-like structure described in Section **??** and highlighted in the detail of Figure 14.26.A. This circuit is one of the most complex NML circuits ever presented in literature, and clearly highlights the huge area overhead due to interconnection wires. In Figure 14.26.B is depicted the adder implemented using domain walls for vertical interconnection wires, as reported in Figure 14.26.D in more detail. The area reduction can be clearly understood at glance.

The complete architectural analysis in terms of total occupied area and latency is summarized in Figure 14.27, where the behavior of area varying the number of bits grows with same trend for both technologies. However the evolution of the DML implementation has the tendency to saturate. This behavior can be attributed to the fact that increasing the complexity of the circuits the logic blocks are more relevant than the interconnections in terms of occupied area. This is not valid for NML implementation, in which the interconnections have an important role producing a wide area overhead as highlighted in Figure 14.26. It is important to note that lower area means lower latency.

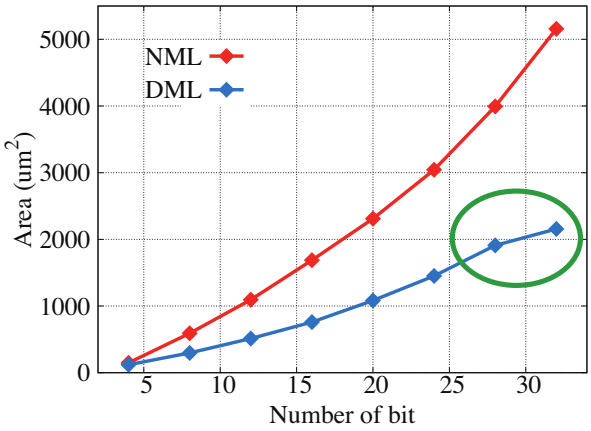

Figure 14.27: Trend of area, expressed in μm^2, of NML and DML implementations of a Pentium 4 Adder varying the number of bits. In DML technology the area points to saturate, as highlighted in the picture.

CHAPTER 15

Out of Plane NML and DW racetrack memories

15.1 Out Of Plane Nano Magnet pNML

In iNML there are some problems that need a new version of Nano Magnet Logic, we had seen the problem of the information transmission in witch only few dots can be cascaded to have a correct information passage from one dot to the next one; this implies the division in clock zone for the circuit and a use of a multiphase clock mechanism as seen in chapter 3.3.2. The multiphase system is used not only to achieve correct transmission, but also to have unidirectionality of information flow but, comes at the cost of a complicated clock mechanism and high dissipation in power for clock generation, moreover the divisions in clock zones not allow a fully pipelined architecture. Another negative aspect, is that with iNML is not possible to go directly in the vertical direction, this can be done with a step strategy that leads to a drastic increment of the overall area and of power also. To overcome this problems a new version of NML is studied which name is pNML or pNML where 'p' stand for perpendicular, that is the way of the preferred magnetization, that means the direction in witch the sample will need less energy to be in that state.
In pNML there is no need of multiphase clock system, there is only one oscillating clock applied to all the circuit, this result in a great simplification of the generation of the clock and a reduction in power dissipation. The unidirectionality of information instead, is implemented thanks to irradiated zone that are preferred places where the nucleation of magnetization starts. There is also a great reduction in area and power since is possible to go directly in the vertical direction and can lead to fully pipelined architecture. Due to this reasons we chose to focus on pNML as the most promising candidate for nano magnetic logic technology.

The Out of Plane pNML are based on dots of nanomagnets that exhibits perpendicular magnet anisotropy PMA, this characteristic is achieved making a stack of Co and Pt and repeating that according to the parameters needed for the dots. PMA is possible in such a structure because, if a very thin layer of Co, less than 1.2nm, is placed between Pt, exhibit high PMA due to the defects in the interface and the new alloy formation [150]. In figure 15.1 we can see an example of a Co/Pt stack put on a substrate, the number of layer is only an example, in real cases can be more:

This technology have to respect some requirement, otherwise it can't be successfully used to perform logic computation.
The fabrication of the dots must allow narrow separation between them, this is important

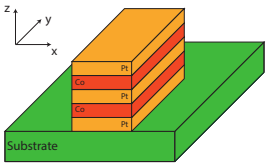

Figure 15.1: ONML dot is stack of layer of Co sandwiched between layers of Pt, this increases the anisotropy

not only to make the final circuit more compact since, narrower separation means low area for the same number of dots, but more important, is that if is possible to define with precision the separation, this means define with precision the coupling of the dots. The dots separation can be done bye a FIB irradiation and will be explained in the Fabrication section.

Another fundamental aspect is the possibility to encode a binary information, without this, is clear that the technology can't be used. This is achieved by encoding the information with the magnetic spin thanks to the anisotropy along Z-axis.
Dots must have a low switching field to design low power circuit, but this have to be not too low otherwise the dots will change according to thermal fluctuations, that is a catastrophic behaviour for the correctness of the information processment.
The important aspect of information unidirectionality flow, is achieved bye the presence of nucleation centres. This are weak spots for the dots where the coercivity is low with respect to the other regions. This spots are obtained with a FIB irradiation since is possible to change the properties of Co/Pt films with an local injections of ions of He^+, Ar^+, Ga^+ [151] and in our case the Ga^+ irradiation is the most important. In the figure 15.2 can be shown a pNML with a nucleation centre(a case, right dot), its indicate in yellow at the border while the left has no nucleation so if put one next to other(b case), the dot with the nucleation will change its magnetization because, it will feel more the coupling of the left dot, so the information will propagate from left to right.
The irradiated region is fundamental because:

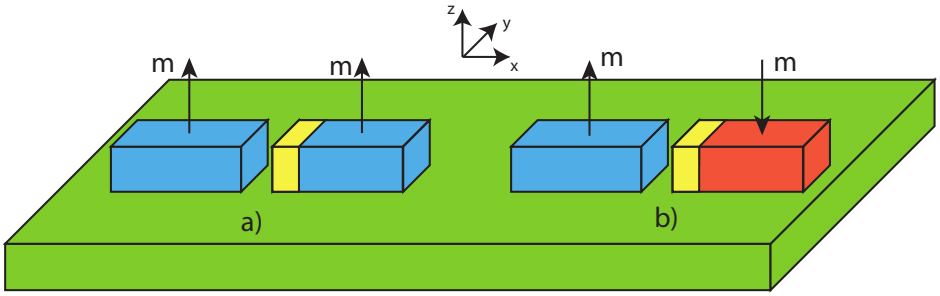

Figure 15.2: pNML dots, the yellow part is the irradiated part. a) the two dots have the same magnetization +1. b) after a certain period of time, the right dot will change from +1 to -1

- allow unidirectional propagation of the information
- dots switch with a lower field
- possibility to create different structure due to the more freedom design

All the coupling principle between dots and the information propagation will be explained more in detail in the oMNL analysis section.

15.1.1 Fabrication

To make pNML circuit, the first think to do is to have a film of Co/Pt stack where to define the needed pattern; Si substrate is needed to have a base where to place the stack of Co/Pt. The film deposition is done with sputtering first a layer of Pt over the substrate that is generally kept at room temperature, then a layer of Co and so on ending with a layer of Pt, because as said before in this thesis, Co exhibit high anisotropy along Z axis only when put between Pt layers. After the creation of the Co/Pt stack film, we need to created the dots for the needed layout; this operation can be done with the traditional techniques used in the creation of CMOS circuit, so can be used lift-off, chemical etching, focused ion beam(FIB).

The FIB irradiation technique is preferred since can 'separate' the dots from the magnetic point of view, without actually removing material; this happens because the magnetic property of the Co/Pt films can be changed by implantation of Ga^+ ions[151][152].
A very high dose of $Ga^+(> 10^{15})$ ions over cm^2 with an energy for the ions of 50 keV, eliminate the anisotropy along the Z-axis, this zone is than considered a non magnetic material, so it's like to remove the non needed part and to have desired pattern.
The FIB irradiation is used than to have the partial irradiated zone, the 'weak region' that have a lower coercivity and are a preferred point for the change of the magnetization. Figure 15.3 resumes the step explained here.

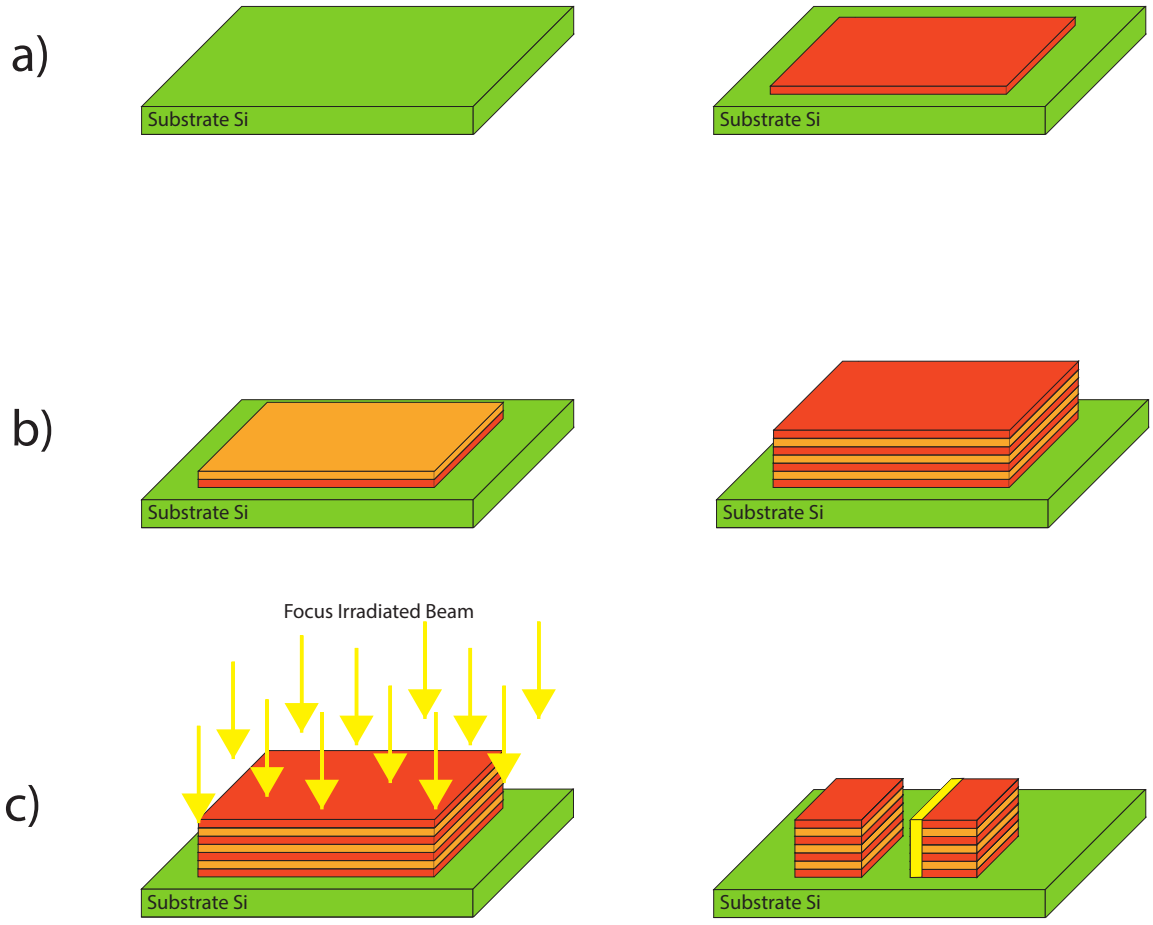

Figure 15.3: Steps of pNML fabrication. a1) the substrate is created. a2) the bottom layer of Pt is placed on the substrate. b1) first layer of Co placed. b2) the stack is made and finish with a Pt layer. c1) after the FIB use, the desired pattern and the irradiate region is made.

In this work the nanomagnet will have this structure, $Pt_{5nm}n\times[Co_{0.3nm}+Pt_{0.8nm}]Pt_{4.5nm}$[153]; in this stack structure the first Pt layers with a thickness of 5nm and 4.5 nm are needed as seed and stopper layer; n is of course the number of Co/Pt layer, this value is very important because there is a direct relation between thickness of the stack and its domain behaviour. A very accurate study on this aspect of pNML structure is done here[154] and they research can be resumed here in figure 15.4.

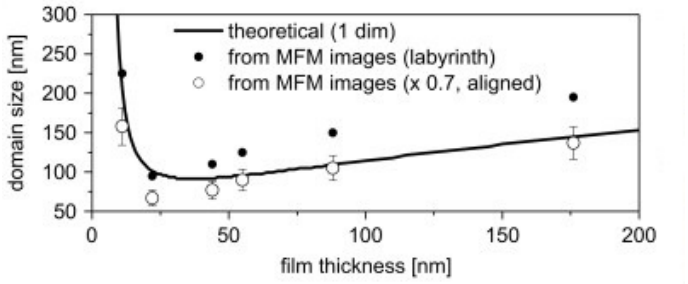

Figure 15.4: Relation between the domain size at different thickness of the Co/pt film. Figure taken from [154]

The figure 15.4 shows that the single domain size, reach a maximum of 300nm for a film thickness less than 10 nm; with the increasing of thickness the domain size reach a minimum around 30 nm of thickness, than after this start to rise very slow. After this considerations we look for structures that have a single domain more large possible; for these reasons we choose $n = 8$ so a thickness around 10nm.

15.1.2 Parameters of pNML

To simulate the Co/Pt structure we need a series of micromagnetic parameters, that model the desired structure and are needed by OOMMF to make static or dynamic simulation. This parameter are related to the energies terms explained in the previous section, and in specific are exchange stiffness A_{exch}, magnetic anisotropy K and saturation of magnetization M_s. There is a detailed study here[155] about the relation of this parameters with specific characteristic of the material, for our work we need to know only how to have a value of this parameters and to use them in simulations.

- **Ms**: the magnetic saturation depends from the ratio the thickness of Co and the total thickness of the stack structure, we define with t_{Co} and t_{Co+Pt} these terms that are related as follow

$$M_s = M_{Co} \times \frac{t_{Co}}{t_{Co+Pt}} \tag{15.1}$$

  In the equation 4.1, the term M_{Co} is estimated equal to 1.4×10^6A/m[155]. According to this value Ms will have a value around 4×10^5A/m but according to measured value of Technic University of Munich[156] the value of Ms will be around 7×10^5A/m due to the polarization of the Pt layers with Co layers.
- A_{exch}: the exchange stiffness is important because, according to it's value the magnetic dot will have different hysteresis curve; figure 15.5 will show this relation.
- K: the magnetic anisotropy K is the most important because determine the reversal behaviour of the nanomagnet. The equation for K is:

$$K = K_v + \frac{2K_s}{t_{Co}} - \frac{\mu_0}{2}M_s^2 \tag{15.2}$$

  in the relation the terms K_v and K_s are volume and magnetic anisotropy. The iNML and pNML differs from one to other because the sign of K, so if we want a pNML will

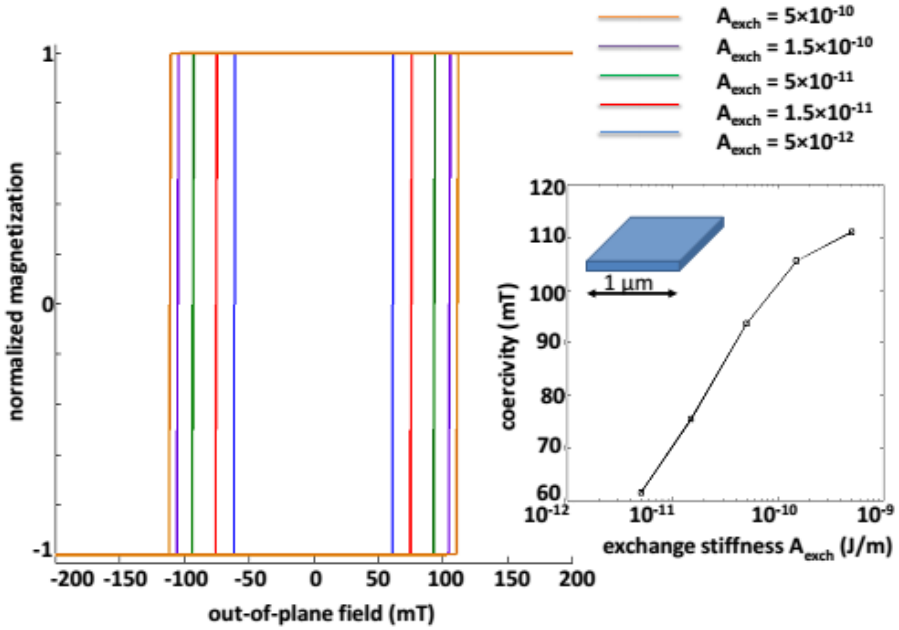

Figure 15.5: Hysteresis curves for different values of A_{exch}. Figure taken from [156]

have a positive value of K, negative otherwise. K is important also because there is a directional proportionality with the coercivity of the nanomagnet dot, so its ability to withstand an external magnetic field without being demagnetized, higher value of K means high coercivity. Figure 4.6 shows this.

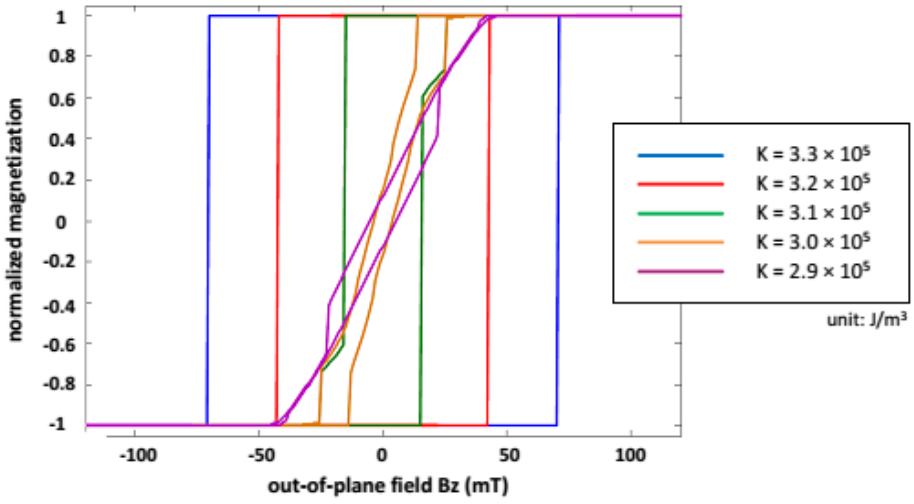

Figure 15.6: Hysteresis curves for different values of K. Figure taken from [156]

The parameters except for the anisotropy, are assumed constant in all the structure for simulations but, in the production of pNML the transition zone between the dots have a linear change for the parameters and isn't abrupt.

15.1.3 pNML analysis

The pNML nanomagnets, switch by a nucleation event and after this a domain wall propagation change the magnetization state for all the Co/Pt dot structure. The nucleation site

have a position dependent on the FIB irradiation because low anisotropy regions, the irradiated ones, are the place with lower coercivity so the easier places to changes magnetizations state.

To have more clear this principle, we will see the simulations with OOMMF of TUM group[153]. In this simulation are compared three dots 200nm × 200nm made with a stack of five layers of Co/Pt ($Pt_{5nm}5 \times [Co_{0.3nm} + Pt_{0.8nm}]Pt_{4.5nm}$) and consequently $A_{exch} = 1.5 \times 10^{-11}$ J/m, $M_s = 7.0^5$ A/m and $K = 3.2 \times 10^5$ J/m^3[153], this micromagnetic parameters are assumed constant for all the structure, except for the anisotropy K that can change in irradiated zones. The simulations are also done without considering temperature effects and we can examinate three cases:

- Dot 200nm×200nm without irradiated zones
- Dot 200nm×200nm with irradiated zones at border
- Dot 200nm×200nm with left side irradiated zone

Dot 200nm×200nm without irradiated zones At the begin of the simulation, the dot have a upwards magnetization(blue colour in figure 15.7); when the simulation starts, a uniform field is applied for all the structure pointing opposite with the polarization of the magnet. With time passing, the magnetizations state of the dot will change, starting from the centre of the structure, a domain wall is created and this will reverse at the end the magnetizations state of the dot, reaching a downwards magnetization(red colour in figure) when simulation finish; this can be seen in figure 15.7.b).

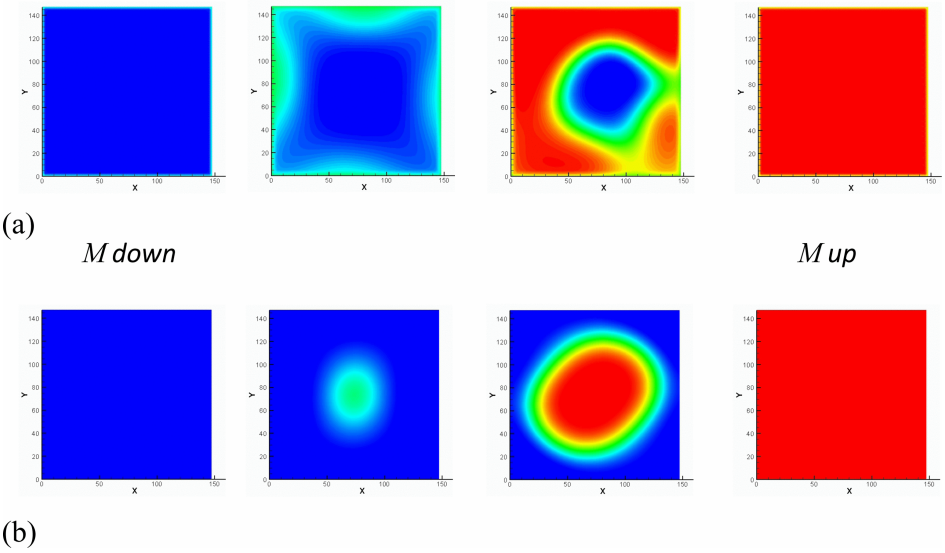

Figure 15.7: Magnetization switching for a 200nm× 200nm. a) The pNML dot is irradiated around the edge. b) the dot is not irradiated Figure taken from [153]

Dot 200nm×200nm with irradiated zones at border In this simulation the border of the dot have a low anisotropy region due to FIB irradiation, with a value of K ranging from 0 to $K_{max} = 3.2 \times 10^5$ J/m^3 and the irradiated zones are 30 nm wide, while A_{exch} and M_s are constant in all the dot. As we can see in the figure 4.7 a), the dot at the begin of the simulation, like the previous case, have a downwards magnetization, but in this case, after the application of the field the change in the magnetization starts from different point and in the specific from the borders, because of the low anisotropy regions; when simulation ends, the dot will reverse its magnetization. In figure 15.7.a) there are some snapshot of this simulation.

Dot 200nm×200nm with left side irradiated zone This case is the more interesting because is the one used in the logic design with pNML. The dot is irradiated only on the left edge with a width of the low anisotropy zone of 30 nm and $K < 2.3 \times 10^5$ J/m^3 while, for the non irradiated zone $K_{max} = 3.2 \times 10^5$ J/m^3 ; A_{exch} and M_s have the values as for the previous cases in all the structure. We can see in figure 15.8 that the dot have an initial upwards magnetization, after the application of an opposite magnetic field, the domain wall creation start in the left edge because there is the irradiated zone and complete the magnetization switching. The importance of one side irradiated zone is not only that its allow unidirection of propagation, but allow also the switching with a lower field because how we will see later in this thesis, the irradiated zone increase the coupling field.

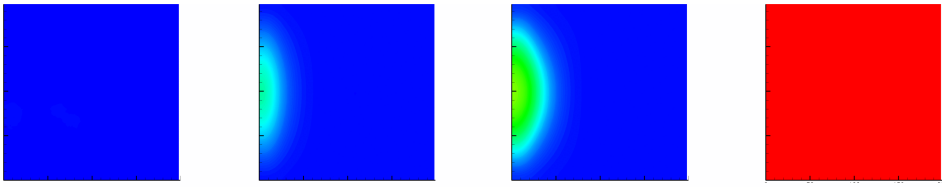

Figure 15.8: Switching of magnetization for a partial irradiate dot. Figure taken from [153]

15.1.4 Coupling for irradiated pNML dot

To study the effect of the partial irradiate zone on the coupling a good way can be to use a fixed dot(can't change it's magnetization state) and a partial irradiated dot free to change it's magnetization state, the irradiation is on the left edge of the free dot. Two cases can be now under analysis:

- free dot on the right of fixed dot
- free dot on the right of right of fixed dot

In both cases, the field of the fixed dot is added to the external field felt by the free dot, and depending on how the dot are magnetized, the coupling field will help the switch in case of parallel magnetization, otherwise will hire the switching of the irradiated dot.

The first case can be seen in the following figure. In figure 15.9 we can see that, due to the presence of the fixed dot, the free dot experience a coupling that shift its hysteresis curve by $2B_{copling}$ so the coupling between the dots can be interpreted as the half of the hysteresis shifting.

The second case can be seen on figure 15.10

In this situation the coupling of the fixed dot, when to the right of the free dot, is lower than the coupling felt by the free dot when the fixed dot is to its left. This is due to the partial irradiated region that makes a greater coupling, a relation can be derived because the left coupling is greater than the right coupling, this means that the irradiated dot have an asymmetric coupling:

$$B^{left}_{coupling} > B^{right}_{coupling} \tag{15.3}$$

Approximately we have a coupling 10 times greater for the first situation with respect to the second one[153].

15.1.5 Nucleation Fields and ANC: an enhanced approach

To nucleate the DW there is the need of the presence of both an ANC and a nucleation field, which aim is to create the new magnetization domain. A lot of investigations has been done around this arguments, since the field required to nucleate the magnetic structure depends

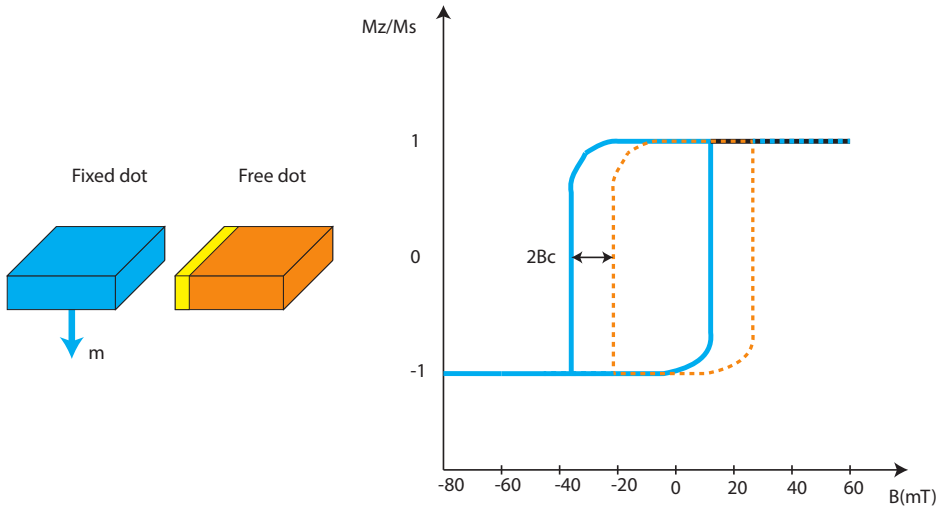

Figure 15.9: Switching of a dot with a irradiated zone, the free dot is one the right. The hysteresis curve is normalized to have $\mid M \mid = 1$

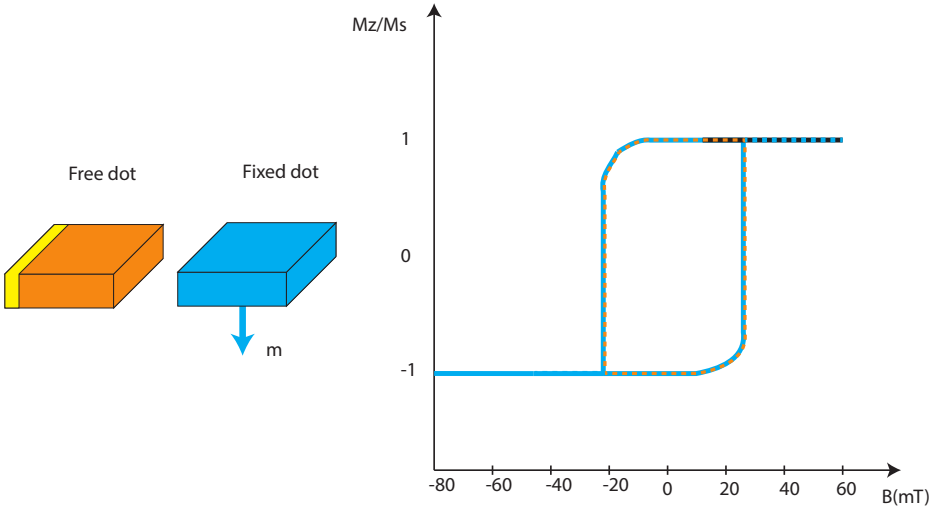

Figure 15.10: Switching of a dot with a irradiated zone; the free dot is on the left. The hysteresis curve is normalized to have $\mid M \mid = 1$

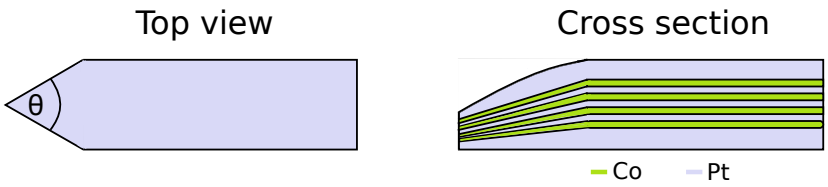

Figure 15.11: Wire geometry. In the top view the tip angle can be seen, while in the cross section how during fabrication due to shadowing effect less material is deposited at the triangular-pointed wire end with tip-opening angle θ.

on the anisotropy and on the energy barrier of the nucleation centre. The aim is to reduce the amplitude of the applied field required to nucleate the DW. In particular the change of the geometry of the domain wall, could reduce the nucleation field till about 60% [157]. All this observed results are meaningful for the investigation of the domain wall structures. In fact is very important for that structures to have a weak pinning site in order to improve the switched velocity.

To reduce the local anisotropy, the domain walls are design with a tip-shaped end, and the nucleation field can be intentionally varied by changing the angle of the tip as is depicted in Fig. 15.11. If the structure of the wire is analysed the ratio of the Co/Pt thickness in the multilayer stack is almost constant so it is unaffected by the reduction of the film thickness towards the triangular-pointed wire end. As a consequence the magnetization M_s remains constant. What changes is the magnetocrystalline anisotropy constant ($K_1 = K_{1,eff} + \mu_0 M_s^2/2$) which depends mainly on the interface and boundaries contributions. In particular there is a reduction of this constant towards the tip ended, which means that the same reduction can be investigated any time there is a deposition of less material. This reduction is caused by two main reasons: the gradual reduction of the thickness of the Co layer, and the reduction of the thickness of Pt interlayer. The reduction of the material that reaches the substrate in the tip of the wire, with respect to the quantity of the material in rest of the wire is caused by the so called shadowing effect during the fabrication.

The decreasing of the required nucleation field is assumed to be originated from a decrease of the local anisotropy constant ($K_{1,eff}$) in the tip area due to shadowing during sputter deposition of the multilayer. Both in experimental and in theoretical results demonstrate that the local anisotropy constant change linearly with respect to the change of the angle, in particular it decreases linearly in the tip area from the maximum value K_1 to $K_1' = aK_1$. However, the linearly behaviour is demonstrated only for angles that are less than 90° .

Other shapes are investigated and this investigation has revealed that the nucleation depends on the total area with reduced anisotropy constant. In triangular end wires the switching field, since it depends on the area, is influenced by the opening angle: the smaller is the angle the larger is the tip area which is available for the nucleation.

The fabrication process of this new wires it is based on the bottom-up micro fabrication approach, with a single lithography step.

There is one main drawback. The shadowing effect does not cause only a modulation of the multilayer stack at the end of a wire due to triangular-pointed ends, but also at the edges of a wire, the multilayer does not end abruptly but the thickness gradually decreases on the way to the edge. An alternative approach is to create first the multilayer wire and then by the use of the lithography to shape correctly the wire. However, this method not only increases the number of steps required to realize the structure but also can improve the number of defects, by increasing the problem of edge damage. It has been demonstrate that the damages of the edges can be change completely the behaviour of the perpendicular magnetized nanostructures.

15.1.6 Clocking

In NML, as in CMOS, there is the need to have a clock system to provide timing for the circuit. The Co/Pt structure can be clocked and re-evaluated with a clock signal that, for this technology, is an oscillating field(square waveform or sinusoidal), that is perpendicular to the pNML circuit. Thanks to the clock, the meta stable states, in a pNML circuit(simple case a pNML wire) can be driven out; meta stable states MS means structure that are parallel aligned, so one them have to switch to reach the computation ground state.
There are two types of metastable states that differs for the direction of the magnetization of the parallel aligned structures are illustrated in fig 4.11 and are :

- upward MS (fig 4.11 a)
- downwards MS (fig 4.11 b)

The upwards MS can be driven out if a downwards field is applied, this will switch the right dot because in case of MS the dot that is on the right is switched, this is due to the partial irradiated zone that allow a greater coupling from the left dot on the right one. For the downward Ms the principle is the same but of course its needed a upwards field.

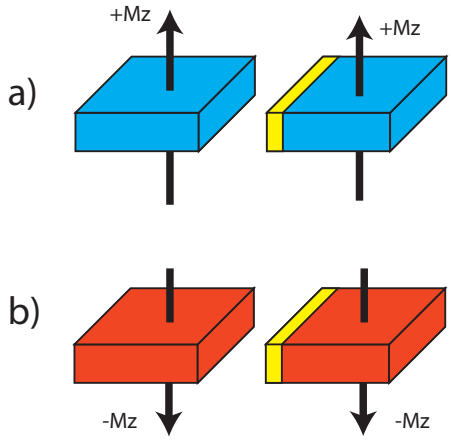

Figure 15.12: Metastable states for two dots. a) upwards metastable state. b) downwards metastable state

The value of the clocking field is one of the most important parameters to make a whole pNML circuit to work correctly. The value have to be sufficient to help the switching of the dots in a metastable state, but not so strong that independently from the magnetization of the coupling, the dot 'follows' the field, so if field is up, all the structures are up, if field is down, all the structures are down. A general rule can be followed:

$$\mid B_c \mid - \mid B^{left}_{copling} \mid + \mid B^{right}_{copling} \mid < B_{osc} < \mid B_c \mid + \mid B^{left}_{copling} \mid - \mid B^{right}_{copling} \mid \tag{15.4}$$

where B_c is the switching field of the alone dot, without near neighbour dots. The maximum distance within the field of one dot can be felt by other dots, is around 150 nm for dot 200nm×200nm [153]. Over this value the coupling is negligible. In figure 15.13 there is the representation of a nano wire with an initial fixed dot and a chain of free irradiated dot. This figure shows how, thanks to clock field, the metastability is driven out. The first dot is a fixed dot with upwards magnetization, the information is moved trough the wire ever $\frac{1}{2}T_{clock}$ and will arrive inverted if the wire have an odd number of dots, not inverted if the wire have a even number.
The first metastability is up/up so have to wait negative edge of the clock to remove the metastability. The MS is now between the A dot and B dot(down/down MS) and a positive edge is needed to remove the metastability in this case and so on for next dots. A N-dot wire need a $\frac{N}{2}$ clock cycles to order the chain in antiferromagnetic ground state. The partial irradiation zone gives unidirectionality to the structure preventing back-propagation, so the information move from left to right, and multiple bits can be send every 1 Clk and a pipeline is created, because the pNML is inherent pipelined.

The uniform magnetic clock field can be generated with system of coils, one of that is the Helmholtz coil system. This structure is maid with two circular coil with same number of turns connected in series (figure 15.14).
The magnetic flux density **B** is:

$$B = \frac{\mu_0 \times NI}{r} \tag{15.5}$$

Where r is the distance between coils, N the number of coil turns and I is the current. More complex system are possible, a good research is done here[158].

15.1.7 Cross wire

The possibility to have wire crossing is mandatory for a technology because allow more complex circuit design and higher integration of device in the same area. The idea to have

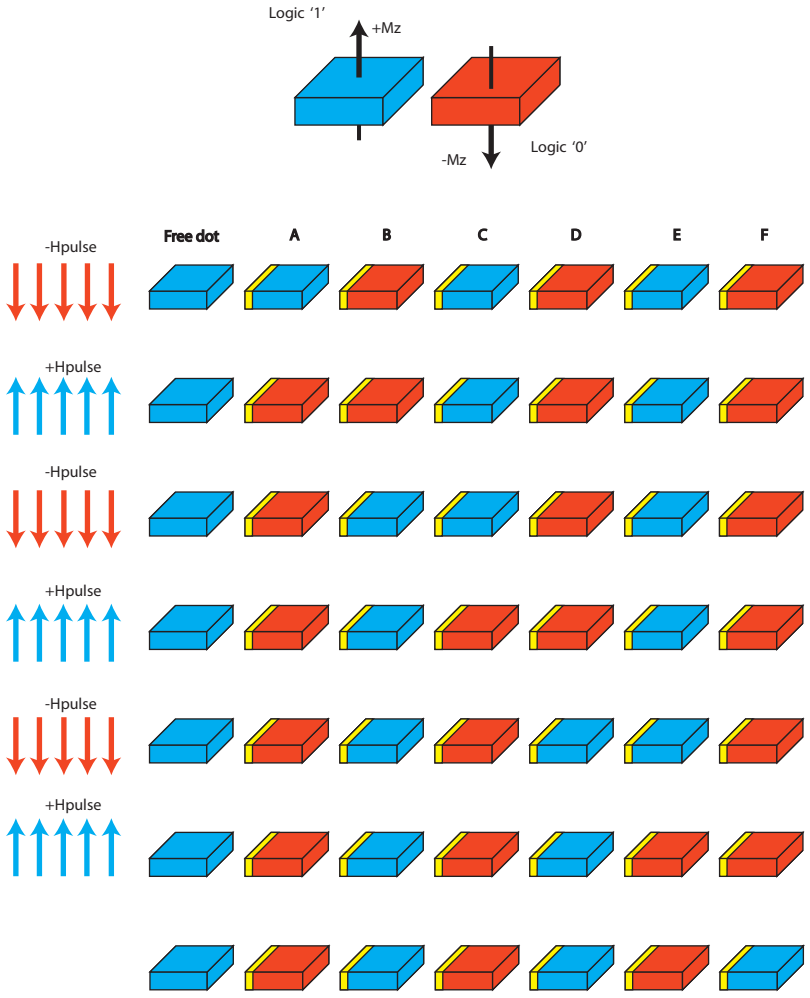

Figure 15.13: Representation of the movement of information in anti-ferromagnet ordered line

signal crossing in pNML bring to a 3D arrangement of magnet[159].

The 3D solution is needed because, if we cross two signal in one plane, this will result in a error off information transmission since, as in figure 15.15 b), the coupling field of input I1 and input I2, act in opposite on the central magnet labelled O so is not correct to use this structure.

The solution is to use instead a second layer, made on hydrogen silsesquioxane HSQ (no magnetic material reduces the coupling) where to route the crossing signal figure 15.15 c); the coupling of M1 is transferred to M2 by the so called UP-VIA that is the irradiated zone of M2 in position up to M1, while from M2 to M3 there is a DOWN VIA, so the irradiated zone is on M3 under the M2 dot. An important aspect is that when the signal from one level is transferred to another level, the coupling field of one level to the other, have to be small enough to not give birth to a nucleation event and domain wall propagation that make incorrect results in signal transmission.

In figure 15.16 we can see how the magnetic field acts from one dot to the other and where are the irradiated areas. Is clear that also for crossing wires, we need an external clocking field, to help the stray field of dot2 to change the state of dot1; depending on the state of dot2 the switching field of dot1 have different value, so for a anti parallel alignment we

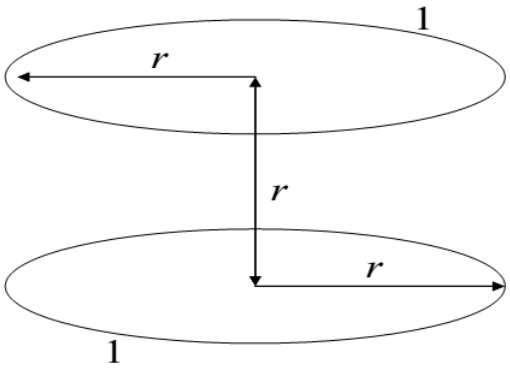

Figure 15.14: Helmholtz coil system

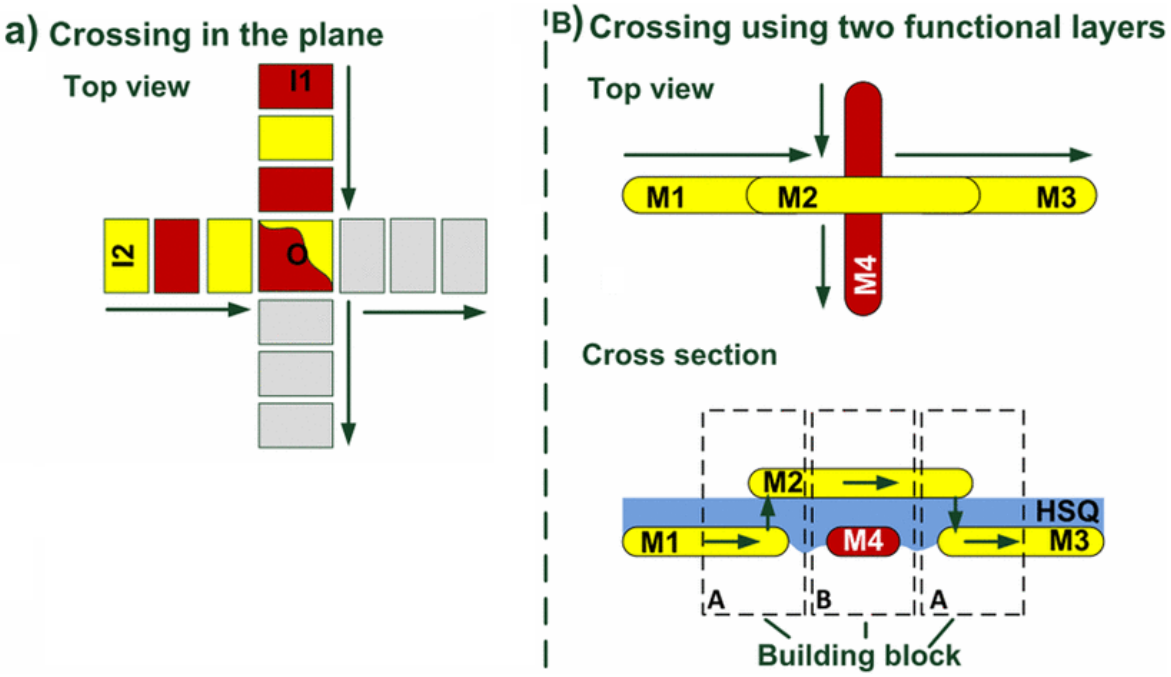

Figure 15.15: Signal crossing. a) error state in the central magnet O due to the different propagation in the information direction. b) Crossing signal using two functional layers. Figure taken from[159]

need a higher value of external field, a bound can be found:

$$H_{external} = H_{nucleation} - H_{coupling} \tag{15.6}$$

Where $H_{external}$ is the value of external applied field, $H_{nucleation}$ is the field that makes possible the nucleation and the domain wall propagation, while $H_{coupling}$ is the coupling of one magnet to the other, that helps the switch when the dot are parallel, or hinder if the dot are anti-parallel. Fig 4.15 b show the variation in hysteresis curves for the parallel and anti-parallel.

Following this concepts, can be realized also a cross wire structure with wires placed in more than two level, this allow to have a lower parasitic coupling on the region where there is the cross. A structure like this can be viewed in figure 15.17.

As depicted in figure 15.17 there are three layers of wire that gives the benefit to transmit information in two different direction avoiding errors.

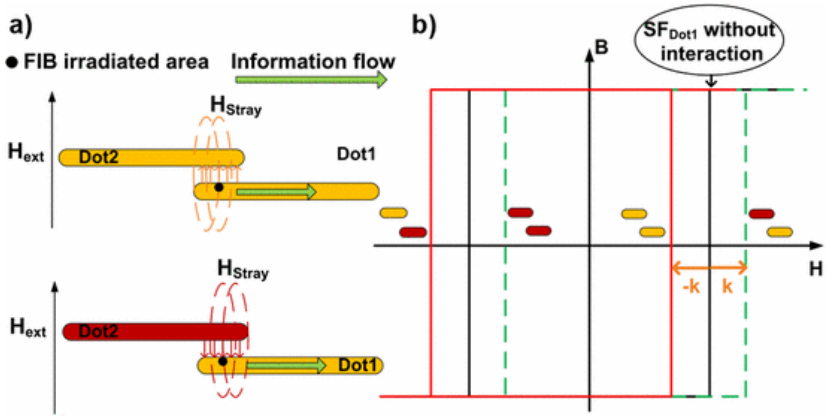

Figure 15.16: Field interaction in two different layers. a) parallel and anti-parallel magnetization for the dots on different layers. b) hysteresis curves for the two cases, can be seen the difference in the switching field SF. Figure taken from[159]

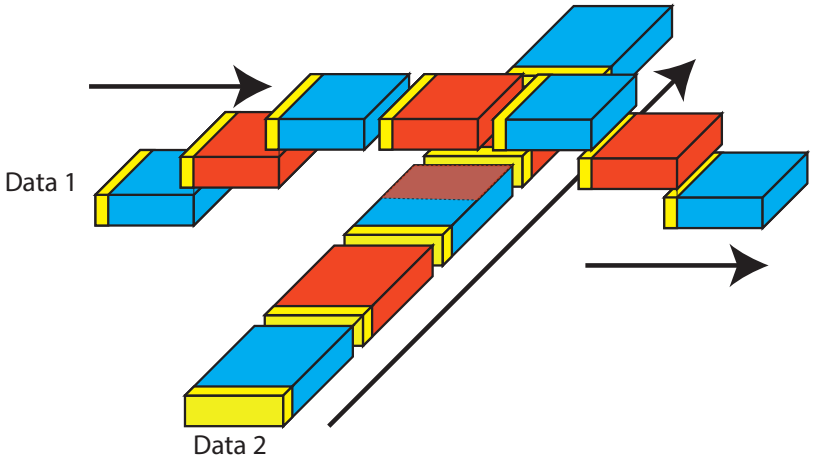

Figure 15.17: Cross wire with three level of layers. The data 1 and data 2 can be transmitted without errors; the three level structure have lower parasitic coupling in the highlighted, cross area.

15.1.8 Speed and Power

The speed of pNML circuit an the power dissipation are fundamental aspects to compare this technology with the CMOS based and to underline the strong or weak point of this pNML technology.

From the study of this parameters done here[160], the time needed to makes a single pNML dot to switch is from 4 to 5 ns as illustrated in figure 15.18. This time can be made smaller increasing the switching field value, but a greater field reduces the stability and the fault tolerance and increase of course the power dissipation.

From th analysis made[160] can be estimated that the power dissipation for a 200nm×200nm dot is 2.91 aJ while for an elongated magnet is 5.21 aJ for every switch, since the static power is 0. This allow to make estimations on dissipated power, so in figure 15.20 there is a comparative on the pattern match processing element depicted in figure 15.19 realized in pNML and in CMOS at different length process; the results are expresses in the Energy/Delay graph of figure 15.20.

NML can't compete with CMOS technology today, but dissipate $\frac{1}{100}$ in power with respect to CMOS at iso-performance; furthermore this is an over estimation for the dissipated power because, the switching will not occur if inputs don't change.

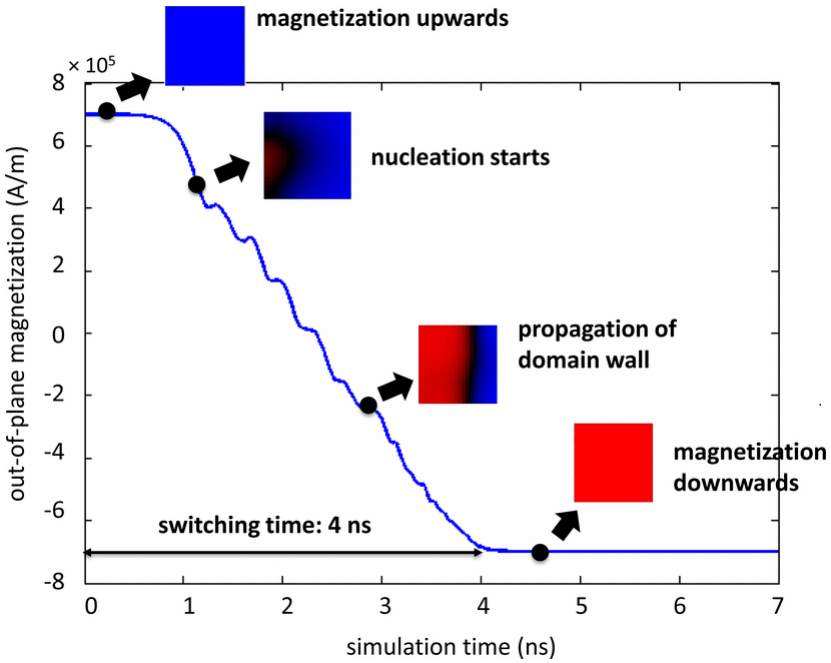

Figure 15.18: Switching time for a single pNML dot. Figure taken from[160]

In the power analysis also the generation of the clock field have to be considered; from the analysis made, using microcoils, the power dissipated is 10x larger than the losses in the circuit and this lead to a power reduction with respect to CMOS in 10x; however the analysis are made on a very small circuit test[160], so if we consider a bigger, more complex circuit, the overhead of the clock generation, will be reduced, and can be reduced more again if we use a multilayer architecture, so there will be only a clock generation for circuits at different levels.

15.2 Simulation of pNML structures

Simulations are very important in research because, allow to study the behaviour of some hypothesis and ideas giving, in case of positive result, the will to continue in the direction thought or to try new possibilities in case of wrong results.
In the magnetic field of research, the more valid simulators are NMAG[161] by the University of Southampton and OOMMF[162] by Applied and Computational Mathematics Division (ACMD) of ITL/NIST.
The simulator used in this master thesis is OOMMF. In the next section will be simulated and analysed different structures made in pNML technology so magnet made of Co/Pt layers.

15.2.1 2 Dot (inverter)

The 2 dot structure is the basic circuit whence to start simulations of pNML because, makes clear the coupling principles of one dot to another, how nucleation starts and how the propagation of the domain wall changes the magnetization state.

In this simulation two square dot 200 nm x 200 nm are simulated; the spacing between the dots is 20nm and they are made with a stack of 8 layers of Co/Pt ($Pt_{5nm}8 \times [Co_{0.3nm} + Pt_{0.8nm}]Pt_{4.5nm}$) and since the two Pt layers are the top and the bottom layers, the relevant thickness for the simulation is $8 \times [Co_{0.3nm} + Pt_{0.8nm} = 8.8nm$ that is approximated

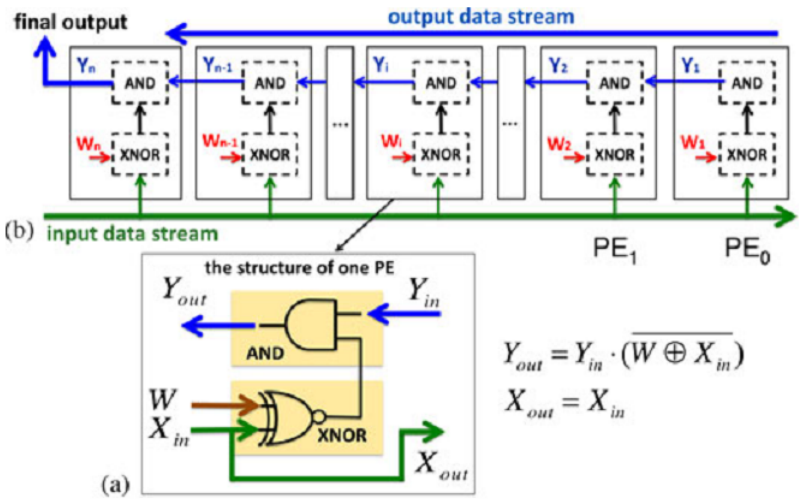

Figure 15.19: Pattern match processing elements where information flows between processing elements from left to right. Figure taken from[160]

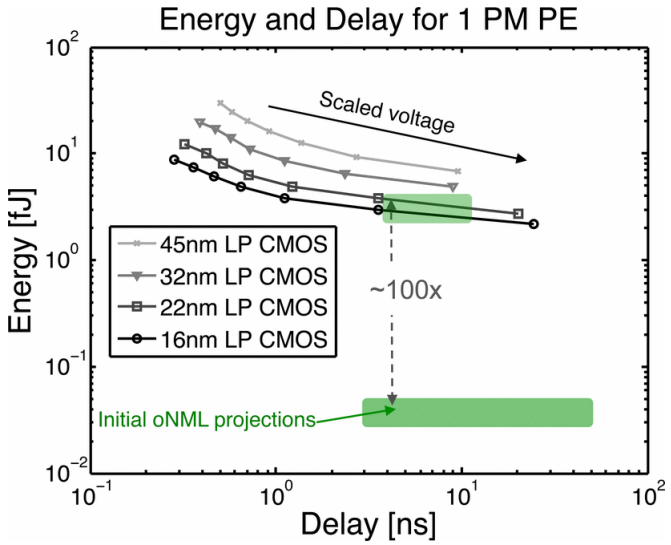

Figure 15.20: Energy/Delay of a functionally equivalent CMOS test circuit. Figure taken from[160]

with 10nm in the next simulations. The irradiated zone is made with FIB and is 20 nm wide.

In figure 15.21 a) are depicted the 3D view and the top view of two pNML dots with the relevant geometric dimension; the yellow colour indicate the irradiated zone of the dots so where the nucleation starts due to the lower coercivity with respect to the non irradiates zone. In the next simulations OOMMF indicate with the blue colour an upward magnetization and with the red the downward magnetization, referred of course to the z-axis, since is the primary characteristic of pNML. The figure 15.21 b) shows the elongated version of the dot, this dot has the same micromagnetic parameters as the standard square dot, is useful in the design of complex circuit made with pNML. This will be seen more accurately in the chapter 6.

To have very accurate results, we implement a 3D simulations using OOMMF eXtensible Solver Interactive Interface (Oxsii)[162].

The description of the structure we want to study is made writing the Micromagnetic Input Format (MIF) files; here we wrote all the description of the physical system so, geometric

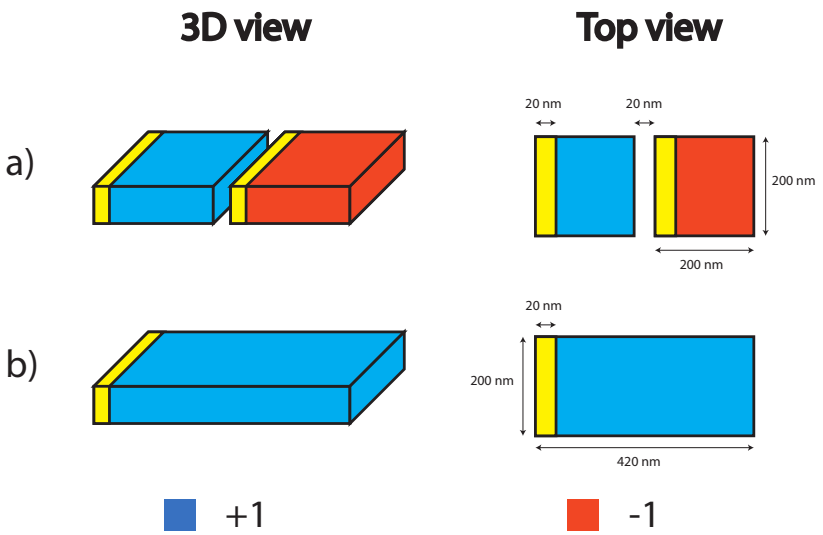

Figure 15.21: Two dot structure pNML. a) 3D view and top view for two pNML square dots. b) 3D view and top view for an elongated pNML dot. Blue colour means upward while red means downward magnetization. The irradiate zone is indicate in yellow.

Geometric parameters	**2 Dot structure**
Width	200 nm
Height	200 nm
Thickness	10 nm
Irradiated zone dimensions	20nm x 200 nm
Spacing between dots	20 nm

Table 15.1: Geometric parameters for the 2 dot simulation

dimensions, micromagnetic parameters, initial condition of the system, accuracy of the simulation, how the external clock is applied to the two dots, and also if we want a static or dynamic simulation; for the static simulation OOMMF uses a Runge-Kutta method while to find the dynamic state states, solves Landau-Lifshitz-Equation. The description in the MIF file starts defining the geometric parameters shown in tab 5.1.

The geometric dimensions are not enough, of course, to have a complete definition from the micromagnetic view point, so we had to define also the micromagnetic parameters such as exchange stiffness A_{exch}, magnetization of saturation M_s and anisotropy K.

The micromagnetic parameters used for this simulation are related to the geometric dimension of the dots and to the dose Ga^+ of the irradiated zone. The value of micromagnetic parameters are

- Exchange stiffness $\mathbf{A_{exch}} = 1.5 \times 10^{-10} J/m$
- Anisotropy $\mathbf{K} = 2.4 \times 10^5 J/m^3$ for irradiates zones, $K = 5.2 \times 10^5 J/m^3$ for non irradiated zone
- Saturation of magnetization $\mathbf{M_s} = 7.2 \times 10^5 A/m$
- Damping $\alpha = 0.055$

The value of the mesh, used for the simulation is 5 nm; the mesh is the smallest sample analysed by the simulator, bigger is the mesh less accurate are the simulations result, the mesh dimensions generally are in the order of nano meters, so i suggest to not use mesh bigger then 10 nm.

Now we have a complete definition of the 2 dot structure in terms of geometric dimensions and micromagnetic parameter but, there is also the need of a magnetic field clock as explained in the previous chapters. The applied clock is a square clock with a duty cycle of 0.5 and oscillating between 315 mT and -315mT along Z-axis and a component of 30 mT along Y-axis is also applied. The magnetic field along Y-axis is used to make the change of the magnetic state faster because, the field along Y-axis increase the magnetic torque moment on the spins of the structures; while the period is 14ns. The magnetic field clock characteristics are here exposed again for a rapid consulting:

- **Clock waveform** : square
- **Duty cycl**e: 0.5
- $|$ **Amp** $-$ **Z** $|$: 315 mT
- **Amp-Y**: 30 mT
- **Period T**: 14 ns
- **Application zone**: all the structure

At this point the last step to do is to set the initial condition of the system, so the magnetization state of the two dots. We choose a configuration as fig 5.2.

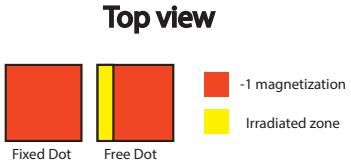

Figure 15.22: Schematic top view of the two simulated dot; the fixed dot, doesn't switch; the red part means downward magnetization, the yellow is the irradiated zone.

In the figure the first dot is a 'fixed dot' so doesn't change its magnetization state because, we impose on it a fixed field with a value equal to M_s, that is very much bigger than clock field amplitude; the fixed dot is also without irradiated zone, it is the input of the simulation; instead, the second dot is free to change its magnetization state because he feels only the coupling of the fixed dot,have the left side irradiated,and the magnetic field.

At this point the simulation can starts and due to the initial configuration of the dot (-1, -1) it is convenient to start the clock with the positive edge, that is the edge needed to change the state of the free dot.
In figure 15.23 and 15.24 there are screen-shots of the simulation obtained by OOMMF.
At the beginning of the simulation the dots have both a downwards magnetization(fig 5.3 a) that is the initial configuration imposed to the simulator trough the MIF file; in the figure is depicted also the direction of the applied clock magnetic field for each screen-shot.

The two dots are in a metastable state, one of the two have to switch to reach the antiferromagnetic order, this is possible thanks to the combination of dots coupling and clock field so, in figure 5.3 b) we can see the born of a nucleation site on the left side of the free dot, where there is the irradiated zone; with passing of time, the nucleation centre become a domain wall (fig 5.3 c) that propagate to the entire free dot switching to the upward magnetization (fig 5.3 d-e).

Once completed the switch of the free dot, the structure is in the ground antiferromagnetic order. When the positive edge of the clock ends, to the structure will be applied the negative edge; if this part of the clock have a high value, the second dot may 'follow' the clock field, changing its state to a downward magnetization. The simulation shows that with the imposed value of the clock field, the free dot doesn't change state(fig 5.3 f), it feels only a

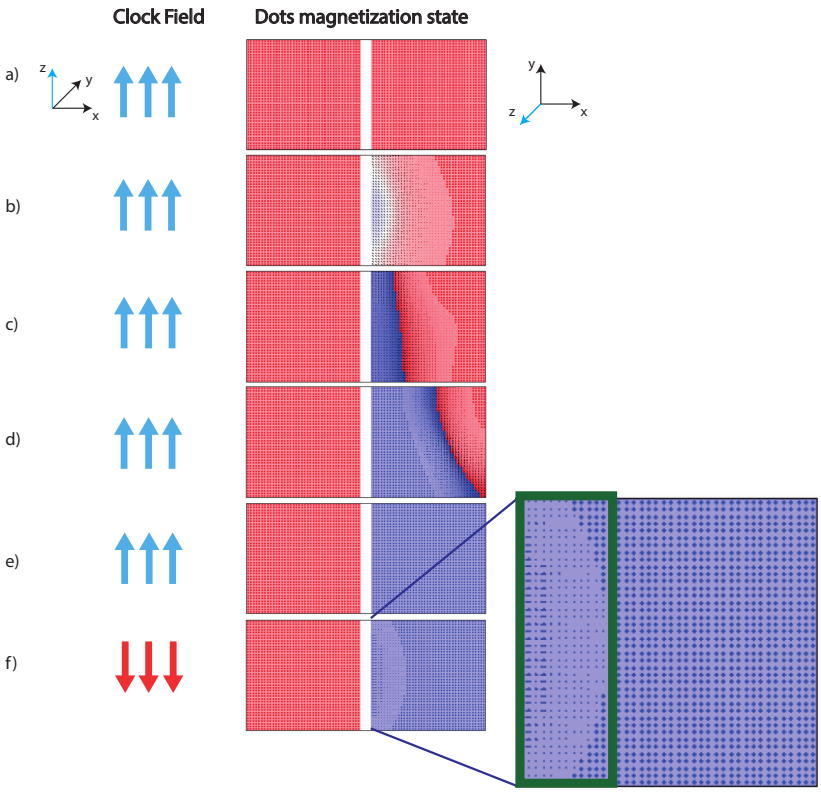

Figure 15.23: Simulation screen-shots for the 2 dot structure. Fixed dot left, free right. a) initial configuration, dots are downwards magnetized. b) nucleation event in the left side of right dot. c) domain wall start to propagate. d) propagation continue. e) right dot totally switched. f) the negative edge of the clock can't change the state of the ordered dots.

little the negative edge of the clock, in the irradiated zone that is the the weak spot of the free dot but, doesn't change the state for all the negative edge.

To have a complete simulation study, also the simulation for the transmission of 1 is done. All the parameter are the same like the previous case, but here, the needed clock edge is the negative to help the switching of the irradiated dot. In figure 5.4 there are screen-shot of this simulation.

The simulations confirms the theory behind the 2 dot structures, and also the correctness of used parameters. In the different simulation made, was observed that there isn't only one working configuration for the parameters of the magnetic field. We can lower the value and increase the period of the clock, or vice versa have a higher field with a shorter period T. It depends on what we want, speed or less power dissipation.

15.2.2 Majority voter

The majority voter is the natural gate for NML technology since it can be turned to a NAND or a NOR gate by simply fixing one of the inputs to 0(NAND gate) or to a 1 (OR gate) and it have a configuration of magneta as depicted in figure 15.25.

The tab 15.2 is the true table for the majority voter, we can note that the output is 1 if at least two input are 0, otherwise is 0 if at least two input are 1; moreover if we consider In1 = 0 than the true table coincide with the true table of the NAND, while is the true table of the OR gate if In=1.

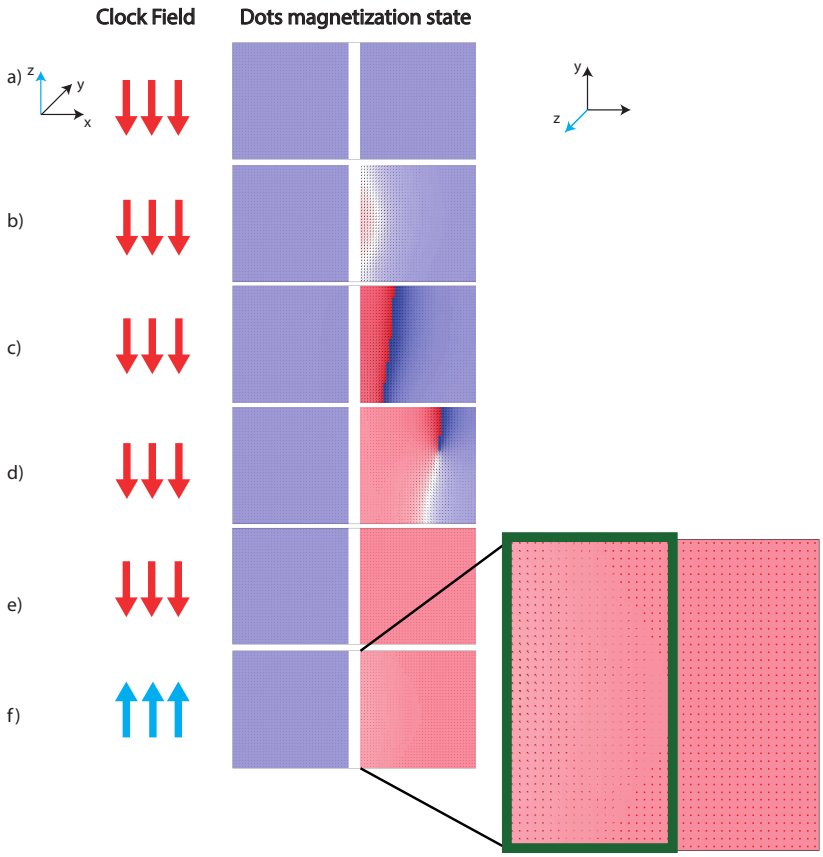

Figure 15.24: Simulation screen-shots for the 2 dot structure (inverter). Fixed dot left, free right. a) initial configuration, dots are downwards magnetized. b) nucleation event in the left side of right dot. c) domain wall start to propagate. d) propagation continue. e) right dot totally switched. f) the negative edge of the clock can't change the state of the ordered dots.

In figure 15.25 can be seen the 3D view and the top view for the majority voter. This configuration is made with four nano magnets dots, three square dot that act as inputs, and one elongated dot, that calculate the vote of them. The inputs are square dot 200 nm x 200 nm with a thickness of 10 nm and the distance from the inputs to the central dot is 20 nm; the elongated dot is 420 nm x 200 nm with a thickness of 10 nm. All the structure is made with a stack of 8 layers of Co/Pt ($Pt_{5nm}8 \times [Co_{0.3nm} + Pt_{0.8nm}]Pt_{4.5nm}$) and the irradiated zone, made with focused ion beam(FIB) is 20 nm width and is indicated with the yellow colour on three side for the majority voter so it can be sensible to the coupling field of the three surrounding inputs.

The irradiated zone for the square dots is no needed in the simulation of the only majority voter structure, but if the MV is used in a more complex architecture, then the irradiated zone is mandatory because we had to transmit the information from previous dots.

To have an accurate simulation, we implement a 3D simulations using OOMMF eXtensible Solver Interactive Interface (Oxsii)[162]. Like the simulation for the two dot structure, the description for the majority voter simulation have to be writing the MIF file, where we direct the simulator with the geometric dimension of the structure, thee micromagnetic parameters, the initial condition of the system, the clock characteristic and the method used to solve the Landau-Lifshitz-Equation.

The geometric dimensions for the majority voter is the first characteristic to write in the

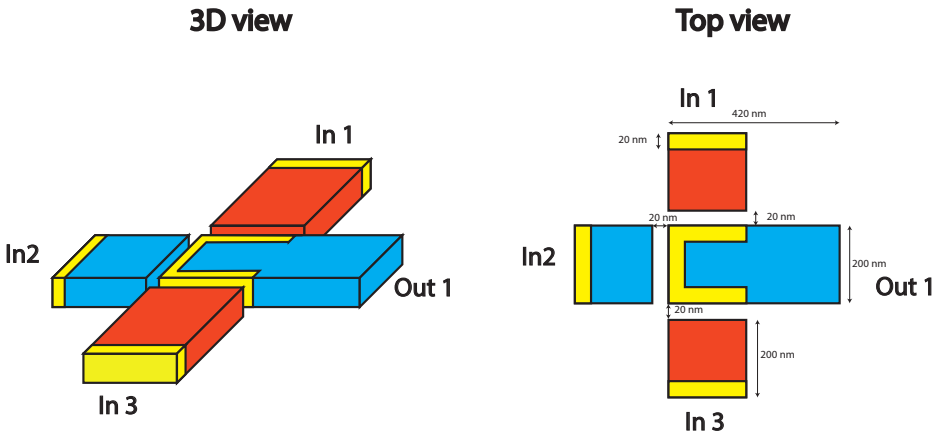

Figure 15.25: Majority voter 3D view and top view. Blue colour means upward while red means downward magnetization. The irradiate zone is indicate in yellow

In1	In2	In2	Out
0	0	0	1
0	0	1	1
0	1	0	1
0	1	1	0
1	0	0	1
1	0	1	0
1	1	0	0
1	1	1	0

Table 15.2: True table for the majority voter

MIF file and can be seen in the table 5.3.

After the geometric dimension we have to instruct the simulator with the micromagnetic parameters such as exchange stiffness A_{exch}, magnetization of saturation M_s and anisotropy K.

The micromagnetic parameters, like for the two dots simulation, are related to the geometric dimension of the dots and to the dose Ga^+ of the irradiated zone. The value of micromagnetic parameters are:

- Exchange stiffness $\mathbf{A_{exch}} = 1.5 \times 10^{-10} J/m$
- Anisotropy $\mathbf{K} = 2.4 \times 10^5 J/m^3$ for irradiates zones, $K = 5.2 \times 10^5 J/m^3$ for non irradiated zone
- Saturation of magnetization $\mathbf{M_s} = 7.2 \times 10^5 A/m$
- Damping $\alpha = 0.055$

Geometric parameters	Square dot	Elongated dot
Width	200 nm	420 nm
Height	200 nm	200 nm
Thickness	10 nm	10 nm
Irradiated zone dimensions	no irradiated zone	20nm x 200 nm on three side
Spacing between dots	20 nm	20 nm

Table 15.3: Geometric parameters for the majority voter simulation

Once completed the definition of geometric and micromagnetic parameters remain to define the applied clock in the MIF file. The applied clock is a square clock with a duty cycle of 0.5 and oscillating between 285 mT and -285mT along Z-axis and a component of 30 mT along Y-axis is also applied. The magnetic field along Y-axis is used to make the change of the magnetic state faster because the field along Y-axis increase the magnetic torque moment on the spins of the structures; while the period is 14ns.
The magnetic field clock characteristics are here exposed again for a rapid consulting:

- **Clock waveform** : square
- **Duty cycl**e: 0.5
- $|$ **Amp** $-$ **Z** $|$: 285 mT
- **Amp-Y**: 30 mT
- **Period T**: 14 ns
- **Application zone**: all the structure

Now the last directive to give to the simulator is how is the initial configuration of the structure, that means obviously how is the initial magnetizations state for the dots. We impose a configuration as depicted in fig 5.6.

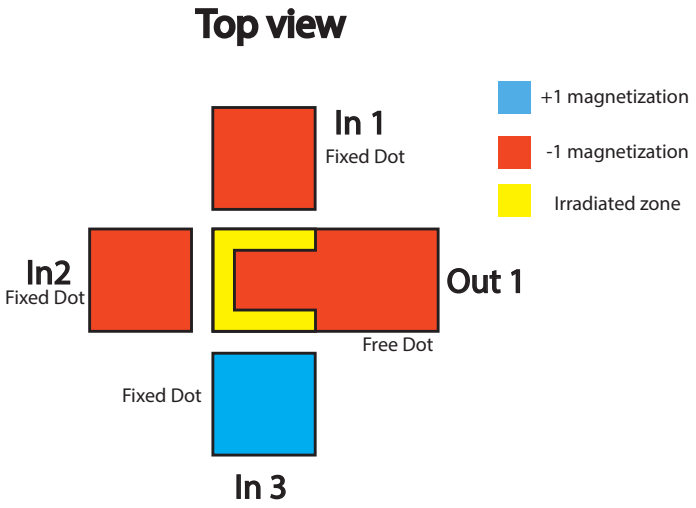

Figure 15.26: Majority voter initial configuration for the simulation

- In1 = -1 (fixed)
- In2 = -1 (fixed)
- In3 = +1 (fixed)
- Central dot = -1 (free to change)

With this configuration, according to the behaviour of th majority voter, the central dot have to switch to have a steady state system; due to this is convenient to impose the clock to start from the positive edge, so we can see soon the combined effect of the inputs configuration and the clock, since the positive edge in this configuration is the half part of the clock that helps the switching.

The simulation at this point starts and we taken screen-shots from mmDisp that is the a OOMMF application that displays two-dimensional spatial distributions of three-dimensional vectors[162]. The screen-shots of the simulation are in figure 15.27.
On the left of majority voter screen-shots, is expressed the direction of the applied clock magnetic field at that instant of time.
In figure 15.27.a there is the initial configuration for the structure under simulation; based to the theory we can predict that the central dot have to switch at the end of the positive

clock edge. In figure 15.27.b can be seen the born of the nucleation centre; differently from the two dot structure, here the nucleation event is not along the side of the dot, but is on the left high corner, this is due to the fact that the corner fells the coupling from dot In1 and In2, is the region of the structure, in this configuration, that have the highest field, so is normal that the nucleation start in that zone of the irradiated region of the central dot. Starting from the nucleation event a domain wall start to propagate (figure 15.27.c) changing slowly half magnetization of the elongated dot; the movement of the domain wall continue trough the dot (fig 15.27.d) switching completely it before the end of the positive edge of the clock.
In figure 15.27.f we can see that the clock field have now the negative edge; with the imposed configuration this field is not strong enough to force the elongated dot to switch following its direction, this confirm the correctness of the chosen value, since as said the clock helps the switching in the needed cases, but not alter the states of the structures when not needed. Also the other configurations of inputs were tested with a positive result.

The correct value of the clock amplitude and its period are not unique values because, increasing the amplitude can be increased the clock frequency but, this value can't be increased without bounds, since if the amplitude is to high, it will switch the pNML dots magnetization regardless to the system configuration having in that case all the circuit magnetizations states following the clock field direction.

15.3 An example of a fabricated circuit: a pNML Full Adder

A one bit full adder is experimentally realized [163]. As any computational logic its operation can be described using only NOT, NAND, or NOR operations, which functionality can be implemented using inverters and the majority gate structure.

Different combinations are investigated to compute the carry and the sum of the full adder [164]. This formulas are exploited using the basic structures of the nanomagnetic logic such as the majority voter and the inverters. At the end the best combination of the inputs, which allows to extract the two outputs, are:

$$S = \mathbb{M}\left[\overline{C_{out}}; C_{in}; \mathbb{M}(A, B, \overline{C_{in}})\right] \tag{15.7}$$

$$C_{out} = \mathbb{M}(A, B, C_{in}) \tag{15.8}$$

The design needs three majority gate structures and two inverters. Due to the antiferromagnetic coupling the operation performed by the majority voter is actually a minority voter evaluation so there is the need to insert other two inverter: one to invert the final output and one to invert the result of the majority voter computation $\mathbb{M}(A, B, \overline{C_{in}})$. As a consequence 4 inverters are needed. The operations that are performed are:

$$S = \overline{\mathbb{M}}\left[\overline{\mathbb{M}}(A, B, C_{in}); C_{in}; \overline{\mathbb{M}}(A, B, \overline{C_{in}})\right] \tag{15.9}$$

$$C_{out} = \overline{\overline{\mathbb{M}}(A, B, C_{in})} \tag{15.10}$$

The complete realized structure can be seen in Fig. 15.28, which shows the completed realised structure, with inputs magnets A, B, C_{in} and the outputs C_{out} and Sum. The majority gate and the inverter devices are interconnected by using magnetic nanowires. The logic operation is provided by applying an alternating clocking field, having an adequate amplitude. In this way the magnets are ordered according to the state of magnetization of the input and to the phase of the clock. The critical path of the structure for the carry is two magnets long, while for the sum is five magnets long. That means the correct computation

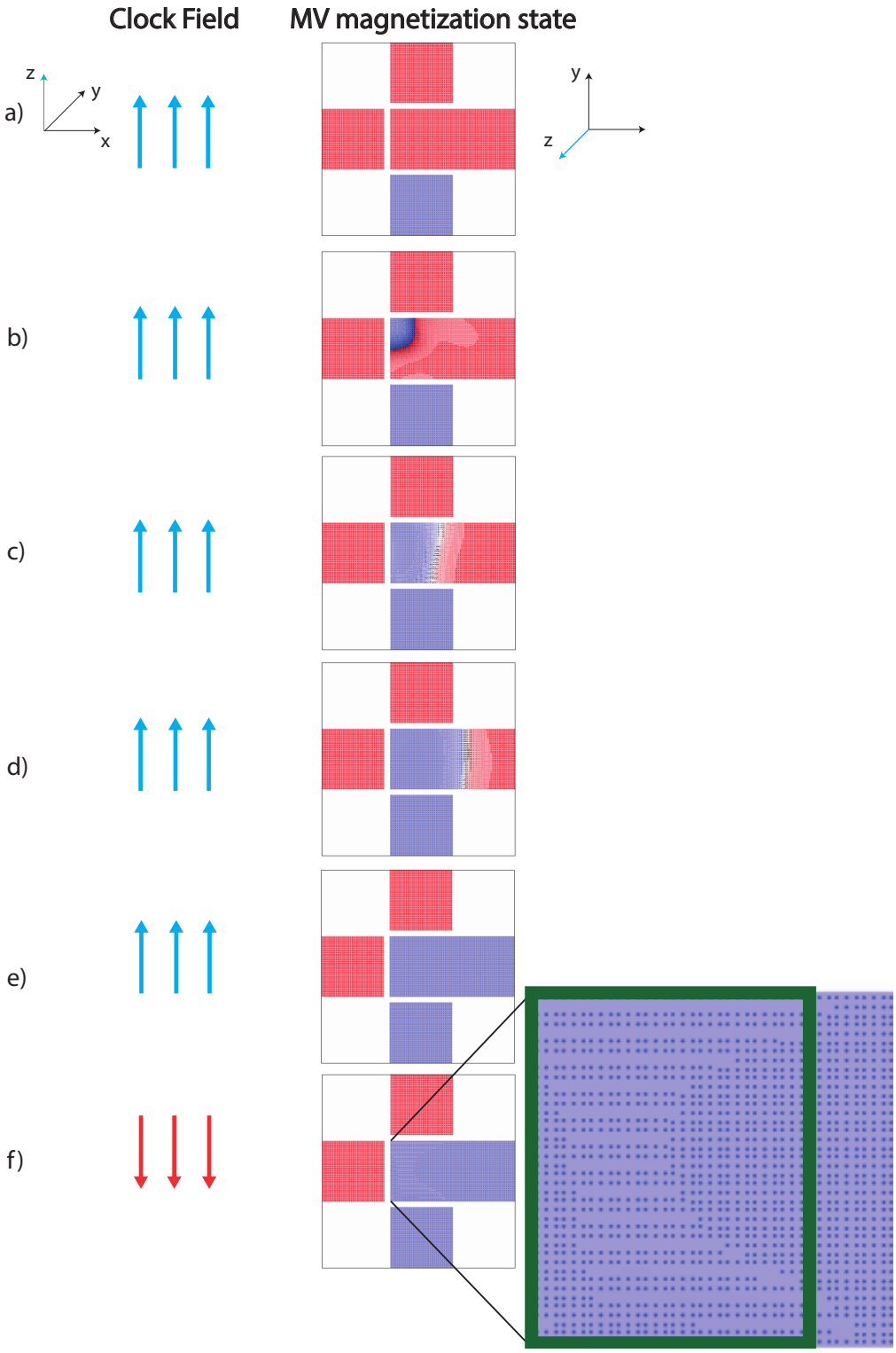

Figure 15.27: Simulation screen-shots for the Majority voter, the inputs are fixed can't switch, the elongated dot is free to switch. a) initial configuration for the mv. b) nucleation event on the left high corner of the elongated. c) domain wall start to propagate. d) propagation of domain wall. e) reverse of magnetization completed. f) the negative edge of the clock can't change the state of the ordered structure.

of the sum is assured after the carry out, so the correct operation of the circuit is assured only when the DW of the sum is propagated.

The signal propagation follows the ensuing steps:

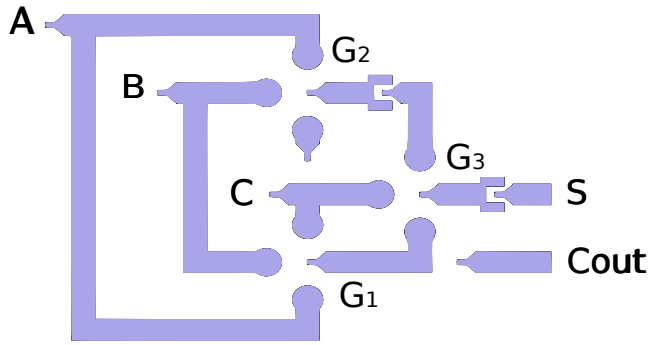

A	B	C	G_1	G_2	G_3	C_o	S
0	0	0	1	1	1	0	0
0	0	1	1	1	0	0	1
0	1	0	1	0	0	0	1
0	1	1	0	1	1	1	0
1	0	0	1	0	0	0	1
1	0	1	0	1	1	1	0
1	1	0	0	0	1	1	0
1	1	1	0	0	0	1	1

Figure 15.28: Synthesised 1-bit FA. The majority gate and the inverters are shown. The truth table is reported and the behaviour of the majority gates is underlined.

- The inputs are nucleated
- The majority gate G_1 which is in charge to compute the carry are set to the corresponding magnetization. The inversion of C_{in} is set to the desire state.
- The computation of G_2 and its inversion is done. The carry out is set to the corresponding value.
- The last majority G_3 receives its inputs and the sum is computed.

Various input combination have been studied, and the magnets order according to the magnetization state of the inputs and to the phase of the clock.

The FA experiment

The structure is fabricated with 200 nm wide $[Co_{0.8nm}Pt_{1.0nnm}]_{\times 4}$, with ANCs of $60 \times 60nm^2$ of $2.8 \cdot 10^3 \ \frac{ions}{cm^2}$. The size of the whole structure is $5 \cdot 3.4\mu m^2$ (Fig. 15.29) [164], [163]. The signal propagation with different inputs is exploited. All the input of the truth table are used and the correct behaviour of the structure is verified. The computation of the C_{out} requires one clock cycle, while to compute the final sum Sum at least another clock cycle should be waited.

Before apply the cocking field the input are set to the desired value by an high value of H_{pulse} then the pulse amplitude is reduced and an alternating clock field is applied, $H_{pulse} = 560$ Oe, with a pulse duration of $t_{clock} = 100$ ms. The corresponding signal propagation is analysed using the magnetic force microscopy MFM, and images of every state are taken to demonstrate the correct logic operation. As can be seen from Fig. 15.30, the magnets are successfully ordered and both the sum and the carry out show the correct behaviour.

15.4 Beyond the functionality: the theoretical model

The pNML technology is based on ferromagnetic materials which are characterized by a perpendicular anisotropy. In order to deeply understand the mechanisms of this technology the theoretical behaviour should be analysed. In this section the basic principles of the pNML technology are explained, in order to understand the main equations that characterize the technology, from the concept of anisotropy to the characterization of the logic behaviour.

In the first section the focus is on the magnetic anisotropy and on the domain theory, which helps to describe the behaviour of the domain wall, the transition region from one domain to the other, under the applied field, since this is the main functionality of the pNML technology. Moreover the pinning and the depinning concepts are described.

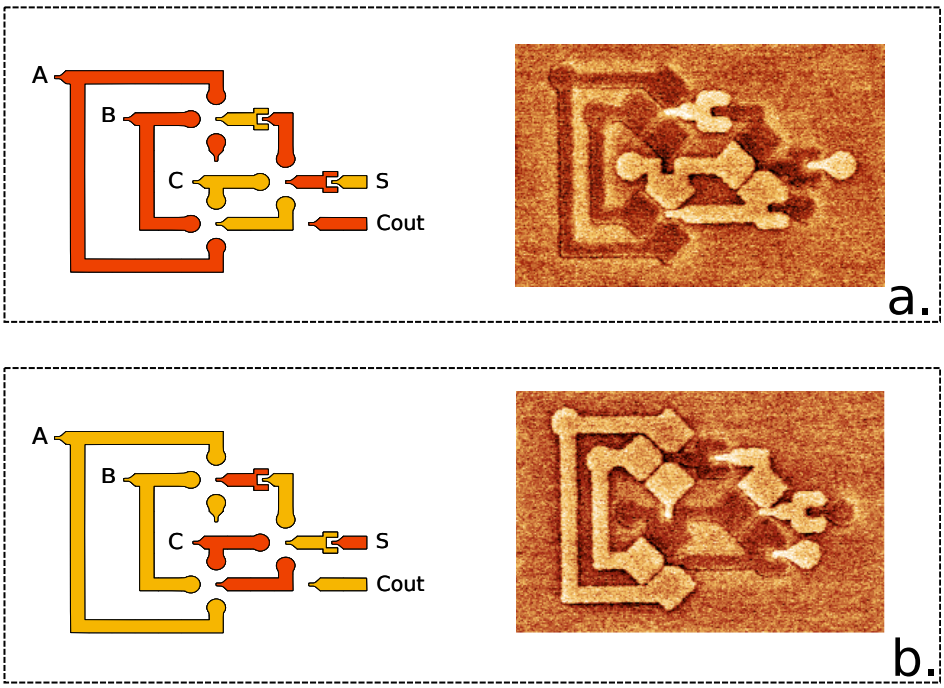

Figure 15.29: Realization of the 1-bit full adder using pNML technology. The final ordering is shown: the yellow represent the down magnetization, so the 0 logic, while the red represent the up magnetization, so the 1 logic. Two opposite cases are presented: **a.** $A = 1$, $B = 1$, $C_{in} = 0$ and **b.** $A = 0$, $B = 0$, $C_{in} = 1$, with the corresponding ordered output.

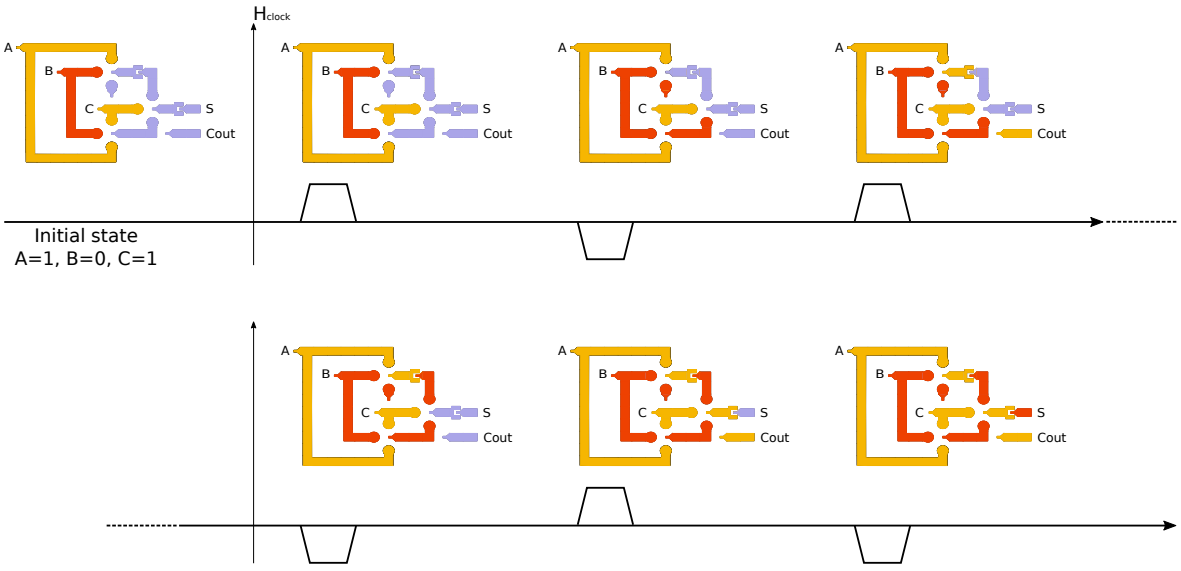

Figure 15.30: Switching behaviour of the realised one bit full adder. The case that is studied is the one having as input combination the values $A = 1$, $B = 0$ and $C_{in} = 1$. The outputs are completely ordered after three clock cycle.

In the last sections the equations which describe the nucleation, the propagation and the pinning of the new domain of magnetization are presented.

15.4.1 Multilayer magnetic anisotropy and domain theory

The magnetic multilayers structures are composed of ferromagnetic layers divided by non-ferromagnetic layers. As they becomes thinner the easy axis rotates from the in plane to the

out of plane, as a consequence the magnetic vector is perpendicular to the film surface of the nanomagnet [164]. The single nanomagnets interact among them by antiferromagnetic couplings. Ferromagnetic materials show a directional dependence behaviour that is known as the anisotropy of the material. Moreover to minimize energy, region having parallel alignment of magnetization are created. This areas are called magnetic domain and the transition region between two opposite magnetic domains is named domain wall.

The basic working principle of the pNML technology, based on multilayer films, is the manipulation and creation of domains wall motions by using magnetics fields. Therefore it is crucial to understand the required field to nucleate a DW in order to reverse the domain wall and its propagation under the applied clocking field. To control the motion of DW the concept of pinning and depinning of DW due to artificial energy barrier is explained.

15.4.2 Magnetic anysotropy

Each nanomagnet is characterized by an unique anisotropy term, which includes all the different contributions (e.g. uniaxial anisotropy, surface anisotropy, interface anisotropy, ecc.). This total anisotropy is called effective anisotropy K_{eff} [164]:

$$K_{eff} = K_u - \frac{1}{2}\mu_0 M_s^2 + \frac{2K_s}{t_{layer}} \tag{15.11}$$

where K_u is the crystalline anisotropy, K_s the surface anisotropy, M_s the saturation magnetization and t_{layer} the thickness of the layer. As a consequence the preferential behaviour of the magnetization depends on the crystal structure, the shape or geometry and material surfaces. The anisotropy energy density is defined, using the effective anisotropy, as:

$$\epsilon_{ani} = K_{eff} \cdot sin^2\theta \tag{15.12}$$

and it is minimized for $\theta \in \{0; \pi\}$ if $K_{eff} > 0$, which means that the magnetization is perpendicular with respect of the surface of the film. In other word this is the case of a perpendicular magnetic anisotropy, with the easy axis oriented perpendicularly. On the contrary, if $K_{eff} < 0$ the 15.12 is minimized for $\theta \in \{-\frac{\pi}{2}; \frac{\pi}{2}\}$ and as a consequence the easy axis lies in plane, so the magnetization is in plane. The magnetic anisotropy strictly depend on the thickness of the film, which means that there is a critical value of thickness for which the anisotropy changes from perpendicular to in plane [164].

Another important parameter for the technological point of view is the saturation of magnetization M_s. To efficiently describe the behaviour of the multilayer magnetic structures the magnetic anisotropy and the saturation magnetization are enough. Indeed, the magnetic stray energy field and the interaction of the magnets depend on M_s. The saturation magnetization is reached when all the magnetics moments are aligned in parallel with respect to the stay field.

15.4.3 Magnetic domains

In ferromagnetic materials, in order to minimize the total energy, regions of parallel magnetization are created, and the energy reduction caused by formation of domains depends on the reduction of the magnetostatic energy of field lines in space.

A transition from one domain to the opposite, requires a rotation of 180°. This rotation can happen in two different manners: parallel to the wall plane between the two domains or perpendicular to it (Fig. 15.31). According to the way of how the magnetization is reversed, the DW are called *Bloch wall* or *Néel wall*. Generally DW shows an hybrid behaviour, so both can be observed. In fact the Bloch wall shows less energy, but the Néel is more favourable for thin layers and small elements [164].

In the design of pNML gates two parameters are important: the domain wall width and the domain wall energy density. Since it is very difficult to define precisely the DW width,

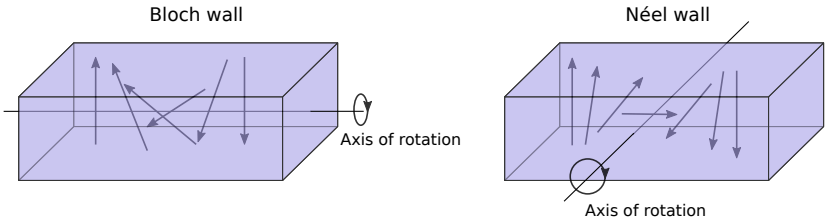

Figure 15.31: Bloch and Néel wall. Owerviwe of the 180 ° rotation of the vector of magnetization.

an asymptomatic approximation is used: the characteristic domain wall width, δ_w, which is energetically most favourable, is defined as follows [164], [165]:

$$\delta_w = \pi\sqrt{\frac{A}{K_{eff}}} \tag{15.13}$$

where A represents the exchange interaction between spins and effective anisotropy. The energy density is given by:

$$\sigma_w = 4\sqrt{AK_{eff}} \tag{15.14}$$

This latter parameter influences the behaviour of the DW in case of geometry variations. It is very important to consider it specifically in the design of artificial pinning sites, as it will be discussed later in section 15.4.6 and in 15.7.

15.4.4 Nucleation of the domain wall

The nucleation of the DW includes the generation of the new magnetic domain, which means reverse the current magnetization of the DW. The reversal starts in a small spot which has less anisotropy, so the total reverse of the domain in thin multilayer structures starts with the domain nucleation and then continues with the propagation of the new domain though the entire nanomagnet. The nucleation can be modelled according to the Stoner-Wohlfarth model and the field required to reverse the magnetization of an area having effective anisotropy K_{eff} is given by the following equation [164]:

$$H_{ani} = \frac{2K_{eff}}{\mu_0 M_S} \tag{15.15}$$

where M_S is the saturation magnetization of the magnet:

$$M_S = M_{S,Co}\frac{t_{Co}}{t_{stack}} \tag{15.16}$$

$M_{S,Co} = 1.4 \cdot 10^6$ A/m is the value for Co saturation magnetization, t_{Co} is the thickness of cobalt in the overall magnetic multilayer stack thickness t_{stack}.

The field is proportional to the anisotropy, so, as a consequence, the starting point of the switching operation is the area which has less anisotropy. For this reason the artificial centre of low anisotropy is created (the ANC), which allows to control the switching process of the magnet. In fact, during the process of fabrication defects having less anisotropy can be distributed randomly along the magnet.

15.4.5 Domain propagation

The propagation entails the motion of the DW and the expansion of the most favourable magnetization domain. The propagation is characterized by a speed of motion, the DW velocity v_{DW}, which depends on the applied field, as will be discussed in 15.5.1.

Three main regimes can be identified in the propagation of the new state in thin multilayer structures. These regimes are modelled according to the external field H_z applied to the

magnetic structure. This field is compared to the intrinsic pinning field, the field needed for DW depinning at zero temperature H_{int} [164]:

- Creep regime: $H_z \ll H_{int}$. The DW depinning depends on the defects which are thermally activated. The motion is called creep motion.
- Depinning regime: $H_z \approx H_{int}$. The motion is still thermally activated. It is an intermediate region between the creep and the flow regime.
- Flow regime: $H_z \gg H_{int}$. The disorder of the magnetic material becomes irrelevant and the motion is governed by flow dynamics.

According to the regimes the velocity v_{DW}, so the speed of the domain expansion (the propagation of the new domain) through the structure changes (15.5.1).

15.4.6 Pinning of the DW

The depinning of the domain wall is very important for the operation of the pNML circuits, as well as the pinning operation. This two complementary operations are strongly influenced by defects and edge roughness of the structure. One of the main consequences of unwanted pinning is the incomplete switching of the domain wall which means error in logic operation of the device. However, some advantages can be taken from the pinning. Wanted geometrical deformation such as notches can be used to create an energy barrier which blocks the transmission of the operation. In fact all the geometric variations influence the effective anisotropy of the structure, so an higher field is required to overcome the energy barrier to change the domains, as will be further discussed in section 15.7

Not only geometrical deformations act on the pinning operation but also local modification on the anisotropy. To better control the nucleation of the magnet the anisotropy is locally reduced at one end: the transition from domains having different anisotropy acts as an energy barrier. As a consequence there is the need of a field to pass from the FIB irradiated to the non-irradiated area. This technique, which reduces locally the anisotropy, can not be applied in the pNML circuitry since other centres with low anisotropy may influence the correct operation of the device. In fact, there is the risk of having the presence of unintentional irradiates areas due to the presence of the other magnets, and so the DW can be nucleated.

15.5 Characterization of the DW propagation

The propagation of the new domain is characterized by a velocity and so by a time of propagation. This two constants are influenced, in addition to the technological parameters, by the length of the domain wall and by the applied external clock field.

15.5.1 Regimes and DW velocity of propagation

The velocity v_{DW}, so the speed of the domain expansion (the propagation of the new domain) through the structure changes according to the applied external field, so according to the clocking field. As described before (see 15.4.5) three main regimes can be identified and according to them v_{DW} is described by the following equations (Fig. 15.32):

- Creep regime: the speed is very slow $v_{DW} \ll 1$ m/s and it is described by:

$$v_{DW}(H_z \ll H_{int}) \approx v_0 \cdot e^{-\frac{E_{pin}}{k_B T}\left(\frac{H_{int}}{H_z}\right)^{\frac{1}{4}}} \tag{15.17}$$

where v_0 is a numerical prefactor.

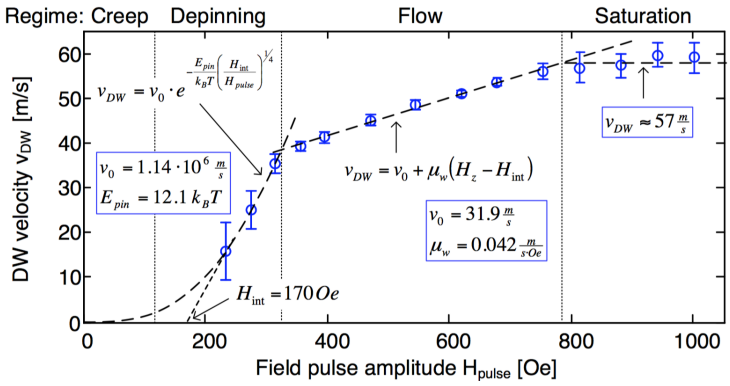

Figure 15.32: Domain wall velocity measured experimentally in a snake structure [164] as a function of the applied clock field, H_{pulse}. According to it the velocity changes.

- Depinning regime: The velocity increase exponentially with the applied field, however it strictly depends on the temperature too, according to the equation 15.17.
- Flow regime: The velocity depends linearly on the applied field and can be modelled according to the equation:

$$v_{DW}(H_z \gg H_{int}) = v_0 + \mu_w(H_z - H_i nt) \tag{15.18}$$

where v_0 is a numerical prefactor and μ_w is the domain wall mobility.

Theoretically the velocity is linear to the applied field so the used working regime is the flow regime.

15.5.2 DW propagation time

After the nucleation of the artificial nucleation centre the new magnetization state is propagated along the structure. The velocity of the propagation changes according to the applied H_{clock}, so according to the regime in which it is classified: creep, depinning and flowing. The propagation time t_{prop} can be defined as follows:

$$t_{prop} = \frac{l_{mag}}{v_{DW}(H_{clock})} \tag{15.19}$$

where l_{mag} is the length of the magnet. The domain propagation time adds a delay between the nucleation and the complete reversal magnetization.

15.5.3 Experiment

To estimate and validate the theoretical model for the propagation velocity, a 400 nm wide magnetic nanowire $Pt_{5nm}\,[Co_{0.8nm}Pt_{1.0nm}]_{\times 4}\,Pt_{5nm}$ is fabricated and by using a wide-field magneto-optical Kerr microscope (WMOKE) based on a modified optical microscope with polarizing optical elements, the l_{prop} is measured [164] [166]. 50 different amplitude pulses are applied and for each H_{pulse} the l_{prop} is measured. Then the v_{DW} is estimated according to:

$$v_{DW} = \frac{l_{prop}(H_{pulse})}{t_{eff}} \tag{15.20}$$

The results obtained are fitted in a graph with the theoretical results (Fig. 15.32). They both are coherent [166]. To propagate the magnetization a minimum field is required ($H_{pulse} > H_{int}$) and after a certain H_{pulse} it saturates to 57 m/s. The corresponding field pulse in this case is $H_{pulse} > 750$ Oe. The three regimes can be distinguished. The depinning regime goes from $H_{int} = 190$ Oe $< H_{pulse} <$ 330Oe, in which the velocity is

dominated by the pinning and depinning phenomena due to the roughness and defects of the material. For fields greater than 330 Oe the flowing regime can be identified and the velocity grows linearly with the applied field according to the equation 15.18. The prefactor is equal to $v_0 = 31.9$ m/s and the domain wall mobility is $\mu_w = 0.042$ m/sOe.

15.6 Characterization of the DW nucleation

The nucleation of the DW includes the generation of the new magnetic domain, which is the opposite of the current magnetization.

The H_{nuc}, nucleation field, required to switch the DW, according to the theory, should be equal to the H_{ani} (eq. 15.15), nevertheless, due to defects in the multilayer structure it can be lower than it.

$$H_{nuc} = max(H_{ani}, H_{depin}) \tag{15.21}$$

H_{depin} is the reduced field, due to defects, necessary to overcome the energy barrier.

An important role is played by the thermal energy and this dependence can be modelled according to the Stoner-Wohlfarth model for the reversal particle [164]. The energy barrier, which should be overcame in order to switch, is decreased by the applying field:

$$E_{barrier} = K_{eff} V \left(1 - \frac{H_z}{H_0}\right)^2 \tag{15.22}$$

where V is the volume of the particle. The coercive field at zero temperature H_0 is equal to H_{ani} (15.15). To get the switching rate the energy barrier is applied to a conventional Arrhenius model:

$$r = f_0 e^{-\frac{E_{barrier}}{k_B T}} \tag{15.23}$$

f_0 correspond to the attended frequency and it is in the order of GHz.

The 15.22 can be manipulated taking in account that:

$$V = \frac{2E_0}{\mu_0 M_s H_0}; \qquad H_0 = \frac{2K_{eff}}{\mu_0 M_s} \tag{15.24}$$

$$E_{barrirer} = E_0 \left(1 - \frac{H_z}{H_0}\right)^n \tag{15.25}$$

the factor n is 1 or 2 according to if the rotation of the magnetization reversal is coherent or if it is a DW nucleation, respectively. E_0 is the energy barrier at zero field. Due to the presence of the ANC, the $E_{0,ANC}$ can be expressed as [167]:

$$E_{0,ANC} = K_{ANC} V_{ANC} \tag{15.26}$$

where V_{ANC} is the volume of the artificial nucleation centre and K_{ANC} is the anisotropy of the ANC and can be obtained from the effective anisotropy K_{eff} and the FIB irradiation factor g_{FIB}:

$$K_{ANC} = g_{FIB} K_{eff} \tag{15.27}$$

Also the $H_{0,ANC}$, the field required to change the magnetization direction of the ANC at absolute zero can be derived taking in account the K_{ANC}, instead of the K_{eff}, in equation 15.15.

The nucleation or not of the domain wall can be estimated by exploit the probability of nucleation, expressed in terms of applied field H_z and of the duration time of the field. It is described by using the Arrhenius model:

$$P_{nuc}(t, H_z) = 1 - \exp\left(-\frac{t}{\tau(H_z)}\right) \tag{15.28}$$

$$\tau(H_z) = r^{-1} = f_0^{-1} \cdot \exp\left(\frac{E_0\left(1 - \frac{H_z}{H_0}\right)^n}{K_B T}\right) \tag{15.29}$$

$\tau(H_z)$ is the reverse of the switching rate so the switching time constant.
The clock amplitude field, H_{clock}, should be enough to nucleate the DW. If the equation 15.28 is solved with respect to H_z, considering a probability of 0.5, the switching field amplitude, so the field required to reverse the particle, can be extracted according to the following equation [167], called Sharrock formula:

$$H_{sw}(t_p) = H_0\left[1 - \left(\frac{k_B T}{E_0} ln\left(\frac{f_0 t_p}{ln(2)}\right)\right)^{1/2}\right] \tag{15.30}$$

To achieve the signal flow, the nucleation of the magnet has to be controlled by another magnet which acts as an input. The control is done by the stray fields of the input magnets which surround it. Since its strength decreases with the increasing of the distance of the inputs, they have to be as closed as possible to the output, and the nucleation centre of the output should be as small as possible in order to have a distinct and equal influence of the input stray fields C [164]. This influence can be clearly seen from Fig. 15.33. As a consequence the nucleation field which is required to nucleate the domain wall is influenced by the superposition of those coupling fields.

$$H_{eff} = H_{clock} - C_{eff} \tag{15.31}$$

Where C_{eff} is:

$$C_{eff} = \sum_{i=1}^{N} C_i M_i \tag{15.32}$$

C_i are the superposed coupling fields from the inputs with magnetization $M_i \in \{-1; 1\}$ [166]. The coupling field C_i is function of the input size A_i and of the distance d_i from the ANC of the output. It scales as:

$$C_i \propto \frac{A_i^{n_1}}{d_i^{n_2}} \tag{15.33}$$

where n_1 and n_2 are geometrical dependent parameters: $0 < n_1 \leq 1$ and $1 < n_2 \leq 3$ [164]. The normalized magnetization M_i influences the energy barrier which increases or decreases according to the input magnetization. In fact in the case that the input and the current state of the magnet are in a parallel state, so both have the same direction of the magnetization vector, $M_i = -1$, the H_{eff} increases to encourage the nucleation of the DW; while in the case of the antiparallel state $M_i = 1$ and the nucleation is prevented. Each M_i is weighted by its coupling field C_i, which is calculated by numerical finite element simulations. The output magnetization after the clocking field is [168]:

$$M_{out} = -sgn\left(\sum_{i=1}^{N} C_i M_i\right) \tag{15.34}$$

The probability to nucleate the ANC with a magnetic field pulse of amplitude H_{pulse} and effective pulse time t_{eff} is:

$$P_{nuc}(t_{eff}, H_{pulse}) = 1 - \exp\left(-\frac{t_{eff}}{\tau(H_{pulse})}\right) \tag{15.35}$$

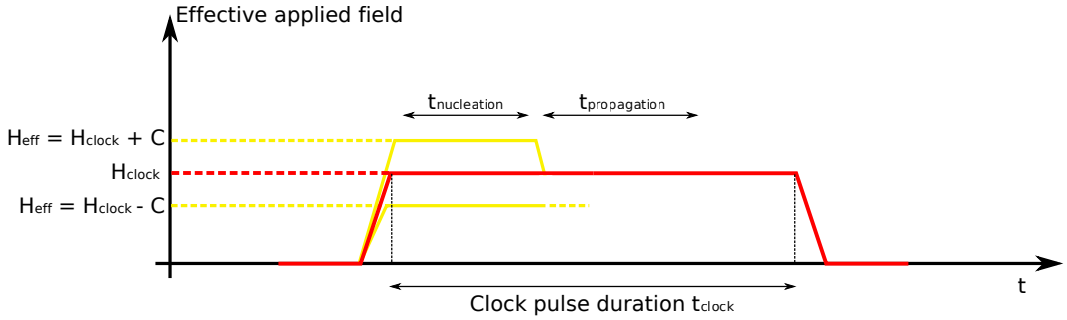

Figure 15.33: Overview of the effective applied external filed. During the nucleation the contribution of the coupling fields C of the neighbouring magnets increases or decreases the total applied field. As a consequence the nucleation can be supported or prevented respectively.

$$\tau(H_{pulse}) = f_0^{-1} \cdot \exp\left(\frac{E_0\left(1 - \frac{H_{pulse}}{H_0}\right)^2}{K_B T}\right) \tag{15.36}$$

Due to the influence of the coupling field the probability of nucleation changes. In fact the nucleation probability is shifted according to the coupling field C of the input. The increasing and the decreasing of the P_{nuc} are due to the changing value of H_{eff}: in the first case, when the magnet should switch, the nucleation is supported by C_{eff} and the magnet, in order to prevent errors and to complete the propagation of the new domain along the whole DW, has to nucleate during the time t_{nuc} (15.51); in the second case, if the magnet should not switch, the nucleation during all the t_{clock} is prevented [166]. This consideration can be translated into two constraints on the nucleation probability:

$$P_{nuc}(t_{nuc}, H_{clock} + C) \to 1 \tag{15.37}$$

$$P_{nuc}(t_{clock}, H_{clock} - C) \to 0 \tag{15.38}$$

The 15.37 supports the nucleation, while 15.38 prevents the nucleation. The error rate of a device during one clock clycle is given by:

$$E_{device} = 1 - P_{nuc}(t_{nuc}, H_{clock} + C) \cdot [1 - P_{nuc}(t_{clock}, H_{clock} - C)] \tag{15.39}$$

By minimizing the error rate the most suitable clocking field amplitude can be determined. The nucleation probability and therefore the reliability of the whole pNML circuit strongly depends on the nucleation time t_{nuc}, on the clocking pulse time t_{clock} , on the field amplitude H_{clock} and especially on the coupling fields C [166].

The time required to nucleate a DW can be expressed in terms of probability to nucleate it:

$$t_{nuc} = -\tau(H_{eff}) \cdot \ln(1 - P_{nuc}) \tag{15.40}$$

so it can be computed according to the wanted P_{nuc} (eq. 15.35).

15.6.1 Experiment

A 400 nm wide magnetic nanowire $Pt_{5nm}\left[Co_{0.8nm}Pt_{1.0nm}\right]_{\times 4} Pt_{5nm}$ is fabricated [164]. To estimate the t_{nuc} firstly the magnet is saturated to a down state then a pulse field is applied having an effective pulse duration of t_{eff} ($t_{eff} = t_{clock} - t_{rise}$). The propagation length is measured and the propagation time t_{prop} is extracted (eq. 15.19). The nucleation time is computed as:

$$t_{nuc} = t_{eff} - \frac{l_{prop}}{v_{DW}(H_{pulse})} \tag{15.41}$$

To extract the nucleation probability the procedure is repeated several times. Firstly the probability density is extracted dP_{nuc}/dt with respect to the nucleation time. If the pulse field amplitude increases the probability density is shifted towards shorter times. For an amplitude of $H_{pulse} = 889$ Oe the domain wall nucleates during the first 60 ns. The total P_{nuc} with respect to the pulse field amplitude is extracted. As a result the P_{nuc} strongly depends on the H_{pulse} and is sufficient a $\Delta H_{pulse} = 90$ Oe to prevent or guarantee the DW nucleation for $t_{eff} = 120ns$ [166].

The results are compared to the theoretical model and the structure and material dependent parameters ($E_0 = 181 k_B T$ and $H_0 = 1036$ Oe) are extracted.

The reliability of the structure is exploited. By using the conditions 15.37 for $t_{nuc}(H_{pulse} = 890Oe) \leq 60ns$ and 15.38 for $t_{nuc}(H_{pulse} = 800Oe) > 120ns$, C_{eff} is extracted. It is sufficient a coupling field greater than 45 Oe to guarantee a correct operation [164].

The influence of the coupling field is investigated also for other structures [164] [166], since the coupling field reduces or increases the applied clocking field, according to the input state M_i.

Inverter

An inverter structure is created to determine the influence of C_{eff} on the nucleation time and on the nucleation probability [164]. In the case of the parallel case, so both the input and the output have the same magnetization vector the coupling field is added and the mean DW nucleation time is reduced to 20 ns for $H_{clock} = 549$ Oe. In the opposite case, so in the antiparallel case, the C_{eff} reduces the field and the DW nucleation is impeded. Any nucleation event has been seen for $H_{eff} = 549$ Oe. For both the cases (parallel and antiparallel) the P_{nuc} is computed with respect to the applied field. This experimental results are used to determine the energy barrier at 0 field E_0, the coercive field at zero temperature H_0 and the input coupling field C. By fitting the obtained nucleation probability with the Arrhenius model the following results are determined: $E_0 = 117/k_B T$, $H_0 = 650$ Oe and $C = 90$ Oe [164]. That means the nucleation probability is shifted by $\pm C$.

Minority voter

The influence of the magnetic coupling field has been investigated also for the minority gate structure [164]. The superposition of the coupling fields of the three input magnets on the ANC of the output influences the logic operation, which is performed according to the majority decision. The central position of the ANC ensures equal influence of each input, so a non-alignment can cause error in computation [169]. After having set the input configuration the switching behaviour is measured. The output hysteresis curve depends on the configuration of the input. In fact, due to the influence of the input coupling fields on the ANC, the hysteresis curve is shifted to left or right. The nucleation probability and the density of the nucleation probability is extracted [164]: it is prevented orr supported according to the coupling fields and to the magnetization input vector. The results obtained matches with the theoretical model. The influence of the coupling field can be classified in three main behaviours, assuming that $C_i \approx C$:

- $C_{eff} = -C_1 - C_2 - C_3 = -3C$: C_{eff} is maximized and the nucleation is supported. The required clock field amplitude is the slowest.
- $C_{eff} = -C$: One input state is different from the others and it is in the antiparallel state. The nucleation is still supported, but an higher H_{clock} is required to nucleate the output ANC with respect to the previous case.
- $C_{eff} = C$: Only one input state is in the parallel state. The nucleation is not supported.
- $C_{eff} = C_1 + C_2 + C_3 = 3C$: The nucleation is prevented. The H_{eff} is minimized.

The values of C_i are determined experimentally by determining the H_{nuc}, tacking in account that due to the coupling field they are shifted by $\pm C_i$. The difference between the H_{nuc} of opposite input vector magnetization gives the value of the coupling field of that input.

Interconnection

The branch structures, which split the input in two or three according to their function are investigated [164] since they are an important feature for interconnections. It has been demonstrated that the depinning field H_{branch} can be derived with respect to the open angle of the branch θ_{branch} and the width of the wire H_{wire}:

$$H_{branch} = H_{int} + \frac{\sigma_w \sin\theta_{branch}}{2M_s h_{wire}} \tag{15.42}$$

A $[Co_{0.8nm}Pt_{1.0nm}]_{\times 4}$ structure is fabricated and the fields are measured [164]. The results match very well the nucleation field, as a consequence the DW propagation is always verified in the branch since $H_{branc} < H_{nuc}$.

15.7 Characterization of pinning and depinning of the DW: notch structures

Besides the flow of magnetic domains through the nanowire, it is also required to store the signal within the nanowire in order to buffer magnetic domains. In pNML systems the domain wall can be pinned (and depinned) in a controlled way. Pinning of domains can be caused by several reasons, but generally it is due to either geometry variations or the variation of the anisotropy of the material. As explained in 15.4.6, geometry variations are mainly used to control the depinning of the domain wall since a variation in the anisotropy brings to a less reliable logic behaviour. Deformations in magnetic nanowire are called notches and they create energy barriers with a specific energy which should be overcome to propagate DW [165], [164].

For a single-sided notch in a magnetic nanowire, the depinning field H_{dep}, which is required to depin the DW, is:

$$H_{dep} = H_{int} + \frac{\sigma_w sin\alpha}{2M_s(h + \frac{1}{2}\delta_w sin\alpha)} \tag{15.43}$$

where α is the notch apex angle and h the notch width, as is depicted in Fig. 15.34 a.. When the notch thickness is much larger than the domain wall thickness ($h \gg \delta_w$) a simplification can be done:

$$H_{dep} = H_{int} + \frac{\sigma_w sin\alpha}{2M_s h} \tag{15.44}$$

Which means that for smaller DW energy densities and larger notch thickness it should be easier to depin the propagation from the notch. The average DW depinning time is the time required to depin a DW from a notch which is characterize by a depinning field H_{dep} by applying a field H. It is described by the following equation:

$$t_{dep} = \tau_0 \cdot e^{\frac{M_s V_a (H_{dep} - H)}{K_B T}} \tag{15.45}$$

where V_a is the activation volume and τ_0 is the reverse of the attempted frequency f_0 [165]. A theoretical value for the depinning field can be defined, but since the process of depinning is a statistical process, where temperature plays an important role and can help to overcome the energy barrier of the notch, it is important to define the probability to depin the DW from the notch. This helps to define also the reliability of the circuit. Based on the Stoner-Wohlfahr model the energy barrier can be defined as [165]:

$$E_{barrier} = M_s V_a (H_{depin,theory} - H_{eff,exp}) \tag{15.46}$$

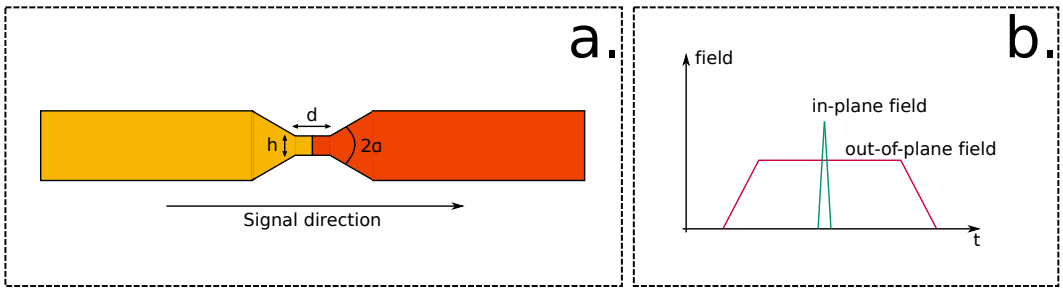

Figure 15.34: **a.** Representation of a notch and of its geometrical characteristics. **b.** Applied out-of-plane field and in-plane field. The in-plane field increases the clocking field in order to depin the notch.

where $H_{depin,theory}$ is the depinning field computed according to the theoretical model (eq. 15.44) and $H_{eff,exp}$ the effective applied magnetic field which is a combination of the in- and out-of-plane field. In fact to depin the notch an in-plane field is applied, as it will describe below. The time constant which describes the switching of the magnetization can be explained by the Néel-Brown formula and is given by:

$$\tau(H_{eff}) = \tau_0 e^{\frac{E_{barrier}}{K_B T}} \tag{15.47}$$

From these equations the depinning probability follows from the Arrhenius model:

$$P_{dep} = 1 - e^{\frac{t}{\tau(H_{eff})}} \tag{15.48}$$

where t is the time of duration of the applied effective field H_{eff}. For a robust device the transition between pinning and depinning should be a sharp as possible, otherwise the magnetic domains are sometimes depinned when actually needed to be pinned.

15.7.1 The in-plane depinning field

To depin the magnetic domain from the notch an external field has to be applied. Indeed, in structures where notch are also present there is the need of two external fields: the clock field which is required to propagate the information and the in-plane field which is necessary to depin the information from the notch (Fig. 15.34 b.).

The out of plane clock field applied externally, which is required to switch correctly the domain wall and propagate the new domain, has an amplitude that is not enough to depin the notch. As a consequence, if a constant amplitude clocking field would be applied there is the need to reduce the depinning field of the notch. This is done by adding an in-plane field to the nanowire. In this way the field strength, which is needed to transfer the signal, is reduced. Two conditions can be defined, according to the presence or not of the external in-plane field:

$$H_{dep} = H_{notch} < H_{clock} = H_{nuc} \tag{15.49}$$

$$H_{dep} = H_{notch} > H_{clock} = H_{nuc} \tag{15.50}$$

In the first case (eq. 15.49) the in plane field is applied and the propagation of the domain is allowed, in the second case (eq. 15.50) the propagation is blocked by the notch. The sub-μs in-plane field pulses are generated by current pulses on-chip coil.

15.7.2 Experiments

In [165], some measurements are carried out in order to verify theoretical model and the behaviour of the domain wall in presence of geometrical variation. The measured notch has an apex angle $2\alpha = 51.5°$, notch thickness $h = 54$ nm. The in-plane field which has been applied has a duration of 200 ns. The out-of-plane field, so the clock field, has been generated independently from the in-plane field, but within a certain overlapping time interval, in order to be able to propagate the domain after the depinning of the notch.

Different amplitudes of the in-plane field are applied and the dependency of the depinning field has been demonstrated: the depinning field is a function of the applied in-plane field and it decrease as the in-plane increases.

Another important aspect has been found in the experiments. According to the applied in-plane field the type of the domain wall changes: a combination of a Bloch and Néel wall is observed. For larger in-plane fields the domain wall becomes a Néel wall.

15.8 Signal flowing

To propagate the information an alternating clock field is required. The amplitude of the clock field H_{clock}, which acts both as internal clock and power supply, should be adequate to force the magnet to switch to the antiparallel state with respect to the input magnet due to the antiferromagnetic coupling. The alternating clock field provides the required energy to switch the magnets, in the correct direction. The amplitude of this pulse field influence the reliability of the circuit [164].

To nucleate the magnet its energy barrier should be reduced. The artificial centre of nucleation (ANC), having low anisotropy, supports the nucleation, by reducing locally the energy required to switch the magnetization. The clocking field supports the nucleation and, moreover, it drives the completely reversion of the domain in the DW.

Two main steps are required to propagate the new domain: the nucleation of the domain wall, and the propagation of the reverse of the current magnetization along the whole magnet. In order to guarantee an operation without errors the switching process should be completed during the clock field pulse time t_{clock}. As a consequence all the operation required to switch the magnet, so the nucleation of the domain wall and the propagation of the new magnetization, should be done before the end of the clock pulse time [166]. This give a constraint on the switch time t_{switch}:

$$t_{switch} = t_{nuc} + t_{prop} < t_{clock} \tag{15.51}$$

where t_{nuc} is the nucleation time and t_{prop} the required time to propagate the magnetization through the entire domain wall, so to reverse all the domains.

15.9 Racetrack memories and logic

..... coming in the next version of the LN....

CHAPTER 16

Skyrmions: device, memories and logic

16.1 Physics and applications of skyrmions

In the following the main physical laws and properties of skyrmions will be described, together with the issues in using them as information carriers. Some applicative aspects, that can either be useful to better understand the practical meaning of some physical properties, or that can be helpful in solving the main issues, will be presented too. The aim of this chapter is not to give an exhaustive and detailed insight into the complex physical phenomena linked to these topological configurations, but just to offer an overview on the principal difficulties and on the main mechanisms involved when trying to use skyrmions as information carriers inside computing architectures. The end of the chapter, moreover, will show a breif description of some applications which exploit and sum up well all the physical characteristics exposed in the first part.

16.2 Physical properties

To employ skyrmions as information carriers it is of vital importance the ability of performing some elementary tasks, including their creation, manipulation, detection and eventually annihilation. The first topic addressed in this section is the structure of a skyrmion and what are the main energetic contributions that compete in its creation. Then will be described the laws of motion and the main possibilities available to move it along the device; finally it will be detailed how is possible to nucleate it and to detect it. The topic of the skyrmion radius will be discussed at the end of the section, since it exploits some results presented in other papers.

16.2.1 Topological properties

Topological charge

A magnetic skyrmion is a non-collinear 2D configuration of magnetic moments resulting from the competition of different energetic terms (which will be detailed in section 16.2.2). This configuration has a whirling structure, like shown in figure 16.1, and is described from a topological point of view by the topological charge Q, also called skyrmion number or Pontryagin number; its expression is [1]

$$Q = \frac{1}{4\pi} \int dxdy(\partial_x \boldsymbol{m} \times \partial_y \boldsymbol{m}) \cdot \boldsymbol{m} \tag{16.1}$$

[1] Like observed in [170], the sign in this formula is not consistently defined in literature. An example in which the topological charge is defined with a minus sign can be found in [171].

where $\boldsymbol{m}$ is the unit vector representing the orientation of the local magnetic moment. The skyrmion number counts how many times the magnetic spins constituting the structure of the skyrmion can be wrapped around a unit sphere: all the spins at the boundary are collected into a single vector mapped on one pole of the sphere, and this is possible only because these spins point all in the same direction; the core is mapped at the opposite pole of the sphere, while the intermediate spins are mapped on the remaining parts of the sphere. In the case of a skyrmion-like structure, the topological charge is an integer equal to ± 1.

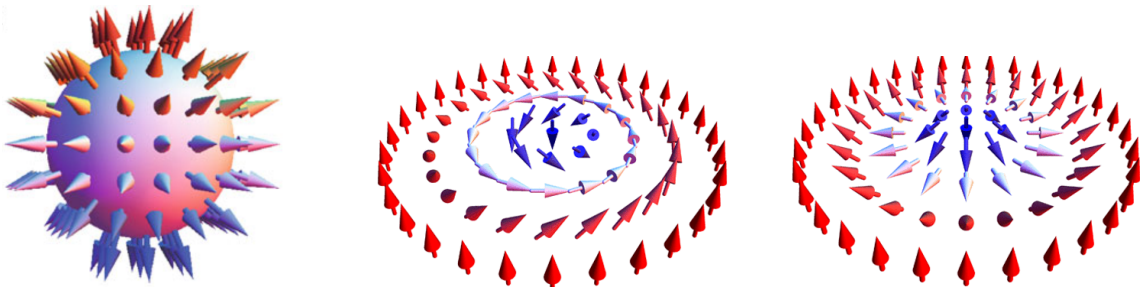

(a) (b) (c)

Figure 16.1: (a) Mapping of the Néel skyrmion onto the unit sphere. Figure extracted from [172]. (b) Bloch skyrmion, (c) Néel skyrmion. Figures extracted from [173].

The magnetization of a skyrmion in polar coordinates [174] is described by

$$\boldsymbol{M} = M_S \begin{bmatrix} cos\phi(\varphi)sin\theta(r) \\ sin\phi(\varphi)sin\theta(r) \\ cos\theta(r) \end{bmatrix} \tag{16.2}$$

while the expression of $\boldsymbol{r}$ in polar coordinates is $\boldsymbol{r} = r(cos\varphi, sin\varphi)$. Inserting equation 16.2 into equation 16.1 it can be obtained that

$$Q = \frac{1}{4\pi}\int_0^{\infty} dr \int_0^{2\pi} d\varphi \frac{d\theta(r)}{dr}\frac{d\phi(\varphi)}{d\varphi} sin\theta(r) = \frac{1}{4\pi} cos\theta(r)\Big|_{r=0}^{r=\infty} \phi(\varphi)\Big|_{\varphi=0}^{\varphi=2\pi} \tag{16.3}$$

This equation will be commented later in section 16.2.1.

The in-plane magnetization angle ϕ is assumed to be a linear function of the azimuthal angle φ [174], so that

$$\phi = m\varphi + \gamma \tag{16.4}$$

This equation will be discussed later in section 16.2.1. For now is enough to remember this: let's assume that the skyrmion's structure lays in the xy-plane; the magnetic moments are organized on circumferences that are concentric with the skyrmion core (of course in first approximation and only if the skyrmion is not being deformed); the angle giving the position of each magnetic moment along the corresponding circumference with respect to the x-axis is φ, with unit vector $\hat{\varphi}$. Then, ϕ is the angle that the spin at position φ has with respect to the unit vector $\hat{\varphi}$. For example, in the skyrmion represented in figure 16.1c, each moment has angle $\phi = 0$, while in the skyrmion shown in figure 16.1b each moment has an angle $\phi = \frac{\pi}{2}$.

Dzyaloshinskii-Moriya Interaction

The Dzyaloshinskii-Moriya Interaction (DMI) is a key element for the stabilization of magnetic skyrmions. The bulk DMI comes from the breaking of the bulk inversion symmetry ($\boldsymbol{r} \nrightarrow -\boldsymbol{r}$) and from the presence of atoms with high spin-orbit coupling in ferromagnetic alloys (for example B20 materials). The interfacial DMI (i-DMI) comes instead from the

breaking of the structure inversion symmetry ($z \nrightarrow -z$) at the interfaces of a multilayer system, where a thin layer of ferromagnetic material is deposited above a substrate made of a material with large spin-orbit coupling (for example Co on Pt) [175, 176].

These two types of DMI give rise to two different types of skyrmion structures, both shown in figure 16.1: the Bloch skyrmion (also spiral skyrmion) and the Néel skyrmion (also hedgehog skyrmion). In both cases there is a central domain and an outer domain, both with out-of-plane magnetization, separated by a domain wall. When the domain wall has a circular chirality (either clockwise or counterclockwise) the skyrmion is a Block skyrmion: in this case the magnetization rotates in the tangential plane while going from the core to the tail of the skyrmion. If the domain wall has a radial chirality (either inward or outward), then the skyrmion is of Néel type and the magnetization rotates in the radial plane [175, 173].

The DMI is an interaction between two magnetic spins mediated by the presence of a third non-magnetic atom with a strong spin-orbit coupling (SOC). The Hamiltonian of this interaction is

$$H_{DM} = -\boldsymbol{D}_{12} \cdot (\boldsymbol{S}_1 \times \boldsymbol{S}_2) \tag{16.5}$$

where $\boldsymbol{S}_1$ and $\boldsymbol{S}_2$ are the two magnetic spins and $\boldsymbol{D}_{12}$ is the DMI vector, perpendicular to the plane containing the three atoms involved. Starting from a ferromagnetic state with $\boldsymbol{S}_1$ parallel to $\boldsymbol{S}_2$, the DMI tilts $\boldsymbol{S}_1$ with respect to $\boldsymbol{S}_2$ by a rotation around $\boldsymbol{D}_{12}$ [177]. This energetic term is minimized when the two magnetic spins are perpendicular to each other. At the same time, however, the exchange energy (detailed in section 16.2.2) in a ferromagnetic material is minimized when all the magnetic spins are aligned with each other: skyrmions are the result of the competition of these two mechanisms and of the minimization of the energy inside the system, like explained in section 16.2.2. The Néel skyrmion is the configuration minimizing the energy when $\boldsymbol{D}_{12} \perp \boldsymbol{R}_{12}$, the Bloch skyrmion instead minimizes the energy for $\boldsymbol{D}_{12} \parallel \boldsymbol{R}_{12}$ [177], like shown in figure 16.2c, where $\boldsymbol{R}_{12}$ is the vector joining spin $\boldsymbol{S}_1$ with spin $\boldsymbol{S}_2$.

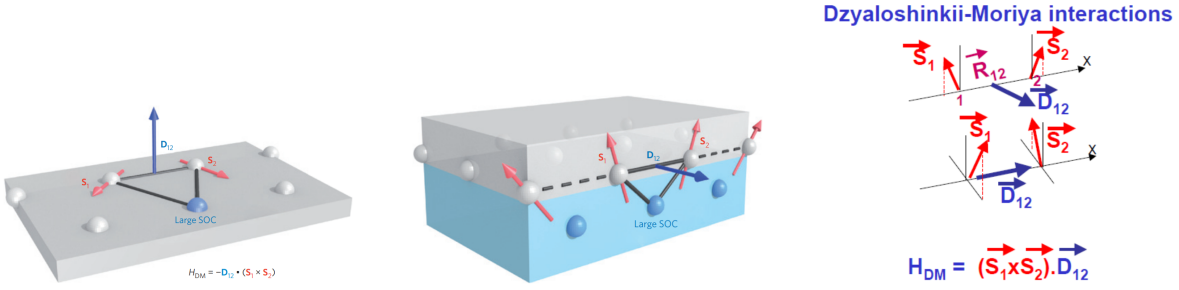

(a) (b) (c)

Figure 16.2: (a) DMI vector generated by the interaction of two atomic spins with an atom with strong SOC (blue) in a ultrathin magnetic film. (b) DMI vector generated at the interface between a FM thin layer (grey) and a metal with strong SOC (blue). Figures extracted from [177]. (c) The top configuration gives rise to a Néel skyrmion, the bottom configuration to a Bloch skyrmion. Figure extracted from [178].

The asymmetry due to the presence of the non-magnetic atom in the lattice or at the interface with the bottom metal layer is needed because, in this way, the DMI cannot be compensated by the DMI coming from a symmetric triangle [177].

The magnitude and sign of the vector $\boldsymbol{D}_{12}$ depend on the materials involved, on the interface and on the strength of the spin-orbit coupling of the non-magnetic atom, and has an important role in determining the size of the resulting skyrmion, like detailed in section 16.2.6.

Spin-orbit coupling While considering the orbiting motion of the electron around the proton from the point of view of the electron, the same atomic system can be seen like the proton orbiting around the electron. Due to Ampere's law, this positive charge motion generates a magnetic field, which of course will interact with the magnetic moment (proportional to the spin) of the electron: this phenomenon is known as spin-orbit coupling (SOC).

Vorticity number

Another parameter useful in characterizing the skyrmion topological structure is the vorticity number m, defined as the winding number of the spin configurations projected into the xy-plane [173]. The winding number of an oriented curve counts how many times the curve encircles a well defined point in a plane in the counterclockwise direction. Describing this curve in polar coordinates (r, θ), the winding number can be computed like

$$W = \frac{\theta(end) - \theta(start)}{2\pi} \tag{16.6}$$

Since the initial and the final position, when following the full path of the curve around the point, must be coincident, then the two θ angles must differ by an integer multiple of 2π: this implies that the winding number is either a positive or negative integer.

In the specific case of magnetic topological structures, the winding number can be defined also like the total variation of the magnetization angle when moving counterclockwise along a circle traced around the centre of the structure, divided by 2π [179, 178]. Each value of the magnetization angle can be mapped into a point on the circle, which in this context is formally called order-parameter space. According to the oriented movement along the order-parameter space, the winding number is computed.

The skyrmion number can be computed also through the vorticity number, using the relation

$$Q = \frac{m}{2}\left[\lim_{r\to\infty} cos(\theta(r)) - cos(\theta(0))\right] \tag{16.7}$$

which can be recognized simply like a rewriting of equation 16.3, where $m = \frac{1}{2\pi}\phi(\varphi)|_{\varphi=0}^{\varphi=2\pi}$ is the vorticity that has just been defined. Observing 16.2 it can be deduced that $cos(\theta(r))$ is the z-component of the unit vector representing the local magnetic moment. So, the skyrmion number depends both on the vorticity and on the direction of the magnetization at the tail and at the core of the skyrmion. Is important to notice that, in a skyrmion, the direction of the core is always opposite to the direction of the tail, which is the same of the background magnetization present in the material.

Helicity number and polarity

The third parameter needed to describe the skyrmion structure is the helicity number γ, determined uniquely by the type of DMI that intervenes in the energetic competition. A Bloch skyrmion (bulk DMI) is characterized by $\gamma = \frac{\pi}{2}$ or $\gamma = \frac{3\pi}{2}$, while a Néel skyrmion (interfacial DMI) corresponds to $\gamma = 0$ or $\gamma = \pi$. It's important to notice that the helicity does not contribute to the topological number.

Finally, the polarity p describes the orientation of the centre with respect to the z-direction: if $p = 1$ the magnetization of the core points in the positive z-direction, vice versa if $p = -1$.

Meaning of the helicity number

Looking back at equation 16.4, which expresses the in-plane magnetization angle ϕ, it can be recognized now that m is the vorticity number and γ the helicity number, while φ is the azimuthal angle of the polar coordinates system, describing the position of a point in the xy-plane. For both Bloch and Néel skyrmions the vorticity number is equal to 1, like

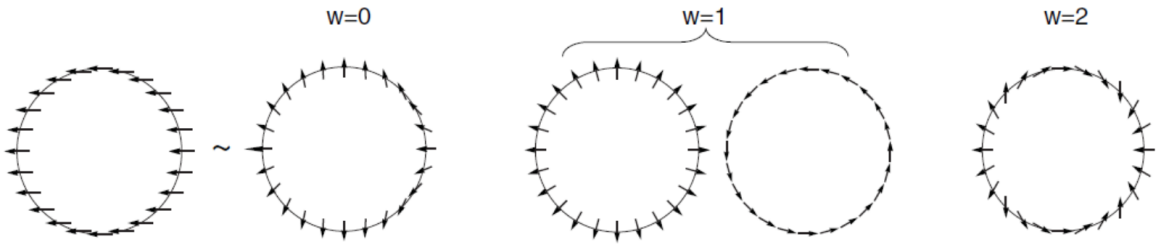

(a)

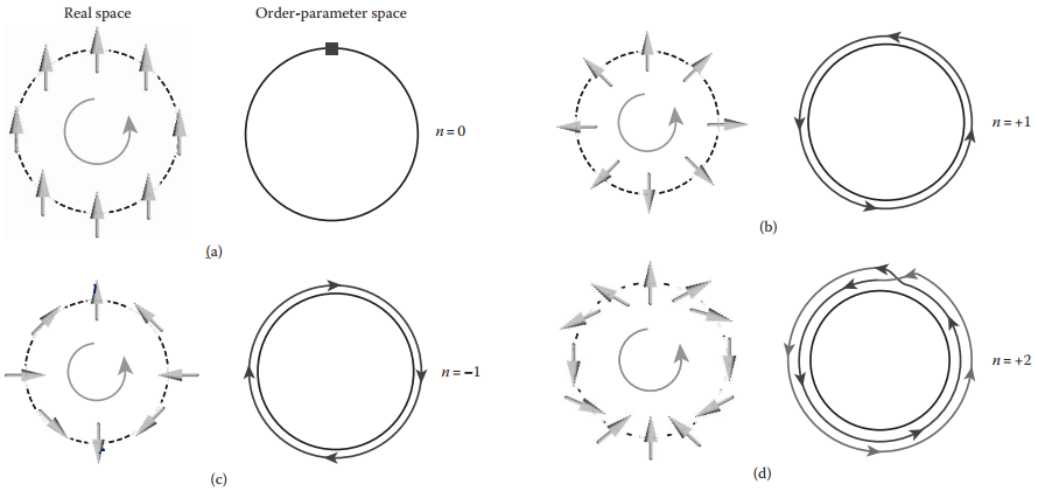

(b)

Figure 16.3: (a) Examples of computation of the winding number for different spin configurations. The two cases with $W = 1$ can be assimilated to a Néel skyrmion (left) and to a Bloch skyrmion (right). Figure adapted from [180]. (b) Other examples of computation of the winding number, including the mapping on the order-parameter space. Figure extracted from [181].

it can be observed comparing figure 16.3a with the two structures shown in figure 16.1. In section 16.2.1 it has been said that for a Bloch skyrmion $\gamma = \frac{\pi}{2}$ or $\gamma = \frac{3\pi}{2}$, while for a Néel skyrmion $\gamma = 0$ or $\gamma = \pi$. Summing up:

Néel:

$$\begin{cases} \phi = \varphi \\ \phi = \varphi + \pi \end{cases} \tag{16.8}$$

Bloch:

$$\begin{cases} \phi = \varphi + \frac{\pi}{2} \\ \phi = \varphi + \frac{3\pi}{2} \end{cases} \tag{16.9}$$

From these expressions is easy to predict one of the experimental results reported in section 16.2.1: if $\gamma = 0$ the in-plane magnetization is aligned with the unit vector $\hat{\varphi}$ and the spins will be out-going, while if $\gamma = \pi$ the magnetization is antiparallel with respect to $\hat{\varphi}$ and the spins will be in-going. Similarly, if $\gamma = \frac{\pi}{2}$ the in-plane magnetization has a 90 phase difference with respect to $\hat{\varphi}$ and the spins of the Bloch skyrmion will rotate in a counterclockwise direction, while if $\gamma = \frac{3\pi}{2}$ the phase difference is by -90 and the spins rotate in a clockwise direction. The confirmation to these statements can be easily found in the top half of figure 16.4.

Topological protection

The topological charge of skyrmions is always an integer equal to $+1$, at least if this particle is in a region larger than its diameter. For this reason, even if its spin texture may

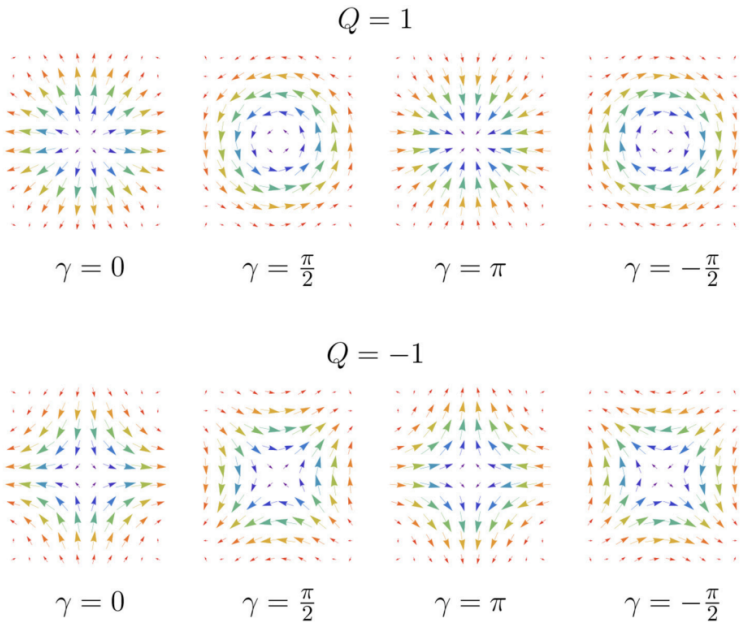

Figure 16.4: Magnetization configuration of skyrmions ($Q = 1$) and antiskyrmions ($Q = -1$) with fixed polarity ($p = 1$) and varying helicity γ. The length and direction of the arrows represents the in-plane magnetization component, while the colour represents the magnitude of the out-of-plane component: blue stands for $+z$, red for $-z$. Figure extracted from [182].

be deformed (for example due to the presence of impurities in the material), the Pontryagin number doesn't change and as a result the skyrmion can be neither destroyed nor separated into pieces: it is said to be topologically protected. This protection fails only when the skyrmion touches the sample edges, because in this condition the topological charge is allowed to change continuously: in this condition the skyrmion can be annihilated and the information it carries gets lost.

Practical examples

Some examples, which show well the practical meaning of all the parameters presented up to this point, can be found in [183], where the results presented in [171] are exploited.

In [171] is demonstrated the possibility to convert in a reversible way a domain wall (DW) pair into a skyrmion and vice versa by using a junction made of a narrow nanowire ($W < 2R$, where W is the width of the nanotrack and R the skyrmion radius) connected to a wide nanowire ($W > 2R$). Like explained in [183], when a topological object, like a skyrmion, that previously was in a wide region enters a narrow region, it loses its topological numbers, like the skyrmion number and the helicity, and becomes a DW pair, which is a non-topological object ($Q = 0$); when it is ejected again into a new wide region, it is assigned new topological numbers to adjust the physical properties of the new region, which may be different from the properties of the former wide region. Skyrmions, as mentioned, are topologically protected only when the sample is enough large, and this protection is broken when they touch an edge: this is what happens when the skyrmion enters the narrow junction.

Another result of [171] that has been used in [183] (like explained in section 16.3.1) is shown in figure 16.5b (g-l frames): using the same junction but reducing the current density needed to move the domain wall, the particle obtained is not a skyrmion, but a meron. A meron is a different type of topological object, very similar to a skyrmion, but with $|Q| = \frac{1}{2}$: this means that its spins can wrap only the north pole or the south pole of the unit sphere, like shown in figure 16.6. Its peculiarity is to remain attached to the sample edges even during

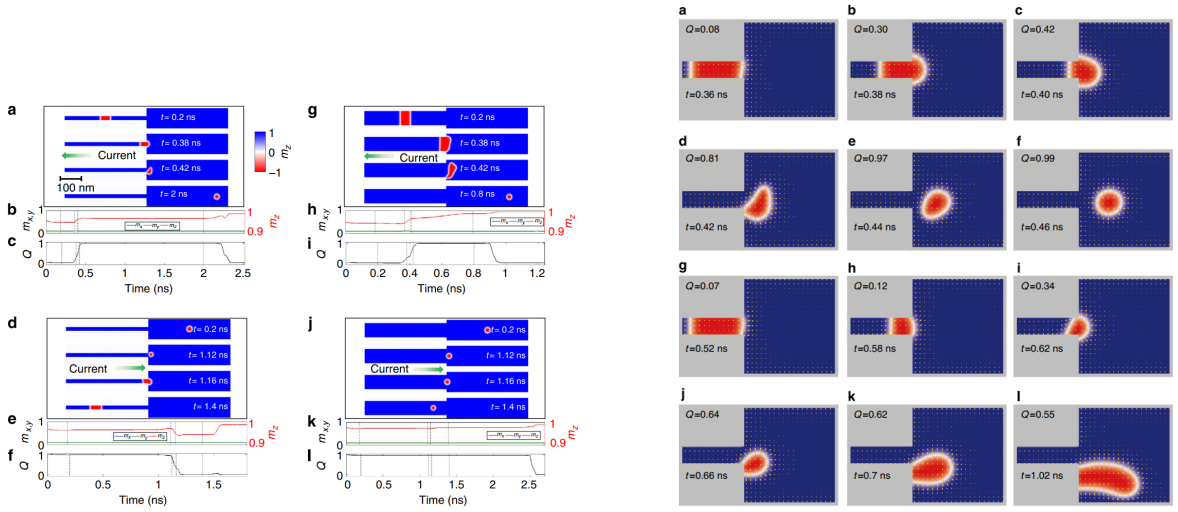

(a) (b)

Figure 16.5: (a) Reversible conversion DW pair→skyrmion (a-c) and vice versa (d-f). g-l: when the size of the narrow part of the junction increases the DW pair is still converted into a skyrmion, but with more fluctuations in the radius and the shape (g-i); the skyrmion instead cannot be converted back into a DW pair (j-l). The middle plots show the time variation of the components of the magnetization; the bottom plots show the time variation of the skyrmion number. (b) Detail on the conversion from DW pair. a-f: when the current density is high enough the right DW pins at the junction, while the remaining part of the DW pair continues to move: as a result, the DW is deformed into a curve shape. When the other DW reaches the junction the skyrmion is formed. g-l: when the current density is reduced a meron is formed; the meron remains in contact with the nanotrack edge. Figures extracted from [171].

its movement.

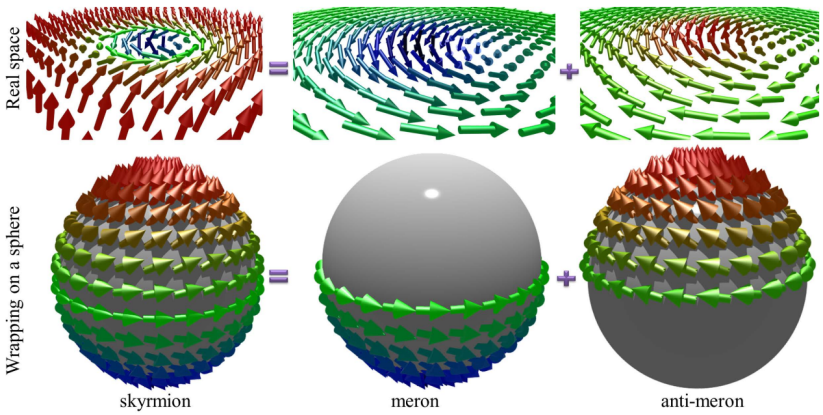

Figure 16.6: Splitting a skyrmion in two halves, a meron and an anti-meron are obtained. A skyrmion covers the entire unit sphere, while a meron covers only half of it: so the topological charge of a meron is $\pm\frac{1}{2}$. Figure extracted from [184].

The first part of [183] verifies how different physical properties of the materials on the left and on the right side of a narrow nanotrack influence the assignment of new topological numbers to the skyrmion ejected from the junction, and allows to understand the practical meaning that these numbers have when considering the skyrmion's structure.

In figure 16.7a the parameter that changes from left to right is the sign of the DMI, which is positive on the left side and negative on the right side. As mentioned in section 16.2.1, the helicity is uniquely determined by the DMI. Since the skyrmions considered in this article

are only of Néel type, the helicity can be either $\gamma = 0$ or $\gamma = \pi$. On the left side the triplet of numbers (Q, m, γ) (topological charge, vorticity and helicity; this notation will be used from now on) is $(1, 1, 0)$, whereas on the right side it is $(1, 1, \pi)$ (while in the junction it becomes $(0, 0, 0)$). Observing the picture, it can be noticed that the direction of the core has remained $-z$, while the spins from out-going have become in-going. So the helicity, like anticipated in section 16.2.1, determines the radial direction of the spins: when $\gamma = 0$ the spins point outwards, when $\gamma = \pi$ they point inwards.

In figure 16.7b the sign of the DMI is the same in both regions, while the direction of the background magnetization is reversed from left to right. According to equation 16.7, the topological charge depends both on the vorticity and on the direction of the spins at the core and at the tail of the skyrmion, and the spin direction at the tail is always the same as the background magnetization. Reversing the background magnetization then the second factor of 16.7 is reversed (from the picture it can be observed that the core now points in the $+z$ direction and the tail in the $-z$ direction), while the vorticity remains unchanged: as a consequence the topological number becomes $Q = -1$ and the magnetic texture obtained is called antiskyrmion. Moreover, in this condition also the helicity changes from $\gamma = 0$ to $\gamma = \pi$ to minimize the energy of the system. So, the topological numbers change as $(1, 1, 0) \rightarrow (-1, 1, \pi)$.

Finally, in 16.7c both the sign of the DMI and the background magnetization are reversed from left to right. Combining the two effects discussed above, then, the skyrmion becomes an antiskyrmion due to the background reversal, while the helicity remains unchanged and so the spin direction remains out-going. The change of the topological numbers is $(1, 1, 0) \rightarrow (-1, 1, 0)$

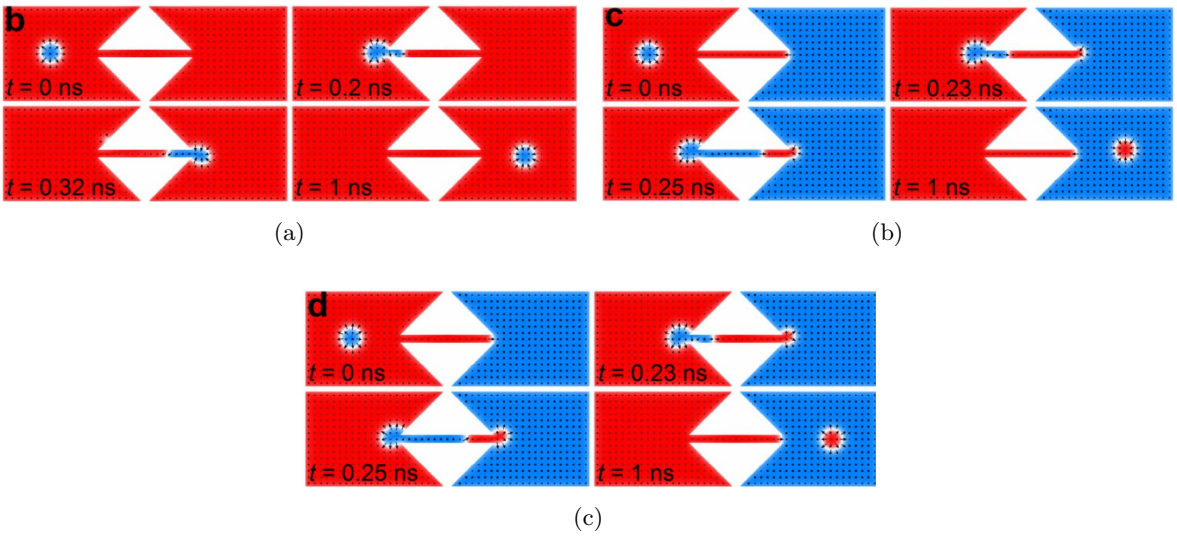

Figure 16.7: Skyrmion→DW pair→skyrmion conversion. Red(blue) is the $+z(-z)$ direction of the magnetization. (a) Reversing the sign of the DMI $(1, 1, 0) \rightarrow (1, 1, \pi)$ (b) Reversing the background magnetization $(1, 1, 0) \rightarrow (-1, 1, \pi)$ (c) Reversing both DMI and background magnetization $(1, 1, 0) \rightarrow (-1, 1, 0)$. Figures extracted from [183].

Skyrmions and antiskyrmions Like mentioned, antiskyrmions are spin textures very similar to skyrmions, but with topological charge equal to -1 [2]. They can still be mapped on a unit sphere, like shown in figure 16.8. Some examples of antiskyrmions can be found

[2]Some attention must be paid in the definition of antiskyrmions. Many examples in literature define as antiskyrmions those particles with $Q = -1$, while other authors consider antiskyrmions those particles that have $m = -1$, usually regardless of the topological charge. This inconsistency is evident when reading [183] and its supplementary information, [185], [176], [186] and [187]. In this document we conform ourselves to the first definition.

also in the bottom half of figure 16.4, where is shown the disposition of the in-plane magnetization by varying the helicity.

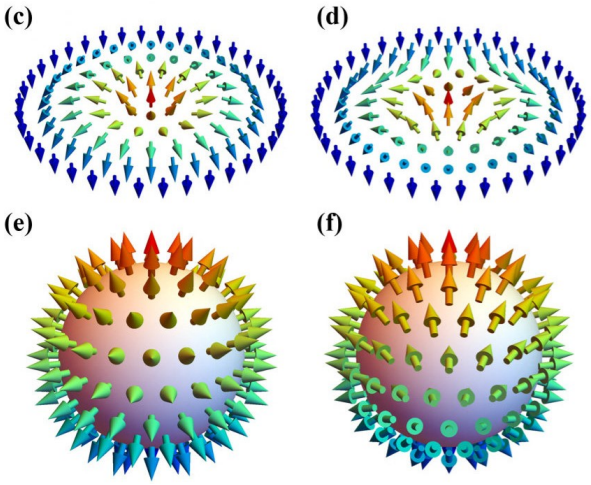

Figure 16.8: Mapping of a skyrmion $(1, 1, 0)$ and of an antiskyrmion $(-1, -1, 0)$ with $p = 1$ on the unit sphere (order-parameter space). Figure extracted from [188].

According to the examples just discussed and to the theory exposed up to now, the skyrmion and antiskyrmion main figures are summed up in table 16.1 (if the background magnetization is along $+z$, then $\lim_{r\to\infty} cos(\theta(r)) - cos(\theta(0)) = 2$, while if it is along $-z$ $\lim_{r\to\infty} cos(\theta(r)) - cos(\theta(0)) = -2$).

Table 16.1: Summary of topological numbers for skyrmions and antiskyrmions

	BACKGROUND: $+z$	BACKGROUND: $-z$
SKYRMION	$Q = 1$, $m = 1$	$Q = 1$, $m = -1$
ANTISKYRMION	$Q = -1$, $m = -1$	$Q = -1$, $m = 1$

The confirmation to this table can be found in the supplementary information of [183], where the figure 16.9 is shown.

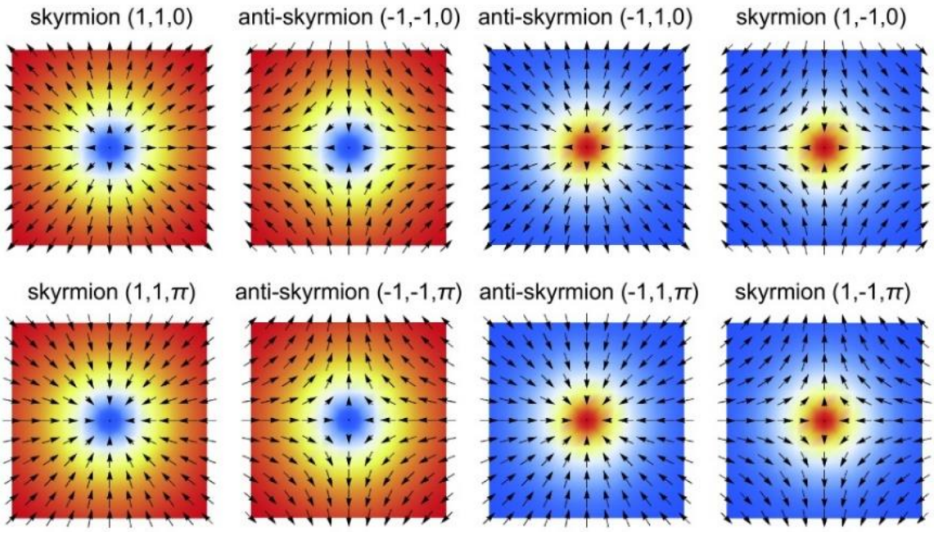

Figure 16.9: Examples of skyrmions and antiskyrmions by varying vorticity, helicity and background magnetization (and so polarization). Each triplet of numbers reports (Q, m, γ); red(blue) denotes the $+z(-z)$ direction of the magnetization. Figure extracted from the supplementary information of [183].

16.2.2 Micromagnetic model

The static properties of skyrmions can be studied theoretically with the help of the micromagnetic model, a theory used to describe the magnetization of a material from the nanoscale to the microscale. This length scale is large enough for avoiding the use of all the mathematical operators required by quantum mechanics, but at the same time it is small enough to carefully describe magnetization patterns like skyrmions or domain walls, among the others [174]. This theory allows to model the relationship between the spatial distribution of the effective magnetic field $\boldsymbol{H}_{eff}$, determined by the energetic contributions competing in the system, and the magnetization vector field $\boldsymbol{M}$ [175]. The key equation on which the micromagnetic model is based is the Landau-Lifshitz-Gilbert (LLG) equation.

LLG equation

This equation relates the effective field $\boldsymbol{H}_{eff}$ to the time evolution of the magnetization vector field $\boldsymbol{M}$. It is a torque equation, and its expression is

$$\frac{d\boldsymbol{M}}{dt} = -\gamma_0 \boldsymbol{M} \times \boldsymbol{H}_{eff} + \alpha \left(\boldsymbol{M} \times \frac{d\boldsymbol{M}}{dt} \right) \tag{16.10}$$

where $\boldsymbol{M}$ is the magnetization, $\boldsymbol{H}_{eff}$ is the effective magnetic field (not necessarily an external magnetic field, it can be also the field experienced locally by the magnetic moments inside the material), γ_0 is the gyromagnetic ratio and α the Gilbert damping coefficient. The first term describes the precession movement that the magnetic moments perform around the effective magnetic field when they are not fully aligned with it: this is known as Larmor precession. While performing this precession movement the magnetization also relaxes along the field line, finally becoming aligned with it, in order to minimize the energy of the system: this is modelled by the second term, containing the Gilbert damping.

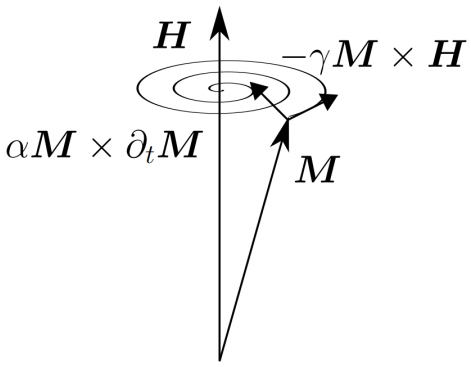

Figure 16.10: Sketch of the Larmor precession performed by a magnetic moment around a field line of $\boldsymbol{H}_{eff}$, and of the Gilbert damping contribution which, determining a spiraling motion around the field line, eventually makes the magnetic moment align with it. Figure extracted from [174].

It can be demonstrated [174] that only the direction of the magnetization changes with time, while its magnitude remains constantly equal to the saturation magnetization M_S.

The direction of the effective magnetic field is the direction in which the magnetization will have the minimum of the micromagnetic energy: therefore the effective field can be written in terms of the micromagnetic energy [174] as

$$\boldsymbol{H}_{eff} = -\frac{1}{\mu_0} \frac{\partial E_V}{\partial \boldsymbol{M}} \tag{16.11}$$

where E_V is the micromagnetic energy density.

Micromagnetic energy density The contributions to the micromagnetic energy come from the exchange energy, the Zeeman energy, the demagnetizing field energy, the anisotropy energy and the DMI. Also other terms could be considered, like the RKKY (Ruderman-Kittel-Kasuya-Yosida) interaction, but when considering skyrmions in most of the cases they are neglected, so they won't be considered here.

Exchange energy The exchange interaction (sometimes also Heisenberg interaction) is the phenomenon which makes the magnetic moments inside a ferromagnetic material align with each other, allowing them to generate a magnetic field observable from the external. If the sign of the exchange constant J present in the Hamiltonian of this interaction is positive, then the material is a ferromagnetic material and the spins align parallel to each other; if the sign of J is negative, instead, the material is an antiferromagnet and the spins arrange antiparallel to each other.

The energy density of the exchange interaction is [173]

$$E_V = A[\nabla \boldsymbol{m}]^2 \tag{16.12}$$

where A is the exchange constant.

Zeeman energy When applying an external magnetic field, the magnetic moments tend to align with its field lines: this is due to the Zeeman interaction. Its energy density is [171]

$$E_V = -\mu_0 \boldsymbol{M} \cdot \boldsymbol{H}_{ext} \tag{16.13}$$

where $\boldsymbol{H}_{ext}$ is the magnetic field applied externally.

Demagnetizing field energy The magnetic induction is $\boldsymbol{B} = \mu_0(\boldsymbol{H} + \boldsymbol{M})$, where $\boldsymbol{H}$ is the magnetic field and $\boldsymbol{M}$ is the magnetization. Since $\boldsymbol{M} = \chi \boldsymbol{H}$, where $\chi = \mu_r - 1$ is the susceptibility, then $\boldsymbol{B} = \mu_0(1+\chi)\boldsymbol{H} = \mu_0\mu_r\boldsymbol{H}$.

Inside a magnetic material $\boldsymbol{H}$ is directed oppositely with respect to $\boldsymbol{M}$, like shown in figure 16.11. For this reason, when considering the value of $\boldsymbol{B}$ inside the material, $\boldsymbol{H}$ contributes by reducing this value. This is why it is called demagnetizing field (while it is named stray field outside the material).

The energy density associated to the demagnetizing field $\boldsymbol{H}_d$ is

$$E_V = -\frac{\mu_0}{2} \boldsymbol{M} \cdot \boldsymbol{H}_d(\boldsymbol{M}) \tag{16.14}$$

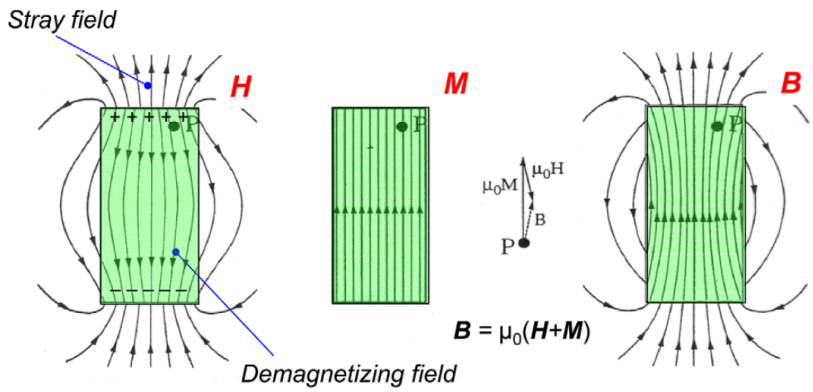

Figure 16.11: Depiction of the magnetic field $\boldsymbol{H}$, the magnetization $\boldsymbol{M}$ and the magnetic induction $\boldsymbol{B}$ inside a magnetic material. The magnetic field $\boldsymbol{H}$ takes the name of demagnetizing field inside the material and of stray field outside it. Figure adapted from [189].

Anisotropy energy The magnetocrystalline anisotropy is the property of some magnetic materials which makes some directions for the magnetization more energetically favourable than others; it is is linked to the spin-orbit coupling and to the atomic structure of the material. As a result, some directions may be easier to be magnetized than others. In particular, when this energetically favourable direction (called easy-axis) is perpendicular to the material, then we're dealing with the perpendicular magnetic anisotropy (PMA). The PMA can be found in some layered ultrathin films, like for example Pd/Co [174].

The energy density for the PMA is [171]

$$E_V = K_u[1 - (\boldsymbol{m} \cdot \hat{\boldsymbol{z}})^2] \tag{16.15}$$

where K_u is the uniaxial anisotropy constant and the unit vector $\hat{\boldsymbol{z}}$ represents the easy-axis.

In layered structures of ultrathin films, where the surface effects are not negligible, a form of PMA arises at the interface due to exchange interactions between some of the electronic orbitals of the materials involved. It has been discovered that the strength of this PMA can be modified by applying an external electric field: this field modifies the occupation of the orbitals and so is able to affect the exchange interactions [174].

As a result, if K_u is the PMA constant, the voltage controlled PMA will induce a variation $\Delta K_{uv} E$ dependent on the electric field applied, so that the expression of the total PMA constant is [190]

$$K_{uv} = K_u + \Delta K_{uv} E \tag{16.16}$$

Of course, according to the sign of the z-component of the electric field, the PMA can either increase or decrease with respect to its bias level K_u.

DMI energy The bulk DMI energy density is [174]

$$E_V^{(bulk)} = D\boldsymbol{m} \cdot (\nabla \times \boldsymbol{m}) \tag{16.17}$$

The interfacial DMI energy density is instead (assuming to consider an ultrathin film, where $\frac{\partial \boldsymbol{m}}{\partial z} = 0$) [171]

$$E_V^{(interfacial)} = D[m_z(\nabla \cdot \boldsymbol{m}) - (\boldsymbol{m} \cdot \nabla)m_z] \tag{16.18}$$

Summing all these energy density contributions together the total energy density $E_{V,TOT}$ is obtained. The total energy of a system of volume V is

$$E_{TOT} = \int_V E_{V,TOT} dV \tag{16.19}$$

The spin configuration then is found by minimizing the total energy E_{TOT} [178].

16.2.3 Motion

There are many possibilities both for nucleating and for moving skyrmions: some of them consist in applying an external magnetic field or temperature gradients. However, is clear than none of these options can be easily used inside an integrated circuit based on skyrmions, where it would be preferable to use current-based mechanisms instead.

When it comes to current, there are mainly two mechanisms available, both exploiting the spin-transfer-torque phenomenon.

Spin Transfer Torque (STT)

When a charge current is injected into a material with a certain magnetization pattern, the spin of each conduction electron will interact with the magnetization vector field. This interaction leads to the formation of two torques: one tends to align the spin of the electron with the direction of the local magnetic moment, while the other, equal and opposite due to the conservation of the total angular momentum, at the same time tries to align the local magnetization with the direction of the electron spin. This is the spin-transfer-torque (STT) mechanism.

The STT contributes in modifying the orientation of the local magnetic moment: for this reason it can be included in the LLG equation. Since the current flows inside the ferromagnet along the in-plane direction, this torque is indicated as $\boldsymbol{\tau}_{IP}$. It is composed by two contributions. The first is the adiabatic STT, where adiabatic refers to the assumption that the spin of the electron passing through the magnetic material relaxes fast enough so that is always aligns with the local magnetic moment [174]. The second term of $\boldsymbol{\tau}_{IP}$ has been added phenomenologically to explain unexpected experimental results and it is the non-adiabatic STT: the adiabatic approximation fails when the magnetization pattern changes so quickly in space that the electrons are not fast enough to align their spin with the local magnetic moment.

The expression of $\boldsymbol{\tau}_{IP}$ is

$$\boldsymbol{\tau}_{IP} = \frac{\gamma_0 \hbar P}{2\mu_0 e M_S}(\boldsymbol{j}\cdot\nabla)\boldsymbol{m} - \frac{\gamma_0 \hbar P}{2\mu_0 e M_S}\beta \boldsymbol{m}\times(\boldsymbol{j}\cdot\nabla)\boldsymbol{m} \tag{16.20}$$

where the first term is the adiabatic STT and the second term is the non-adiabatic STT. Here γ_0 is the gyromagnetic ratio, P is the polarization coefficient of the in-plane electrical current, e is the electron charge, M_S is the saturation magnetization, $\boldsymbol{j}$ is the in-plane electrical current flowing through the ferromagnet, $\boldsymbol{m}$ is the normalized magnetization, and β is the non-adiabaticity factor, quantifying the relative strength of the non-adiabatic STT with respect to the adiabatic STT.

The term $\boldsymbol{\tau}_{IP}$ is added to the LLG equation when a current is flowing along the in-plane direction of a ferromagnet. The geometry used for the skyrmion motion that uses this effect is then called current-in-plane (CIP) geometry and is shown in figure 16.12a.

As mentioned, the spins of the conduction electrons exert a torque on the spin texture of the skyrmion; at the same time, the spin texture exerts a torque equal in magnitude and opposite in sign on the spin of the conduction electrons. As a result, the magnetic moments of the skyrmion subjected to the torque will rotate, allowing the movement of the particle, and at the same time the conduction electrons are deflected from the original direction of the current flux: this is known as topological Hall effect, and the reason behind this is the Berry phase.

The Berry phase is the rotation that a vector experiences while moving along a closed path on a curved surface. The skyrmion, as already mentioned, is a 2D structure, but the magnetic moments that constitute it can be organized on a unit sphere: assuming that the conduction electrons are able to follow exactly the orientation of the local magnetic moment of the skyrmion (adiabatic approximation), while crossing the particle they gain a Berry phase. This Berry phase is the reason behind the emergent magnetic field experienced by the conduction electrons. This field will make the conduction electrons experience a Lorentz force

$$F = q(\boldsymbol{E} + \boldsymbol{v}\times\boldsymbol{B}) \tag{16.21}$$

If the skyrmion texture is localized in the xy plane, the emergent field points along the z-axis, so the Lorentz force belongs to the xy plane and is perpendicular to the motion of the conduction electrons, making them deflect from their original direction [174].

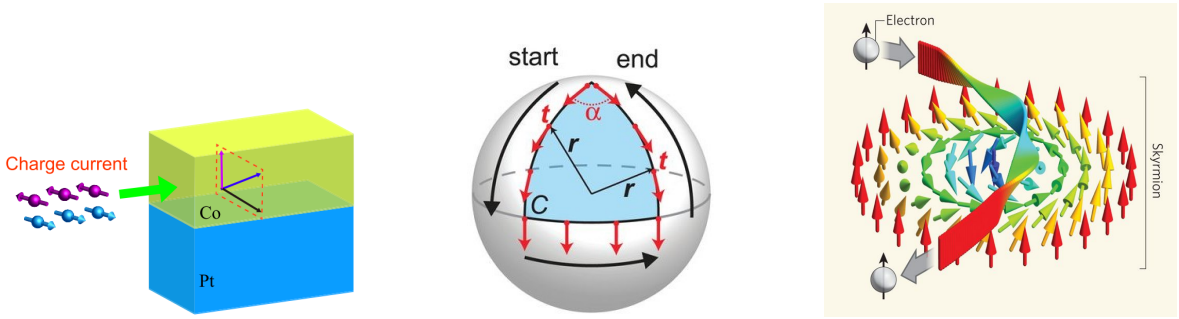

(a) (b) (c)

Figure 16.12: (a) CIP configuration: a spin-polarized current flows directly inside the FM layer (yellow) deposited above the HM layer (blue). Figure extracted from [173]. (b) Sketch of the Berry phase α acquired by a vector t (depicted in red) in the movement along the oriented curve on the curved surface of a sphere. Figure extracted from [191]. (c) Effect of the torque exerted by the skyrmion texture on the spin of the conduction electron and depiction of the topological Hall effect. Figure extracted from [192].

Spin Hall Effect (SHE)

The spin Hall effect is a phenomenon that originates in spin-Hall devices, where a ferromagnetic (FM) thin film is deposited above a heavy metal (HM) substrate, like shown in figure 16.13. Here the electrical current is injected inside the HM layer. Due to spin-dependent scattering mechanisms (which include also SOC [193]), the electrons will experience a deflection perpendicular to their flow direction and to the orientation of their spin. As a result, the SHE leads to an accumulation of charges at the sides of the wire, and each side is populated by electrons with a well defined spin orientation. For example, if the current flows in the $+x$-direction and if the anomalous velocity acquired by the electrons is directed along the $+z$-axis, making them accumulate at the top surface of the wire, their spin orientation will be along the $+y$-axis. Moreover, this spin current flowing in the z-direction and polarized along the y-direction, can be collected by the FM thin film deposited above the HM substrate. This transverse spin current then will interact with the magnetization of the HM layer, again through the STT mechanism [194, 193].

Since this time the current that interacts with the magnetization is directed perpendicularly to the film plane, this configuration is called current-perpendicular-to-plane (CPP) geometry.

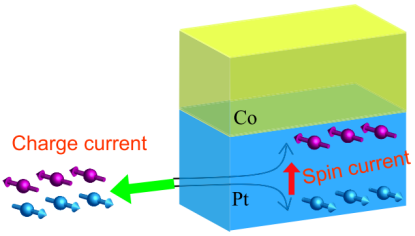

Figure 16.13: CPP configuration: an electrical current flows inside the HM layer (blue); the spin-Hall effect determines the creation of a spin-polarized current directed in the vertical direction that is collected by the FM layer (yellow) deposited above. Figure extracted from [173]

The expression of the torque $\boldsymbol{\tau}_{SHE}$ associated to this phenomenon is

$$\boldsymbol{\tau}_{SHE} = -\frac{\gamma_0 \hbar j \theta_{sh}}{2\mu_0 e M_S t_f} \boldsymbol{m} \times (\boldsymbol{m} \times \boldsymbol{p}) \tag{16.22}$$

where t_f is the thickness of the FM layer, $\boldsymbol{p}$ is the spin-current polarization direction ($+y$ in the example reported above), j is the current density and θ_{sh} is the spin Hall angle. The

spin Hall angle measures the efficiency of the conversion from charge current J_{ch} to spin current J_s and depends on material parameters [195]. Its expression is

$$\theta_{sh} = \frac{J_s}{J_{ch}} \tag{16.23}$$

Thiele equation and skyrmion Hall effect

When assuming that the skyrmion moves without deforming its texture, the time-dependent evolution of the magnetization pattern can be written like

$$\boldsymbol{M}(\boldsymbol{r}, t) = \boldsymbol{M}_0[\boldsymbol{r} - \boldsymbol{R}(t)] \tag{16.24}$$

where $\boldsymbol{M}_0$ is the initial configuration of the skyrmion when located in the axis origin, and $\boldsymbol{R}(t)$ is the position of the skyrmion's centre of mass at time t [196]. Thiele recognized that, in this case, the time derivative of the magnetization can be written as

$$\frac{d\boldsymbol{M}}{dt} = \frac{\partial \boldsymbol{R}}{\partial t}\frac{\partial \boldsymbol{M}}{\partial \boldsymbol{R}} = \frac{\partial \boldsymbol{R}}{\partial t}\left(-\frac{\partial \boldsymbol{M}}{\partial \boldsymbol{r}}\right) = -(\boldsymbol{v}\cdot\nabla)\boldsymbol{M} \tag{16.25}$$

Substituting the time derivatives that appear in the LLG equation with the expression 16.25, and converting the LLG equation into a force density equation, like detailed in [196], the LLG equation can be rewritten into the Thiele equation [174]. Its expression for the CIP configuration is

$$\boldsymbol{G}\times(\boldsymbol{v}_s - \boldsymbol{v}_d) + \mathcal{D}(\beta\boldsymbol{v}_s - \alpha\boldsymbol{v}_d) + \nabla\boldsymbol{V}(\boldsymbol{r}) = 0 \tag{16.26}$$

Here $\boldsymbol{G} = (0, 0, G) = (0, 0, 4\pi Q)$ is the gyromagnetic coupling vector; $\boldsymbol{v}_d$ is the drift velocity of the skyrmion core; $\boldsymbol{v}_s$ is the velocity of the conduction electrons, where $\boldsymbol{v}_s = -\frac{Pa^3}{2eM_S}\boldsymbol{j}$ (P is the spin polarization of the electrical current and a is the lattice constant); $\mathcal{D}$ is the dissipative force tensor, where $\mathcal{D} = \begin{pmatrix} \mathcal{D}_{xx} & 0 \\ 0 & \mathcal{D}_{yy} \end{pmatrix}$ and $\mathcal{D}_{xx} = \mathcal{D}_{yy} = \int_{unit\ cell}(\partial_i\boldsymbol{m}\cdot\partial_j\boldsymbol{m})dxdy$ for both skyrmions and antiskyrmions; β is the non-adiabaticity factor; α is the Gilbert damping; $\nabla\boldsymbol{V}(\boldsymbol{r})$ represents the repulsion forces due to process impurities, the nanotrack edges or due to skyrmion-skyrmion repulsion.

Considering a skyrmion that moves far away from the edges along the x-axis (so, $\boldsymbol{v}_{s,x} \neq 0$, $\boldsymbol{v}_{s,y} = 0$ and $V = 0$), it can be found that [197]

$$\begin{cases} v_{d,x} = \left(\frac{\beta}{\alpha} + \frac{G^2}{\alpha}\frac{\alpha-\beta}{G^2+(\alpha\mathcal{D})^2}\right)v_{s,x} \\ v_{d,y} = \left(\mathcal{D}G\frac{\alpha-\beta}{G^2+(\alpha\mathcal{D})^2}\right)v_{s,x} \end{cases} \tag{16.27}$$

The Thiele equation for the CPP configuration is

$$\boldsymbol{G}\times\boldsymbol{v}_d - \alpha\mathcal{D}\cdot\boldsymbol{v}_d + 4\pi\mathcal{B}\cdot\boldsymbol{J}_{HM} + \nabla\boldsymbol{V}(\boldsymbol{r}) = 0 \tag{16.28}$$

Here $\mathcal{B} = \begin{pmatrix} \mathcal{B}_{xx} & 0 \\ 0 & \mathcal{B}_{yy} \end{pmatrix}$, where $\mathcal{B}_{xx} = \mathcal{B}_{yy}$ for skyrmions and $\mathcal{B}_{xx} = -\mathcal{B}_{yy}$ for antiskyrmions, is the tensor linked to the STT effect quantifying the efficiency of the spin Hall-spin torque over the spin texture of the skyrmion [198], and it can be determined starting from the spin configuration; $\boldsymbol{J}_{HM} = \frac{\boldsymbol{J}_s}{\theta_{sh}}$ is the electrical current density flowing in the HM, where $\boldsymbol{J}_s$ is the spin current density and θ_{sh} is the spin Hall angle of the HM [173, 198].

From the Thiele equation of the CPP configuration it can be proven that the velocity components of both skyrmion and antiskyrmion are [199, 200]

$$\begin{cases} v_{d,x} = \frac{-j\alpha\mathcal{D}\mathcal{B}_{xx}}{(\alpha\mathcal{D})^2+Q^2} \\ v_{d,y} = \frac{jQ\mathcal{B}_{xx}}{(\alpha\mathcal{D})^2+Q^2} \end{cases} \tag{16.29}$$

It has been demonstrated in [173] that the driving efficiency of the CPP configuration is much higher with respect to the efficiency of the CIP configuration: applying the same current density, the skyrmion velocity obtained with the CPP geometry is higher than the velocity obtained with the CIP geometry.

The drift velocity $\boldsymbol{v}_d$ for both geometries includes not only a component $v_{d,x}$ parallel to the direction of the driving current, but also a transverse component $v_{d,y}$ perpendicular to it that drives the skyrmion towards the track edges. The term inside the Thiele equation that gives rise to this component is the Magnus force $\boldsymbol{G} \times \boldsymbol{v}_d$. Since $\boldsymbol{G} = (0, 0, 4\pi Q)$, the reason why the skyrmion is subjected to this force is that it carries a topological charge different from 0.

With both configurations, increasing the current density also the skyrmion velocity will increase. However, there is a limit current density above which the repulsive forces from the edges of the nanotrack, due to the tilting of the magnetization induced by the DMI [199, 201] and taken into account with the term $\nabla \boldsymbol{V}(\boldsymbol{r})$, are not strong enough to balance the Magnus force, so that the skyrmion collides with the edges and gets annihilated due to the breaking of the topological protection.

The Magnus force behaves like the Lorentz force for electrical charges and gives rise to a phenomenon very similar to the traditional Hall effect, even if here the skyrmion does not carry any electrical charge but only a topological charge. This is why this effect is called skyrmion Hall effect.

Like discussed in [198] and in [199], reversing the sign of the magnetization and thus the sign of the topological charge, turning it from $Q = +1$ to $Q = -1$, the topological Magnus force $\boldsymbol{G} \times \boldsymbol{v}_d$ is reversed, since $\boldsymbol{G} = (0, 0, 4\pi Q)$ is strictly related to the skyrmion number. As a consequence, reversing the sign of the topological charge, the skyrmions become antiskyrmions and will be accumulated at the opposite edge of the sample, in strict analogy to what happened with the Hall effect for electrical charges. Of course, when the Magnus force deviates the trajectory of an antiskyrmion, the resulting effect is called antiskyrmion Hall effect.

This can be proven also looking at the expression of $v_{d,y}$ for both geometries:

$$v_{d,y} = \begin{cases} \left(\mathcal{D} G \frac{\alpha - \beta}{G^2 + (\alpha \mathcal{D})^2} \right) v_{s,x} & \text{for CIP} \\ \frac{jQ\mathcal{B}_{xx}}{(\alpha \mathcal{D})^2 + Q^2} & \text{for CPP} \end{cases} \tag{16.30}$$

The $v_{d,y}$ component for the CIP case is directly proportional to $G = 4\pi Q$: reversing the sign of the topological charge also the velocity component will be reversed. The component for the CPP case is proportional directly to Q and thus behaves in the same way. So, applying the same current density, both skyrmions and antiskyrmions propagate in the x-direction with the same speed, while they exhibit equal and opposite transverse velocities.

The (anti)skyrmion Hall angle is defined as the angle between the direction of the applied current and the direction of the resulting motion of the texture, and its expression is

$$\Phi_{sk} = arctan\left(\frac{v_y}{v_x}\right) \tag{16.31}$$

Focusing on the CPP geometry, both the skyrmion and the antiskyrmion Hall angle [199, 198] are equal to

$$\Phi_{sk} = arctan\left(-\frac{Q}{\alpha \mathcal{D}}\right) \tag{16.32}$$

This equality can be easily found by substituting equation 16.29 inside the definition of the (anti)skyrmion Hall angle.

Due to some differences inside the symmetry of the spin texture constituting the antiskyrmions, the antiskyrmion Hall angle, differently from the skyrmion Hall angle, is dependent on the angle θ that the applied current density has with the x-direction, so that its

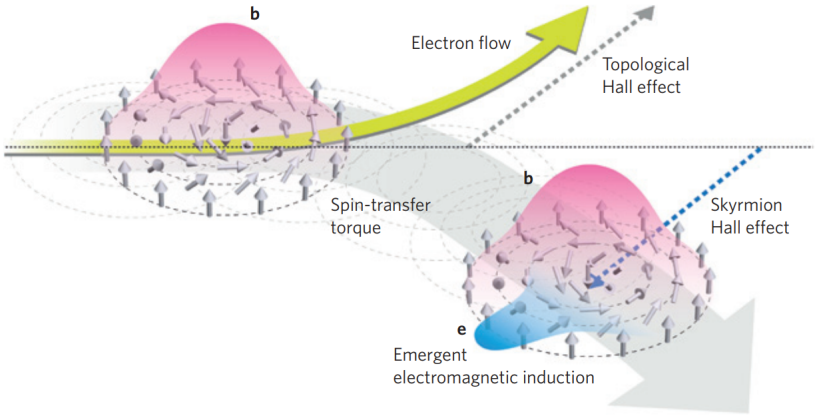

Figure 16.14: Schematic representation of the topological Hall effect and of the skyrmion Hall effect. Electrons are deflected by the Lorentz force due to the emergent magnetic field of the skyrmion, and this results into the topological Hall effect. The velocity of the skyrmion has a transverse component due to the Magnus force in the Thiele equation, and this is the skyrmion Hall effect. Due to the time variation of the emergent magnetic field carried by the skyrmion, is present also an emergent electric field, that is, emergent electromagnetic induction. Figure extracted from [202].

complete expression actually is

$$\Phi_{ask} = arctan\left(-\frac{Q}{\alpha\mathcal{D}}\right) - 2\theta \tag{16.33}$$

It has been proven in [199] that if the current is injected along the direction $\theta = \frac{1}{2}arctan(-\frac{Q}{\alpha\mathcal{D}})$, so that $\Phi_{ask} = 0$, the antiskyrmion Hall effect is cancelled and the texture moves exactly along the current direction, without any transverse motion. Since the maximum speed at which both skyrmions and antiskyrmions can move inside a nanotrack without being annihilated is limited by the competition between the (anti)skyrmion Hall effect and the edge repulsion, enabling a motion with zero antiskyrmion Hall angle can largely increase the maximum velocity of antiskyrmions, allowing a higher throughput for the devices potentially based on them.

Mitigation of the skyrmion Hall effect

Since the skyrmion Hall effect may lead to the annihilation of the particle and so of the information it carries, it is a well known issue in the design of skyrmionic devices. Looking at the expression of $v_{d,y}$ in 16.27, it can be noticed that if $\alpha = \beta$ the transverse velocity component is cancelled and the skyrmion Hall effect disappears. However, these two parameters depend on material properties, and it's clear that is impossible to rely on this equality from a design point of view; of course, thanks to the repulsion from the edges of the nanotrack, the skyrmion is able to travel along the nanotrack even if β is not too different from α, but in this case the current density must remain below a certain threshold so that the Magnus force doesn't overcome the repulsive forces from the boundaries, and this of course limits the maximum throughput of the device. So, it's clear why some other solutions to the skyrmion Hall effect must be found, and these solutions must be able to work both with the CIP and with the CPP geometry (even if the CPP configuration has a higher driving efficiency with respect to CIP).

In [203] two methods have been proposed for engineering a potential well, needed for confining the skyrmion in the centre of the nanotrack and preventing its annihilation. The first method proposed tunes the magnetic anisotropy along the width of the nanotrack, reducing the value of the PMA in the centre with respect to the edges. This will form a path of lower resistance all along the nanotrack, since there the magnetization will be

allowed to flip more easily due to a lower value of the effective field. Of course, however, there is still a certain value of velocity above which the repulsion from the edges won't be enough and the skyrmion can be destroyed. The patterning of the PMA can be performed by ion irradiation, combined together with high-resolution litography. Of course this must be done during the fabrication step and is a static control, without any possibility of change during the lifetime of the device.

The second method proposed is to add more ferromagnetic material at the edges of the nanotrack. Doing so the demagnetization field is increased at the inner edges of the modified nanotrack and decreased at its centre: so there is again a magnetic potential well which forces the skyrmion to move at the centre of the track. The threshold velocity above which annihilation happens in this case is even higher that the one that can be obtained through PMA patterning.

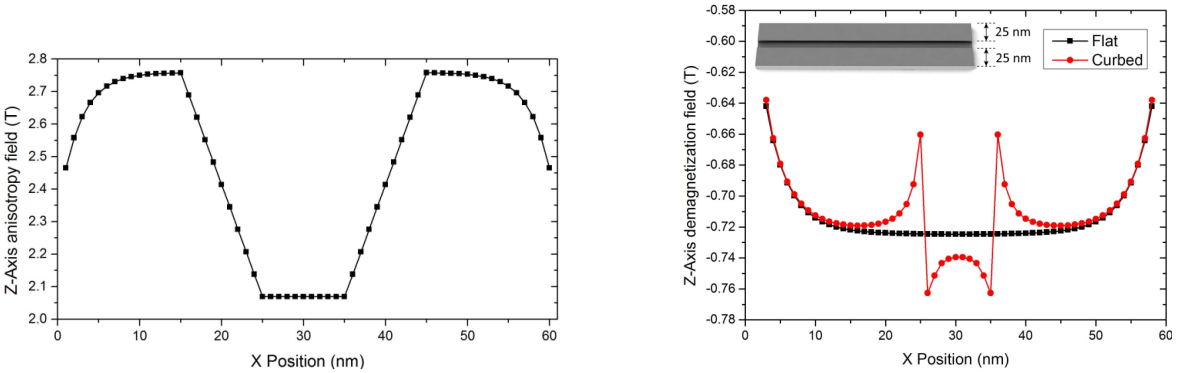

(a) (b)

Figure 16.15: (a) z-axis anisotropy field along the width of the nanotrack after patterning of the PMA constant: K_u has a lower value at the centre of the nanotrack. (b) z-axis demagnetization field for the traditional nanotrack (black curve) and for the modified nanotrack shown in the inset (red curve). Figures extracted from [203].

A completely different possibility is presented in [197]. The structure of the device described in this article is reported in figure 16.16: a FM layer with positive background magnetization is separated from a bottom FM layer with opposite background magnetization by an insulating spacer. Below the bottom FM layer, a HM substrate allows the flow of a current in the x-direction and is able to generate a spin-polarized current vertically directed with spin direction along $+y$. The peculiarity of this structure is to have an antiferromagnetic (AFM) exchange coupling between the top and the bottom FM layers. The Hamiltonian for this kind of interaction is

$$H_{inter} = -A_{inter} \sum_i \boldsymbol{m}_i^T \cdot \boldsymbol{m}_i^B \tag{16.34}$$

where T stands for top, B stands for bottom and A_{inter}, the interlayer AFM exchange stiffness, is negative. As a result, if the magnetic moments of the top layer point in one direction, the moments of the bottom layer will point exactly in the opposite direction, in order to minimize the total energy of the system, equal to $H_{total} = H_T + H_B + H_{inter}$.

In this structure is possible to nucleate a skyrmion by injecting a current inside the MTJ shown in figure 16.16 (the nucleation of a skyrmion by allowing a current flow through a MTJ is explained in section 16.2.5); the resulting spin-polarized current is not able to reach the bottom FM layer, so if the AFM exchange coupling is not strong enough only a single skyrmion will be nucleated in the top layer. If instead the coupling between the two layers is strong, the nucleation of a skyrmion in the top FM layer will induce the nucleation of a skyrmion with opposite topological charge (since the spin directions are opposite, as detailed by equation 16.7) also in the bottom FM layer. These two skyrmions

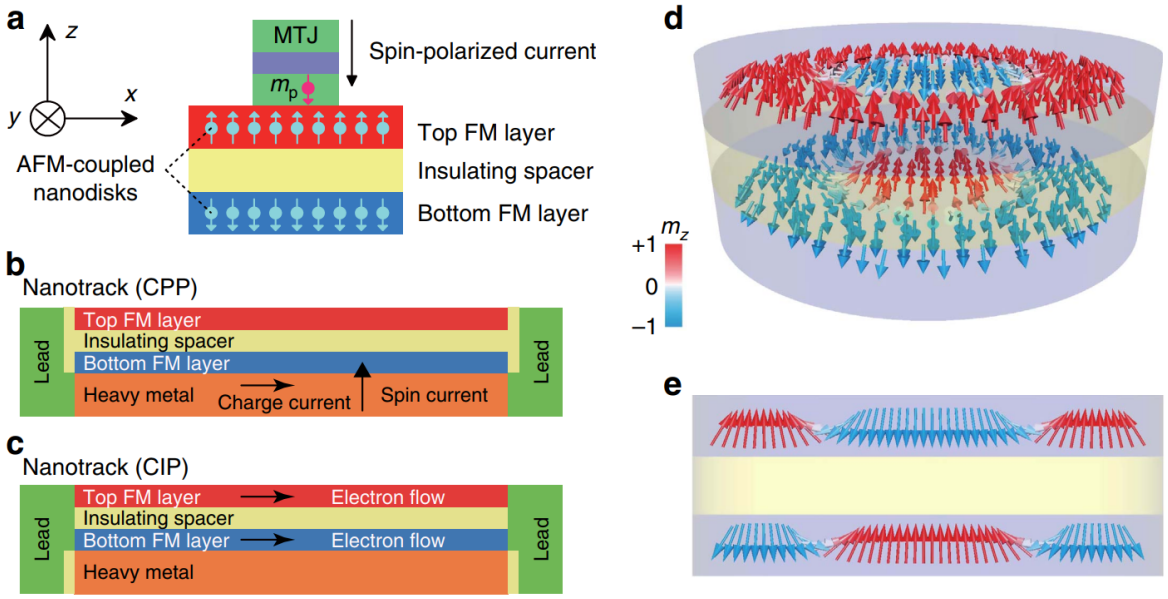

Figure 16.16: Schematic of the AFM exchange coupled bilayer system. (a) MTJ write-head needed for the nucleation of a single skyrmion in the top FM layer. (b-c) Bilayer nanotrack where the CPP geometry (b) or the CIP geometry (c) is exploited for the skyrmion motion. (d) Illustration of the bilayer-skyrmion. (e) Side view of the bilayer skyrmion along the diameter section. Figure extracted from [197].

(magnetic bilayer skyrmion) are bounded and move together along the track. If the current is injected according to the CIP geometry, the texture of both skyrmions will be subjected to the torque from the conduction electrons. If instead is adopted the CPP geometry, only the bottom skyrmion will be subjected to the torque of the spin-polarized current coming from the SHE: the top skyrmion will move only due to the AFM exchange coupling.

The key point is that the two textures have opposite topological charge: for this reason, the $\boldsymbol{G} \times \boldsymbol{v}^{(d)}$ term (Magnus force) that appears in the Thiele equation of both CIP and CPP geometry is cancelled. Like mentioned in section 16.2.3, in fact, $\boldsymbol{G} = (0, 0, 4\pi Q)$ depends on the topological charge, and if the sign of the topological charge is reversed also the Magnus force will change its sign. Thanks to the bound connecting the skyrmions inside the two layers, the total Magnus force on the system of the bilayer skyrmion is exactly zero. In this way is possible to obtain the movement along a straight line without any skyrmion Hall effect: this allows to obtain a system in which the velocity of the information carriers can reach even $1000\,\mathrm{ms}^{-1}$. Moreover, in the article is demonstrated that the bilayer skyrmion maintains the same (low) depinning current density of a single skyrmion, and that the CPP geometry is again the most efficient configuration, like it happened in the case of single skyrmions.

In the same article is proposed also a second method to nucleate a bilayer skyrmion, exploiting the result presented in [171]: it is enough in fact first to nucleate an AFM-coupled DW pair, to move it along a narrow track an then, through a narrow-wide junction geometry, to convert it into a bilayer skyrmion, similarly to what has been discussed in section 16.2.1.

16.2.4 Nucleation

The nucleation of skyrmions can be obtained in many different ways: by means of an electrical current, of magnetic fields, or even with local heating using laser irradiation; again, from an application point of view the nucleation through the injection of an electrical current is the most promising mechanism.

STT

In [204] has been studied the nucleation of a single skyrmion in a thin magnetic film by injecting a out-of-plane spin-polarized current perpendicularly to the film plane. By changing the simulation parameters it has been studied also the dependence of the threshold current density on the Gilbert damping, on the magnitude of the DMI and on the PMA coefficient.

Notch

Another mechanism for the nucleation of skyrmions has been proposed in [201]. Here a notch inside the ferromagnetic material is exposed to a magnetic field and to a flowing current. Even if the magnetic field considered in the article is directed along $+z$, the spin direction along the edges of the sample is in-plane due to the DM interaction. When injecting an electric current, the STT and the DMI together make the spins first swell out around the corner, then twist and point down at the core of the new skyrmion, which after some fluctuations in the radius size will detach from the corner and move in the sample due to the STT from the current. The authors have studied the dependence on the sign of the magnetic field, on the sign of the current density and on the shape and dimension of the notch. It has been proved that the essential feature is the spin pattern along the edge of the sample, together with the direction of the injected current: a current with opposite sign is not able to generate a skyrmion, due to the unique direction that the spin movement has in the Larmor precession. If the in-plane component of the spin is guaranteed and if the current has the correct direction (given the sign of the applied magnetic field), then even a notch with round shape would allow the nucleation.

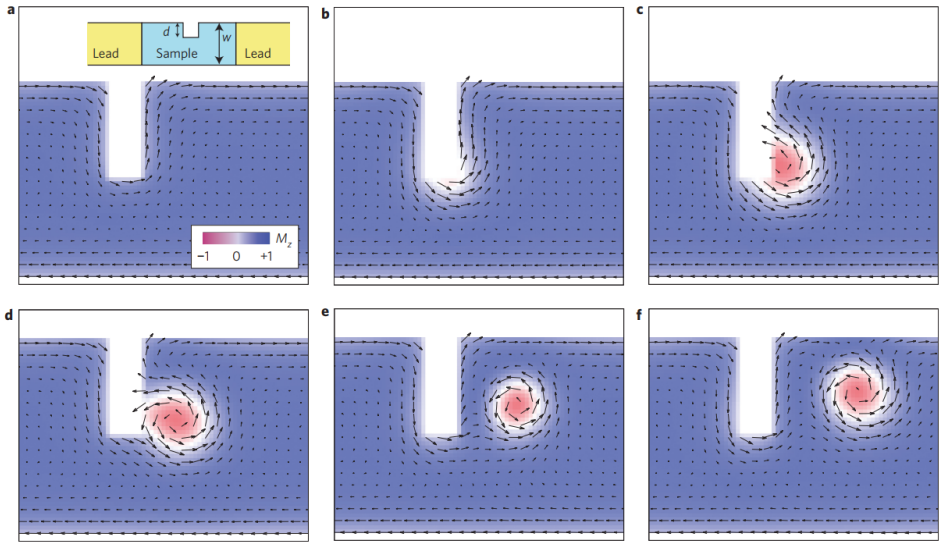

Figure 16.17: Simulation snapshots showing the nucleation of a skyrmion around a rectangular notch. Blue(red) represents the $+z(-z)$ component of the magnetization. Figure extracted from [201].

16.2.5 Detection

The detection of skyrmions can be accomplished mainly through either the topological Hall effect or the magnetoresistance effect; only the latter method, however, can be easily performed in a fully electrical way, and so is the easiest to be implemented in an electronic device [173].

In [205] the electrical detection of a single skyrmion based on the tunnel magnetoresistance (TMR) effect at room temperature has been detailed. The structure of the proposed read-

head is made by a HM layer, above which is deposited an ultrathin ferromagnetic layer, in order to achieve a strong i-DMI (interfacial DMI). This ferromagnetic layer will host the skyrmion and is at the same time the free layer of a MTJ; it has an elliptical cross section with the major axis oriented along the y-direction. The pinned layer of the MTJ has a fixed out-of-plane easy axis of the magnetization and is a nano-contact with 50 nm of diameter, since the average value of the skyrmion diameter, with the parameters chosen for the simulation, is around 40 nm. First of all, the skyrmion nucleation is achieved, like proposed in [204], by injecting a current pulse through the MTJ.

Spin-polarized current The current passing through the ferromagnetic layer with fixed magnetization becomes spin-polarized. Like explained by [193], in fact, the density of states (DOS) of a ferromagnetic metal is different from the DOS of a normal metal: like shown in figure 16.18a, in this case the DOS is different for the two spin states, so that the spin-up band at the Fermi level is mostly filled, while there are many empty states available in the spin-down band. So, the conduction electrons injected in the ferromagnet will encounter a different resistivity, according to their spin: the spin-down electrons have more states to scatter into, and as a result they see a higher resistivity ($\rho_\downarrow$) compared to the one ($\rho_\uparrow$) seen by the spin up electrons. So, overall, this leads to the spin-polarization of the current injected, where the degree of spin-polarization is given by

$$P = \frac{\rho_\downarrow - \rho_\uparrow}{\rho_\downarrow + \rho_\uparrow} \tag{16.35}$$

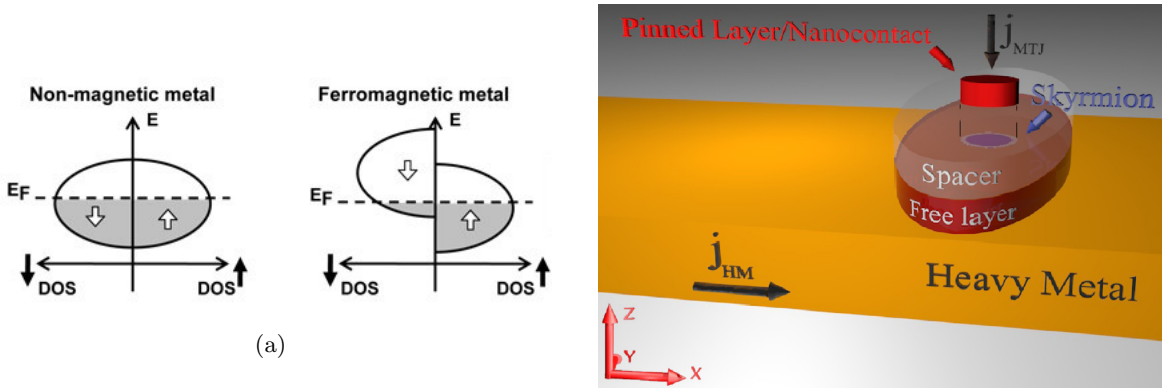

(a) (b)

Figure 16.18: (a) DOS of a metal and of a ferromagnetic material. The misalignment of the spin-up and of the spin-down band in the energy diagram determines a higher number of states available in the spin-down band. Adapted from [206]. (b) Structure of the detection-head proposed in [205]. The MTJ structure is exploited both for the detection and for the nucleation, while a current flowing in the HM layer controls the motion of the skyrmion in the free layer via SHE. Figure extracted from [205].

Once the skyrmion is nucleated, the main problem to solve is its thermal drift below the detection head. This thermal drift induces shape deformations, apart from the so called breathing (expansions and compressions of the spin texture), and most of all makes the skyrmion follow a Brownian motion, which forces it to stay most of the time away from the detection head: that's why it cannot be detected by means of just a current flowing through the read-head. The motion of the skyrmion must instead become controlled, and must force it to pass periodically below the detection area. To do so, an electrical microwave current is made flow in the HM layer in the x-direction: in this way, thanks to the SHE, the skyrmion is forced to move along the y-axis of the free layer. The consequence of this periodic passage is a periodic variation of the out-of-plane component of the magnetization: then, due to

the tunnel magnetoresistance effect, the resistance that a current density J_{MTJ} across the MTJ encounters will change periodically, and this allows the detection of the skyrmion.

16.2.6 Skyrmion size

Like observed in [207], a bit of confusion can be found in literature about the topic of the skyrmion size, and many different and non-equivalent expressions have been used up to now. Skyrmions are made of an inner core, an outer domain and a wall separating them; so, when dealing with the skyrmion size, first of all is necessary to distinguish between the contour of the region where $m_z = 0$, whose radius is called skyrmion size R, and the wall width w surrounding the core. These two quantities are visually defined in figure 16.19.

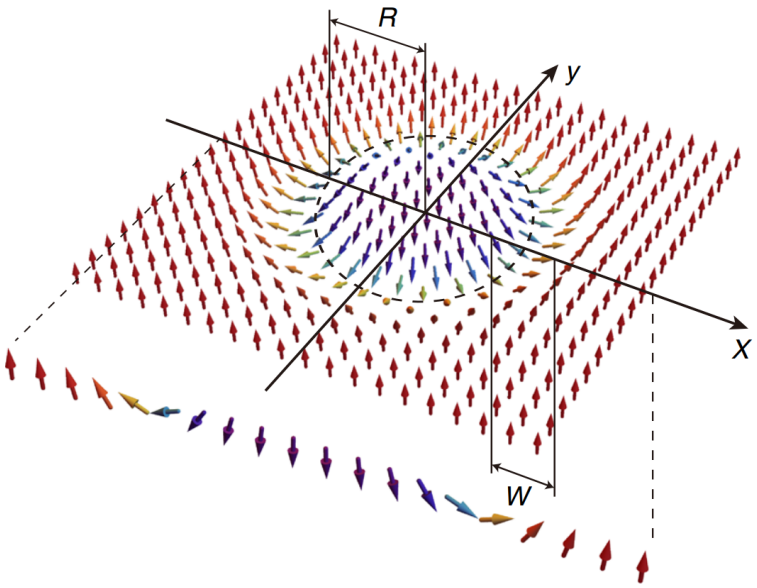

Figure 16.19: Schematic of a Néel skyrmion showing the visual definition of the skyrmion size R and of the wall width w. Figure extracted from [207].

The authors of this article focus on Néel skyrmions stabilized by i-DMI in a ultra-thin ferromagnetic film; they confirm that the same results apply also to Bloch skyrmions stabilized by bulk DMI. However, the basic assumption is that the thickness of the film is much smaller than both R and w, so that the demagnetizing field can be neglected. If the thickness of the film increases, the model they present and all the 2D theories behind it are no longer applicable.

The energy terms taken into account are the exchange energy, the DMI energy, the anisotropy energy and the Zeeman energy, where A is the exchange constant, D is the DMI coefficient, K is the perpendicular easy-axis anisotropy and B the perpendicular magnetic field. In the article it is first found the general and exact expression of the total energy E including these terms. The skyrmion radius and the wall width are those values that minimize the energy of the system: so, their dependence on A, D, K and B is found by minimizing the total energy with respect to R and w separately. This is the main innovation that this article brings on the topic: usually the domain wall width was either considered constant or dependent on the value of R. Doing so, instead, the simulation points are quite perfectly interpolated by the curve obtained by minimizing the exact expression of E with respect to R and w and by varying the values of A, K, D and B that appear in it. In figure 16.20 are shown the four plots, where the symbols represent the simulation data and the solid lines are the results obtained theoretically from the exact expression of the energy.

However, doing so is not possible to get the complete expression of R and w, expression which would be useful to have a clear idea about their dependence on the four parameters.

For this reason, in the same article the expression of the energy was approximated under the assumption $R >> w$, and minimizing it again with respect to R and w the following expressions can be found for $B = 0$:

$$R = \pi D \sqrt{\frac{A}{16AK^2 - \pi^2 D^2 K}} \tag{16.36}$$

$$w = \frac{\pi D}{4K} \tag{16.37}$$

If $B \neq 0$ there is no closed-form solution; however, the approximated dependency of both R and w on B can still be simulated by varying its value in the two minimized expressions. In this way the dashed curves shown in figure 16.20 are obtained.

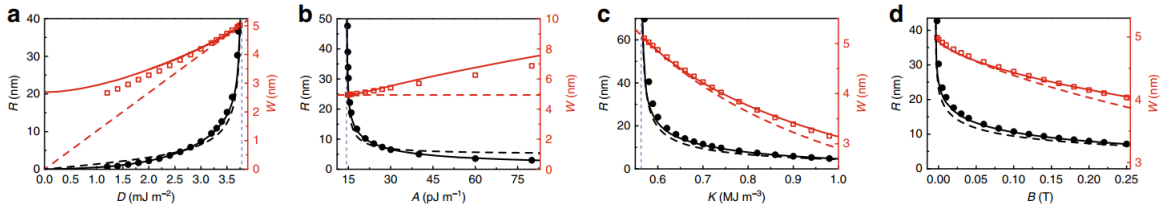

Figure 16.20: Comparison between simulation data (symbols), exact theoretical result (solid curve) and approximated theoretical result (dashed curve) for both the skyrmion size R and the wall width w. The limit of the region where the skyrmion is the configuration minimizing the energy of the system is shown by the vertical dashed line. Figure extracted from [207].

From equation 16.36, imposing that R is a real and finite number, it can be derived that

$$16AK > \pi^2 D^2 \tag{16.38}$$

From this expression is possible to determine the limit value for A, D and K: these values are reported in the plots like a vertical dashed line, which agrees well with the simulations even if it has been derived from an approximate expression. If these three parameters do not respect the range obtainable from equation 16.38, the stable state is not a skyrmion but stripe domains.

In figure 16.21 is shown the comparison with the results obtained from two different articles. In particular, the one indicated as *Ref. [26]* is [190], whose results are commented in section 16.3.3. From this comparison is possible to realize the validity of the model proposed, and how it should be trusted more than different models proposed in other articles.

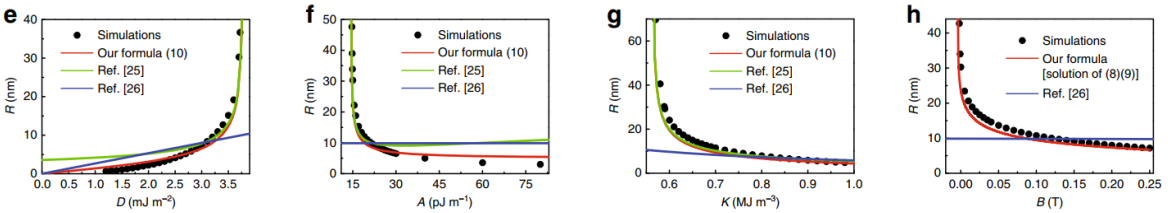

Figure 16.21: Skyrmion size: comparison between simulation data, the results provided by the approximated expression of the energy and the results obtained in two different articles. Figure extracted from [207].

In article [207] the skyrmions are assumed to be isolated inside an infinite medium, so the edge effects are not taken into account. In [208] instead are studied the effects that the repulsive forces from the boundaries of a tapered nanotrack have on the skyrmion size. The nanotrack used in the simulations, shown in figure 16.22, exploits the results of [197]: it is in fact made by two FM layers separated by a spacer, so that the skyrmion Hall effect

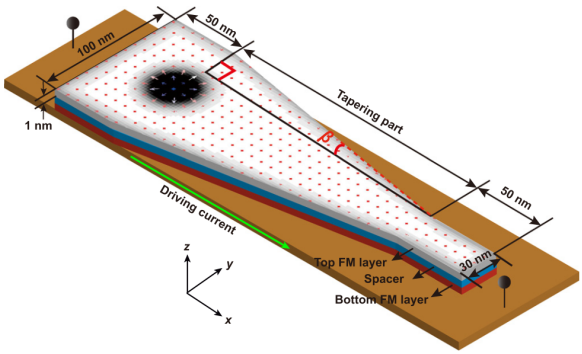

Figure 16.22: Tapered nanotrack used in [208]: two FM layers are AFM exchange-coupled, so that the skyrmion Hall effect is suppressed. The skyrmion is moved by a current flowing in the HM layer via SHE. The varying width of the nanotrack exerts a compression on the skyrmion texture. The slope is defined by $k = tan(\beta)$. Figure extracted from [208].

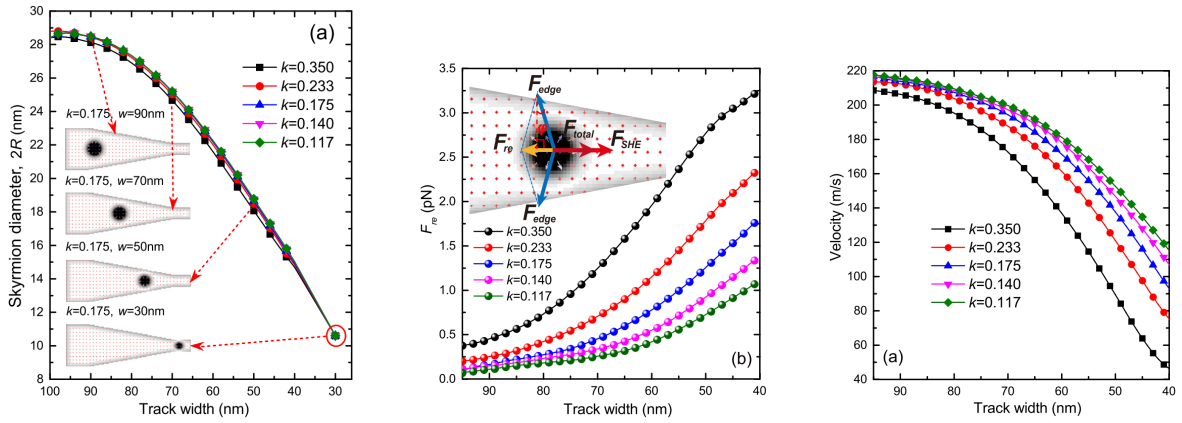

(a) (b) (c)

Figure 16.23: (a) Dependence of the diameter of the skyrmion on the width of the nanotrack. The dependence on the slope k of the nanotrack is very weak. (b) The resultant of the repulsive forces from the edges increases when the skyrmion radius decreases; increasing the slope of the nanotrack the force component that opposes to the skyrmion's motion increases. The inset shows the force components competing in the motion. (c) The velocity of the skyrmion decreases when the track width decreases; increasing the slope of the nanotrack the velocity decreases as well. Figures extracted from [208].

is cancelled thanks to the AFM exchange coupling between the two layers, like already discussed in section 16.2.3. The skyrmion movement is achieved through the SHE.

The results shown in the article are reported in figure 16.23. The variation of the skyrmion size according to the track width is shown in figure 16.23a: while the skyrmion moves along the track, the edges exert a repulsive force on its texture, shrinking it. In particular, at the end of the nanotrack, where the width is of 30 nm, the skyrmion diameter is 10 nm. It's difficult to obtain such a small size directly with the nucleation of a skyrmion via STT: that's why a tapered nanotrack could become useful in increasing the packaging density of information in a skyrmionic memory.

The authors observe also that the repulsive force exerted by the non-parallel edges makes the velocity decrease with the track width (figure 16.23c). The summary of the forces competing in the system is shown in the inset of figure 16.23b: each edge exerts a force $\boldsymbol{F}_{edge}$ on the texture, and the sum of these two forces is $\boldsymbol{F}_{re}$, opposite in sign with respect to the force $\boldsymbol{F}_{SHE}$ responsible of the motion of the skyrmion. Like shown in figure 16.23b, $\boldsymbol{F}_{re}$ increases while the width of the track decreases, and opposing to $\boldsymbol{F}_{SHE}$ it makes the resulting skyrmion velocity decrease.

The result concerning the skyrmion size shown in figure 16.23a is confirmed also by the simulation results presented in [203], where the width of the considered nanotrack spans between 28 nm and 10 nm.

16.3 Applications

Skyrmions present many advantages with respect to domain walls: they need a lower depinning current density and they are smaller, so overall they allow either to consume less power while maintaining the same throughput, or to increase the throughput while maintaining the same power consumption.

It is a fact that a lot of research has already been done on DW racetrack memories: however, thanks to the result shown in [171], is now possible to reversibly convert DW pairs into skyrmions and vice versa. This allows to exploit all the work already done on the optimization of racetrack memories, together with all the advantages presented by skyrmions. Not only: as it will be shown in this section, different designs for skyrmionic logic gates have been proposed. This allows even to realize some logic in memory: the information could be stored in the form of DW pairs, which can then be elaborated by skyrmionic gates after a conversion, and the result of the elaboration can be stored again like DW pair somewhere else.

Of course, as soon as the basic logic gates are available, it is then possible to build more complex computing architectures: this topic will be discussed in chapter **??**.

16.3.1 Logic gates using the DW pair-skyrmion reversible conversion

In the first part of [183] is studied the variation of the topological numbers of skyrmionic structures according to the physical parameters of the material used for the wide part of a nanojunction, exploiting the reversible conversion from DW pair to skyrmion proposed in [171]. This topic has been detailed in section 16.2.1. In the second part of [183] the DW pair-skyrmion conversion is exploited for designing the basic logic gates. Here a skyrmion signifies a logic 1, while its absence represents a 0.

Figure 16.24a shows the structure of the *OR* gate in different simulation points and according to different input combinations. In the $1+0$ and the $0+1$ case, the only skyrmion on the input is converted into a DW pair thanks to the presence of the narrow junction, is propagated along the structure and is converted back into a skyrmion in the wide output region. When two skyrmions are present they are both converted into a DW pair, and when these two structures meet at the central junction of the Y structure they merge into a single DW pair, which is then propagated towards the output and converted back into a single skyrmion like before.

In figure 16.24b is represented the structure of the *AND* gate. It is very similar to the *OR* gate, with the only difference of a wider bottom half in the Y central junction. In this way, considering the $1 \cdot 0$ and the $0 \cdot 1$ cases, when injecting the same current density as before, the current density in the bottom half of the junction will be lower with respect to the case of the *OR* gate, so the DW pair, since it is pushed towards a wider region, is converted not into a skyrmion but into a meron. Since the meron has the peculiarity of remaining attached to the sample edge, when it reaches the output junction it is driven away from the nanotrack: so in both cases the output of the function is 0, as expected. In the $1 \cdot 1$ case, instead, the two DW pairs are still able to merge into a single DW pair, which is propagated towards the output and converted back into a single skyrmion, correctly providing a 1 on the output.

The cases $0 + 0$ and $0 \cdot 0$ are not shown since they are trivial: if we don't provide any skyrmion on the inputs of the gates, the output will be for sure 0.

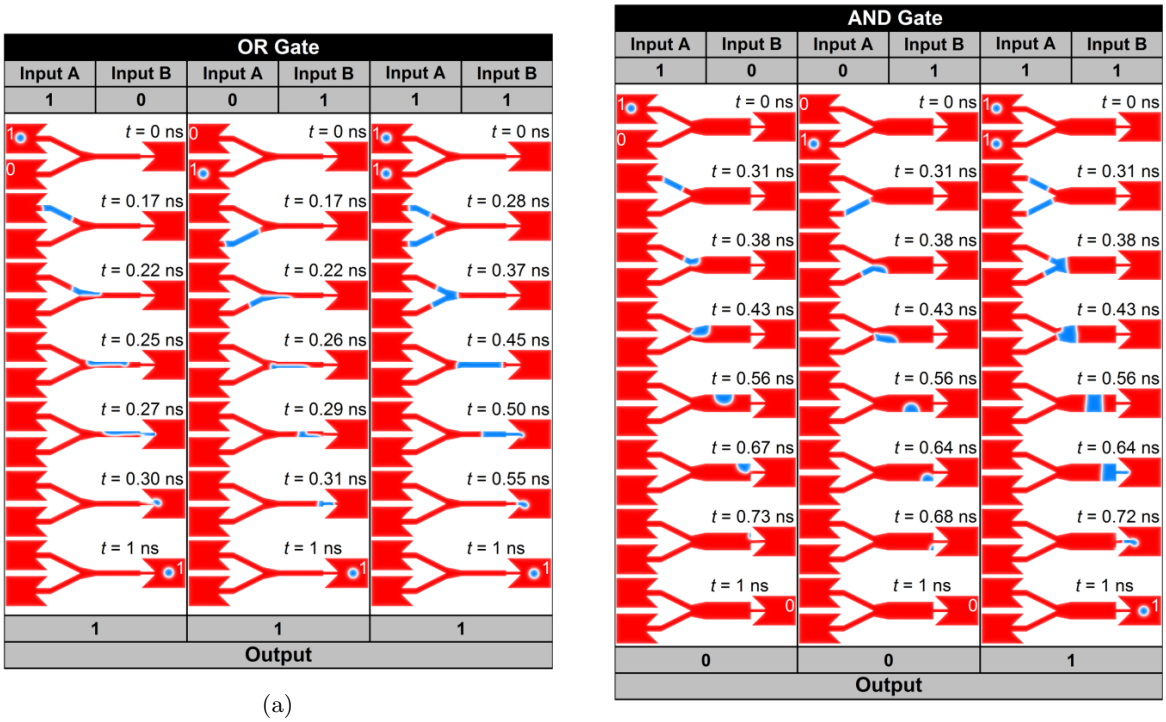

(a) (b)

Figure 16.24: (a) *OR* gate: snapshots of micromagnetic simulation at different instants showing the cases $1 + 0$, $0 + 1$ and $1 + 1$. The $0 + 0$ case is trivial. (b) *AND* gate: snapshots of micromagnetic simulations for the cases $1 \cdot 0$, $0 \cdot 1$ and $1 \cdot 1$. The $0 \cdot 0$ case is trivial. Figures extracted from [183].

It is worth noticing that, using the same structure of the *OR* gate but exchanging output and inputs, the gate obtained is able to perform the duplication of a single skyrmion, as shown in figure 16.25. Like observed by the authors, the capability of duplicating the information carried by a single skyrmion is very important for any skyrmionic device.

Even if not specified by the authors of the article, is worth noticing that these gates could in principle be used inside a conservative skyrmionic logic system: the skyrmions on the output of each of these gates could in fact be used in the remaining part of a larger circuit to trigger the computation of other logic functions, like proposed in [209] for a different type of logic gates (see 16.3.2).

16.3.2 Logic gates for conservative logic systems

The application proposed in [209] is a different method to realize the basic logic gates. It exploits the results shown in [203], adopting an additional layer of FM material at the edges of the nanotrack to achieve the confinement of the skyrmion, like shown in figure 16.26. Moreover, the system that can be obtained from these gates is defined "conservative", because once the skyrmions have crossed the whole gate, allowing the computation of the logic function, they can be collected at the other end and used to trigger the computation of new functions, without the need of nucleating new skyrmions, which is an energetically expensive operation. Finally, the way in which is taken advantage of the complex physics of skyrmions in realizing the computations deserves an additional mention: here the features that in other skyrmionic devices represent a problem, like the edge-skyrmion repulsion, the skyrmion-skyrmion repulsion, and most of all the skyrmion Hall effect, are not only tolerated, but actually exploited for realizing the computation.

The structure of the gates proposed is shown in figure 16.27. Also in this case a logic 1 is represented by a skyrmion and a 0 by its absence. The device shown in 16.27a implements

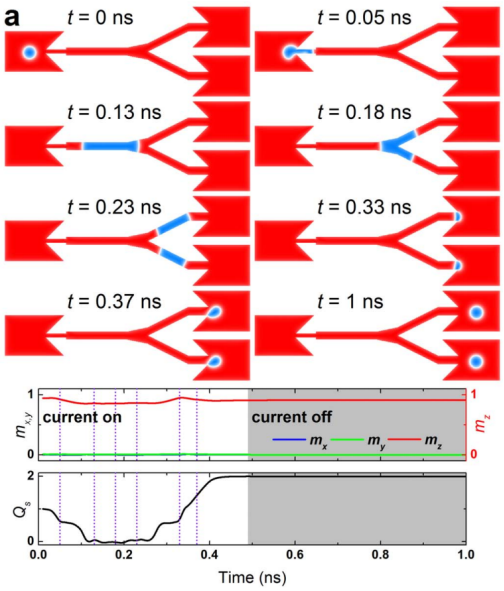

Figure 16.25: Duplication of a skyrmion. The middle panel shows the time evolution of the magnetization components m_x, m_y and m_z. The bottom panel shows the time evolution of the skyrmion number: from $Q = 1$ (one skyrmion) it becomes $Q = 0$ (DW pair) and then $Q = 2$ (two skyrmions). Figure extracted from [183].

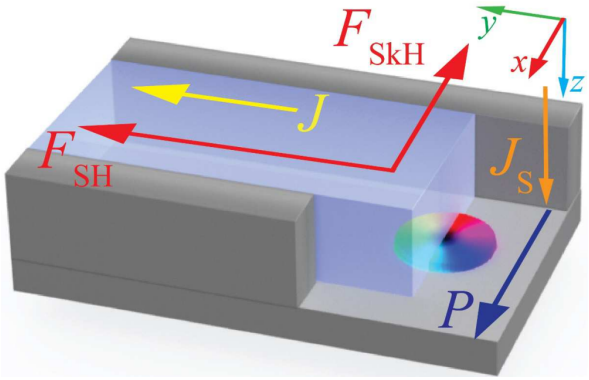

Figure 16.26: Structure of the nanotrack used in [209], made of Pt HM (blue) and Co FM (gray, with polarization P). The current J injected in the HM is converted via SHE into the spin-polarized current J_S, producing on the skyrmion (multicolor circle) a force F_{SH} in the direction of the electrical current $(+y)$ and a force F_{SkH}, due to the skyrmion Hall effect, directed along $-x$. Figure extracted from [209].

the *AND* and the *OR* function at once: remembering that each skyrmion is subjected at the same time to a force component along $+y$ and to a second force component directed along $-x$, is easy to understand the working mechanism behind the gate. When a single skyrmion is present (case $A = 0,\ B = 1$ or $A = 1,\ B = 0$), it moves along its track as long as there is no way to move towards the $-x$-direction. If the skyrmion is in the rightmost track and it reaches the central junction, the skyrmion Hall effect will make it move towards left and change its track. This won't happen only if there is already a skyrmion occupying the left track ($A = 1,\ B = 1$): in this case the skyrmion-skyrmion repulsion prevails and both skyrmions continue on their respective track, correctly providing a logic 1 on both outputs.

In 16.27b is shown the structure of the *INV/COPY* gate. This time, to allow the correct functioning, the *CTRL* input must always be set to 1. Then, if both skyrmions are present, the skyrmion-skyrmion repulsion in the central junction will make the rightmost go towards

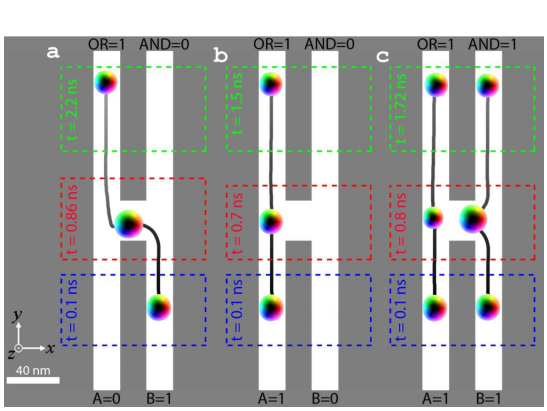

(a)

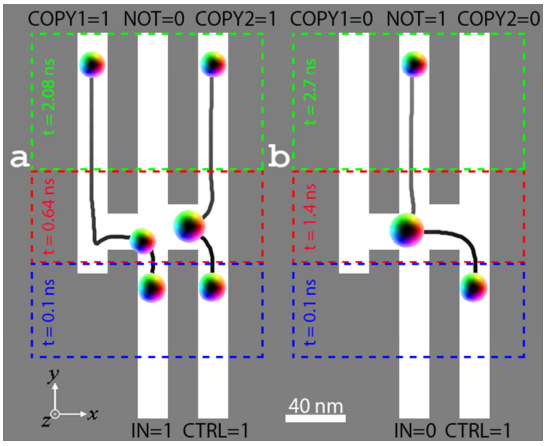

(b)

Figure 16.27: (a) *AND/OR* gate: schematic of the behaviour of the gate for the cases ($A = 0,\ B = 1$), ($A = 1,\ B = 0$), ($A = 1,\ B = 1$). The ($A = 0,\ B = 0$) case is trivial. (b) *COPY/NOT* gate: schematic of the behaviour of the gate for the cases $IN = 1$ and $IN = 0$. Figures extracted from [209].

the *COPY2* output, and together with the skyrmion Hall effect it will make the leftmost reach the *COPY1* output. In this way the value of the input ($IN = 1$) is copied on the two *COPY* outputs, while it is inverted on the *NOT* output. If a single skyrmion is present, the skyrmion Hall effect will make it go towards the $-x$ direction, but it is not strong enough to make it reach the *COPY1* track: again, the value of the input is copied on the two *COPY* outputs and inverted on the *NOT* output.

Having the implementation of both the *AND/OR* function and of the *NOT* function, it is in principle possible to realize any boolean logic function. However, here the correct functioning of the device is based on the forces that arise from the interactions of skyrmions inside the same logic gate. It is then of vital importance to synchronize their movement and to control their timing: differently from the traditional electric circuits, in which (at least in lumped circuits) the speed of the signal propagation can be approximated as infinite, here the speed of skyrmions is limited and the time they take in propagating along each track must be carefully considered. That's why in the same article has been proposed also the structure of a signal synchronizer, shown in figure 16.28a. It is realized with a 7 nm wide notch that blocks the passage of the skyrmion, which is around 20 nm wide.

Like discussed in section 16.2.6, a tapered nanotrack has the effect of decreasing the radius of a skyrmion passing through it. However, the repulsion from the edges gives rise to a force component antiparallel with respect to the force $\boldsymbol{F}_{SH}$, which is coming from the SHE and is responsible for the skyrmion motion. The force component $\boldsymbol{F}_{SH}$ is directly proportional to the current density applied ([208]): as a result, if the current density is not enough, the skyrmion propagation will be blocked by the notch. The passage of the skyrmion is allowed only when a higher current density is applied: in this way the force component $\boldsymbol{F}_{SH}$ becomes able to overcome the repulsion force coming from the edges, the skyrmion diameter is reduced due to edge repulsions, and the information can go through the restriction and continue the propagation along the circuit.

In this way the current needed to allow the data propagation becomes at the same time also the clock needed for synchronizing it: the low logic level of the current will correspond to a value higher than the depinning current, but lower than the value needed for allowing the passage of the skyrmions through the notches present in the circuit; this high value will be applied periodically only for a short period of time, so that the resulting waveform of the current will have a very small duty cycle.

The last structure proposed in the paper is the one of a *FULL ADDER*, shown in figure

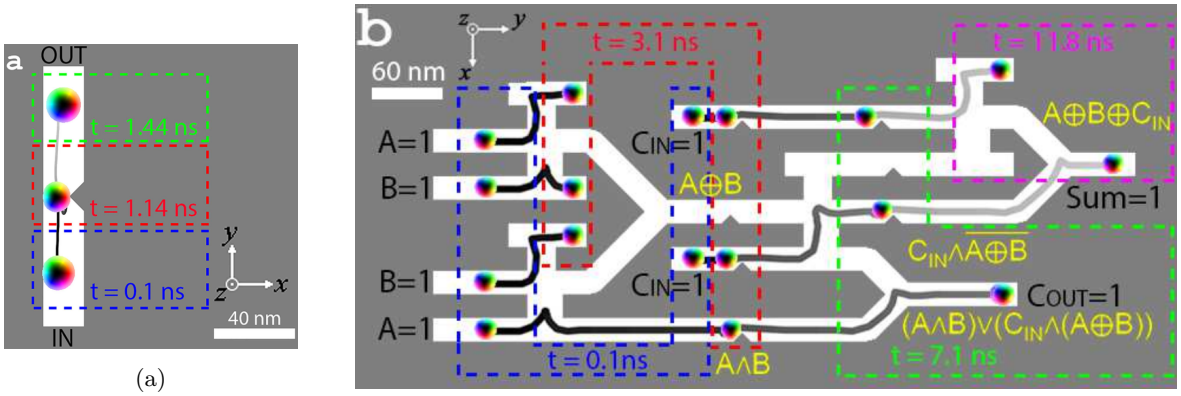

(a) (b)

Figure 16.28: (a) Signal synchronizer: the 7 nm wide notch blocks the passage of the skyrmion until a higher current density level is applied. (b) *Full Adder* structure, built using the *INV/COPY* gate, the signal synchronizer and some join tracks. Figures extracted from [209].

16.28b. For understanding its behaviour is important to notice that the structure of the *INV/COPY* gate is able to perform also different logic computations, if the assumption of having always an input $CTRL = 1$ is relaxed. It's easy to verify that the same structure corresponds to the truth table 16.2. The names of the inputs and of the outputs of the gate have been redefined, like shown in figure **??**, for avoiding any confusion about the actual logic function implemented.

Table 16.2: Truth table for the *INV/-COPY* gate

A	B	OUT2	OUT1	OUT0
0	0	0	0	0
0	1	0	1	0
1	0	1	0	0
1	1	1	0	1

$$\begin{cases} OUT2 = A \\ OUT1 = \overline{A} \cdot B \\ OUT0 = A \cdot B \end{cases} \tag{16.39}$$

16.3.3 Skyrmion-based transistors

In [190] it was proposed a skyrmionic device able to behave like a conventional CMOS transistor. Its structure is shown in figure 16.30a.

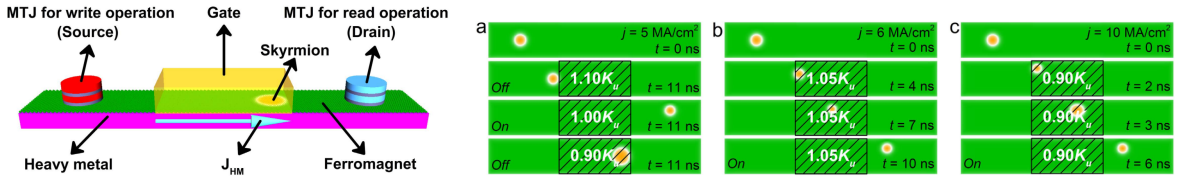

(a) (b)

Figure 16.30: (a) Structure of the skyrmionic transistor: two MTJ are used respectively for writing and for reading the skyrmion, whose motion is achieved via SHE. The gating effect is obtained applying a voltage on the gate terminal and tuning the magnetic anisotropy of the gate region of the nanotrack. (b) Snapshots of micromagnetic simulation: if no voltage is applied $K_{uv} = K_u$ and the transistor is on. If $K_{uv} > K_u$ the skyrmion encounters a potential barrier and pins at the left of the gate region; if $K_{uv} > K_u$ it finds a potential well and pins at the right side of the gate area. In both cases, increasing the current density is possible to depin the skyrmion and turn the transistor on. Figures extracted from [190].

In this device, a MTJ is used for nucleating the skyrmion and a second MTJ is used for reading it, just like described in section 16.2.5; the skyrmion is moved from source to drain via the SHE by a J_{HM} flowing in the bottom HM layer. Finally, the gating is obtained by applying a voltage on the gate terminal: this will induce a variation of the PMA parameter K_{uv}, according to the relation

$$K_{uv} = K_u + \Delta K_{uv} E \tag{16.40}$$

where E is the applied electric field.

In the *off* state both the current density and the electric field are applied, while in the *on* state only the electric field is turned off, so that $K_{uv} = 1.00 K_u$. Like equation 16.40 shows, the electric field increases the value of the PMA; the energy of the skyrmion is

$$E_{sk} = -\frac{D^2\pi^4}{4K\pi + \frac{16}{\pi}B} + 38.7A \tag{16.41}$$

while its radius, according to this article, is

$$R_{sk} = -\frac{D\pi^2}{2K\pi + \frac{8}{\pi}B} \tag{16.42}$$

where K is the PMA constant, D is the DMI magnitude, A is the exchange constant and B is the magnetic field. However, like discussed in section 16.2.6, this equation for the radius of the skyrmion has been proven wrong in [207], according to which the correct (approximated) definition of the radius is

$$R_{sk} = \pi D \sqrt{\frac{A}{16AK^2 - \pi^2 D^2 K}} \tag{16.43}$$

where the label of each parameter has remained the same. In this way it is represented the dependence of the radius not only on D and K (whereas the dependence on B is more complex to be represented), but also on the exchange interaction stiffness A. However, the key point here is that the dependence on the PMA constant has remained similar: if the PMA increases the skyrmion radius decreases, and vice versa, decreasing the PMA the radius increases. According to equation 16.41, increasing the magnetic anisotropy the energy of the skyrmion increases too and vice versa, decreasing the magnetic anisotropy the energy decreases.

As a result, from the snapshot (a) in 16.30b it can be observed that, if the electric field is turned off, the skyrmion is free to go through the voltage-gated region and to reach the drain. If the electric field increases the PMA, it means that the skyrmions finds a potential barrier on the left side of the gated region and stops there. If, in the contrary, the field decreases the PMA, the skyrmion finds at first a potential well and is able to enter the gated region (and its radius there increases, like predicted); then, going out of the potential well it finds a potential barrier, and if the current density is not enough it won't be able to exit the potential well, remaining pinned at the other side of the gated region. However, in both cases there is always a current density threshold above which the skyrmion is able to overcome the barrier and reach the drain. In the article the authors have studied the dependence of this threshold on the PMA value and on the intensity of the DMI. Finally, it has been demonstrated that the same behaviour is verified even if the size of the nanotrack is reduced, and this indicates the good scalability of this skyrmionic transistor, which could be used as a component of hybrid skyrmionic-electronic devices.